Suzaku Study of Non-Thermal Iron Line Emission at 6.4 keV from Supernova Remnants

Shigetaka Saji

Space Astronomy Laboratory (X-ray Astronomy Group),
Division of Particle and Astrophysical Science,
Graduate School of Science, Nagoya University

February 9, 2018

Abstract

Iron (Fe) K-shell emission lines have been detected in many Supernova Remnants (SNRs) (e.g. Yamaguchi et al., 2014). Generally the line emission originates from optically thin thermal plasma heated by the blast wave. Recently, Sato et al. (2016) reported peculiar line emission at 6.4 keV from the Galactic SNR Kes 79. The spatial distribution of the line emission was correlated with a molecular cloud rather than the thermal X-ray radiation. Sato et al. (2014) also discovered a hint of the 6.4 keV emission line from 3C 391, which can be associated with molecular clouds. Such a 6.4 keV line was also reported from five Galactic SNRs even though the electron temperatures of its thermal plasma are lower than $\sim$ 1 keV (Nobukawa et al., 2017). Since almost no iron K-shell lines are emitted from such low-temperature plasma, the 6.4 keV line emission is thought to be generated by non-thermal processes such as interactions between low-energy cosmic-ray particles and adjacent cold gases, or photoionization. Based on the large equivalent width of $\gtrsim$ 400 eV and the absence of the X-ray irradiating sources, the authors claimed that the low-energy cosmic-ray proton with the $\sim$MeV energy is the most plausible origin of the 6.4 keV line. However, the property of the 6.4 keV line and the emission mechanism are still unclear.

In this thesis, the 6.4 keV line emission is systematically searched for using the Suzaku X-ray Imaging Spectrometer (XIS) data of several Galactic SNRs. The Suzaku XIS is the best instrument for our purpose, owing to the good energy resolution ($\sim$ 130 eV at 6 keV) as well as the low and stable background. Our sample consists of SNRs in the western side of the Galactic plane with their coordinates $l > 180^\circ$ and $|b| < 1.^\circ 0$. SNRs known to have plasma with the temperature higher than 1 keV are excluded, since the Fe Kα line emitted via thermal processes can be a contamination of our analysis. Then our sample consists of 11 SNRs.

Spatially-extended enhancements of the 6.4 keV line are found from G304.6+0.1 at a significance level of 3.6σ, G323.7$-$1.0 at 4.1σ and G346.6$-$0.2 at 3.2σ. In addition, there are signs of the 6.4 keV line enhancements at 2.7σ in G330.2+1.0 and at 2.2σ in G348.5+0.1. In G304.6+0.1, G323.7$-$1.0 and G346.6$-$0.2, the spatial distribution of the 6.4 keV line emission is different from that of the thermal X-ray radiation. The equivalent width of the 6.4 keV line is generally large; in particular, the equivalent width of the enhancement in G323.7$-$1.0 is larger than 1200 eV. The combined spectrum of the enhancements in the three SNRs shows the

equivalent width larger than 760 eV. The energy centroid is 6.40 ± 0.02 keV, indicating that the ionization state is lower than $100(n_{\rm e}/1\ {\rm cm}^{-3})$ yr, here $n_{\rm e}$ is the electron number density of the plasma.

We concluded that the 6.4 keV line does not originate from thermal plasma, based on the large equivalent width and the low ionization state. The observed equivalent width and the energy centroid require low-ionized Fe-rich ejecta. Such low-ionized ejecta are quite unlikely in G304.6+0.1, G323.7−1.0 and G346.6−0.2 because of the relatively old age of the SNRs ($\gtrsim 10^4$ yr). In addition, it is impossible to generate the young plasma within 100 yr by the shock heating, since it takes more than 3000 yr to cross the 6.4 keV emitting region assuming the shock velocity of 3000 km s^{-1}. The 6.4 keV line emission is explained by non-thermal processes such as K-shell ionization by photons, non-thermal electrons or protons with energy above the Fe K-edge (7.1 keV). The photoionization scenario is rejected because of the absence of the X-ray irradiation source. The scenario of the ionization by cosmic-ray electrons is also unlikely due to the large equivalent width. The interactions between the protons with an energy of ~ 10 MeV and the adjacent cold gases, on the other hand, can explain the results. The protons are possibly accelerated in the SNRs.

Contents

List of Figures

List of Tables

Chapter 1

Introduction

1.1 6.4 keV line emission from SNRs

Iron (Fe) K-shell emission lines have been detected in many Supernova Remnants (SNRs). In most cases the line emission is located around the center of the SNR, and hence the iron is thought to originate from the ejecta. The Fe-rich ejecta are heated by the reverse shock, and the ionization state is often lower than the helium-like (He-like) state in young or middle-aged SNRs (Yamaguchi et al., 2014). The ionization state determines the Fe Kα energy centroid; its centroid changes to higher energy from Fe X to Fe XXVI (e.g. Vink, 2012). The Fe Kα lines detected from the SNRs above are emitted from thermal plasma with a temperature of $\gtrsim 1$ keV.

Sato et al. (2016) reported a peculiar Fe Kα line emission centroid at ~ 6.4 keV from the Galactic SNR Kes 79. The spatial distribution of the 6.4 keV line emission was correlated with a molecular cloud rather than the thermal X-ray radiation. Thus the 6.4 keV line emission from Kes 79 is unlikely to originate from the thermal plasma. Such a 6.4 keV line was also reported from five Galactic SNRs even though the electron temperatures of their thermal plasma are lower than ~ 1 keV (Nobukawa et al., 2017). Since almost no Fe K-shell electrons can be ionized in such low-temperature plasma, the 6.4 keV line emission is thought to be generated by non-thermal processes. The authors claimed that a possible origin of the 6.4 keV line is interactions between low-energy cosmic-ray protons and the adjacent cold gas. Due to the lack of the samples, however, the property and the emission mechanism of the 6.4 keV line are still unclear.

1.2 Aim of this work

The aim of this work is to reveal the nature of the non-thermal 6.4 keV line emission from SNRs. First, we systematically analyze the Galactic SNRs focusing on the 6.4 keV line. Then detailed analyses are performed for the SNRs which exhibit significant 6.4 keV line enhancement. Based on the results, the possible origin of the 6.4 keV line emission is discussed.

To investigate the 6.4 keV line, it is necessary to resolve the Fe I Kα (6.4 keV), Fe XXV Kα (6.7 keV) and Fe XXVI Kα (7.0 keV) lines. In addition, the background has to be low and stable since the signal of the 6.4 keV line is quite weak. The Suzaku XIS meets these requirements. The energy resolution of $\sim$ 130 eV at 6 keV is enough to resolve the three Fe Kα lines. In addition, the background level of the Suzaku XIS is low and stable owing to the low altitude of its orbit. Thus we used the Suzaku archival data for our analysis.

This thesis consists of the following chapters. The basic physics and previous researches are reviewed in chapter 2. Then characteristics of the instruments on board Suzaku are explained in chapter 3. The sample selection and the observations are summarized in chapter 4. In chapter 5, systematic analyses for all selected SNRs are presented. More detailed analyses for SNRs which show significant enhancement of the 6.4 keV line are shown in chapter 6. Implications of these results and previous studies are discussed in chapter 7. Chapter 8 gives the summary of this thesis.

Chapter 2

Review

2.1 Supernova Remnants (SNRs)

SNRs are nebulae composed of heated interstellar gas and ejecta generated by supernovae (SNe). When an SN explosion occurs, the ejecta expand into interstellar space and generate strong shock wave. About 300 SNRs have been discovered in our Galaxy (Green, 2009).

2.1.1 Supernovae

The SN can roughly be classified into two groups based on the explosion mechanism; Type Ia or Core-Collapse (CC). The optical spectrum of a Type Ia SNe has no H absorption line, and the Type Ia SN is believed to be a thermonuclear explosion of a white dwarf in a binary system. When the mass of the white dwarf exceeds the Chandrasekhar limit (~ 1.4 $M_\odot$) due to gas accretion or a merger of two white dwarfs, the thermonuclear burning is ignited. Some elements such as Fe and Si are synthesized rather than O, Ne, and Mg (Nomoto et al., 1984; Iwamoto et al., 1999). A CC SN is a catastrophic explosion of a massive star ($M > 8$ $M_\odot$). A massive star generates heavy elements at the center and finally an Fe core is produced. Since Fe is the most stable element, the core cannot generate the energy to support itself against the gravity anymore. Then the star collapses. A strong shock wave is generated by the released gravitational energy and it propagates outward. The shock wave leads to the explosive nuclear fusion and ejects the nuclear-fused material outwards. Therefore, the abundances created by a CC SN are affected by the envelope, which depends on the mass of the collapsing star. Less of Fe is ejected by a CC SN compared to a Type Ia SN. The remnants of the core are believed to leave a neutron star or a black hole after the explosion.

2.1.2 Thermal and non-thermal processes in SNRs

Thermal plasma

After an SN explosion, the ejecta expands without deceleration since the interaction with the low-density ISM is negligible at first. The expansion velocity is typically about 10^4 km s^{-1}, which is much higher than the sound speed in the ISM (~ 15 km s^{-1}). Therefore an expanding forward shock is generated. In addition to the forward shock, shocks propagate inward the SNR are also generated. As the shock wave passes, the translational motion converts to the random motion and the gas is thermalized.

Based on the Rankin & Hugoniot relations, the temperature of the post-shock gas is written by

$$kT = \frac{3}{16}\mu m_{\rm H} v_{\rm s}^2, \tag{2.1}$$

where μ, $m_{\rm H}$ and $v_{\rm s}$ show the mean atomic mass, the mass of a hydrogen atom, and shock velocity, respectively. Here the gas is assumed to be mono-atomic gas. Typically the temperature of the heated plasma reaches about 1 keV. The plasma emits the bremsstrahlung and lines in the X-ray band. The details of the X-ray emission is summarized in section 2.2.

Non-thermal processes

One of the most important processes in SNRs is cosmic-ray acceleration. The principle idea of the cosmic-ray acceleration is that the changed particles are reflected by moving magnetic fields (Fermi, 1949). A head-on encounter between a cosmic-ray particle and the magnetic field leads to the gaining energy, while a tail-on encounter leads to an energy loss. Since the head-on encounters occur more frequently than the tail-on encounters, the cosmic-ray particles increase their energy on average. This statistical acceleration is called the second order Fermi acceleration.

In the environment of shocks, the acceleration process becomes more efficient. If a cosmic-ray particle reflects between magnetic structures upstream and downstream of the shock, every encounter is head-on and thus the cosmic-ray particle is accelerated rapidly. This is called the first order Fermi acceleration. In Bell (1978), the spectrum of the accelerated particles was theoretically investigated. By considering a statistical escape from the accelerating region, the spectrum is calculated to be

$$\frac{dN}{dE} \propto E^{-2}. \tag{2.2}$$

The electrons accelerated to the GeV band can be observed in the radio band. Indeed, most of the SNRs are identified in the radio band at first. A relativistic electron moving in an external magnetic field emits continuum-spectrum radiation. This process is called the

synchrotron radiation. The critical frequency is defined as

$$\nu_c = \frac{3e}{4\pi m_e c} B_\perp \left(\frac{E}{m_e c^2}\right)^2, \tag{2.3}$$

where e is the electric charge of the electron, m_e is the electron mass, c is the light speed, $B_\perp$ is the strength of the magnetic field perpendicular to the motion of the electron, and E is the kinetic energy of the electron. The emitted power reaches its maximum at the frequency of 0.29 times the critical frequency (e.g. Rybicki & Lightman, 1979). For example, radiation at $\sim$ 1 GHz is produced by electrons with the energy of $\sim$ 5 GeV assuming a typical magnetic field of $\sim$ 10 μG. The observed frequency is proportional to the square of the electron's energy.

When the kinetic energy of the electrons reaches to the TeV band, X-rays are emitted by the synchrotron radiation. In addition to the synchrotron X-rays, high-energy gamma-rays are produced by the inverse Compton scattering. In this process, very high-energy electrons scatter low-energy photons, such as the cosmic microwave background, to higher energy. The power of the gamma-rays generated by the inverse Compton scattering is given by

$$P = 4\sigma_T c \beta^2 \gamma^2 U_{ph}, \tag{2.4}$$

where σ_T is the Thomson cross section, $\beta = v/c$ (v is the velocity of the electron), $\gamma^2 = 1 - (v/c)^2$, and the U_{ph} is the photon energy density.

High-energy gamma-rays are produced also by the high-energy protons. Accelerated protons produce neutral pions (π^0) when they collide with other protons in the interstellar matter such as molecular clouds. A neutral pion decays with a mean lifetime of 8.4×10^{-17} s and then generates two gamma-ray photons. This process is written as

$$p + p \rightarrow p + p + \pi^0 \rightarrow p + p + \gamma + \gamma. \tag{2.5}$$

To produce a neutral pion, the kinetic energy of the incident protons has to exceed $\sim$ 280 MeV. In this process, the intensity of the gamma-rays is proportional to the multiplication of the target density and the cosmic-ray proton's energy density.

Such high energy cosmic-ray particles are thought to be in many SNRs. For example, non-thermal continuum X-ray spectrum, which can be explained by the synchrotron radiation, was discovered in SN1006 (Koyama et al., 1995). Later, association of the high-energy gamma-ray emission was detected (Tanimori et al., 1998) and then the existence of the very high-energy electrons was confirmed. The SNR RX J1713.7−3946 is also known to emit very high-energy gamma-rays. The gamma-ray intensity is well correlated with the distribution of the interstellar medium (Fukui et al., 2012). Therefore it is suggested that the dominant source of the gamma-

rays is the high-energy cosmic-ray protons.

The cosmic-ray particles above $\sim$ GeV band have been investigated relatively well. Property of lower-energy cosmic-rays, on the other hand, is less understood, since neither the electrons nor protons in the $\sim$ MeV band are hard to observe. For example, the "injection" process for the acceleration is one of the unresolved problems. Although the Fermi acceleration is thought to start from relatively high-energy particles of the thermal plasma, the detailed process is still unclear. In addition to the injection, escape process from the accelerating site is also not well understood. Assuming a typical strength of the magnetic field in the accelerating site of 0.1 mG, the Larmor radius of an electron or a proton with the energy of 1 GeV are 1×10^{-8} pc or 2×10^{-8} pc, respectively. Thus the relatively low-energy cosmic-ray particles cannot escape from the accelerating region if the direction of the magnetic field is random. To discuss the detailed process of the cosmic-ray acceleration, information of the low-energy cosmic-rays is necessary.

2.1.3 Dynamical evolution

The dynamical evolution of an SNR can be classified into four phases: free expansion phase, adiabatic phase, radiative cooling phase and disappearance phase. Each phase is defined as follows.

Free expansion phase

After an SN explosion, the ejecta expands without deceleration since the interaction with the low-density ISM is negligible at first. The expanding forward shock sweeps up the ISM. The boundary between the ejecta and the ISM is called the "contact discontinuity". Behind the contact discontinuity, a reverse shock starts to propagate into the ejecta. When the swept-up mass of the ISM becomes larger, it starts to affect the SNR's expansion.

Adiabatic phase (or Sedov-Taylor phase)

When the mass of the accumulated ISM becomes greater than that of the ejecta in the SNR shell, the kinetic energy of the ejecta is significantly transferred to the ISM and the forward shock is decelerated. The energy loss via radiation is still negligible in this phase. An exact self-similar solution called the "Sedov-Taylor solution" is established (Taylor, 1950; Sedov, 1959). The gas flow is characterized by two parameters; initial kinematic energy of the SN explosion (E_0) and the surrounding ISM density (n_0). The radius $R_{\rm s}$ and the velocity $v_{\rm s}$ of the forward

shock, and the mean temperature behind the shock front $T_{\rm s}$ are given by

$$R_{\rm s} = 13 \left(\frac{E_0}{10^{51}{\rm erg}}\right)^{1/5} \left(\frac{n_0}{1{\rm cm}^{-3}}\right)^{-1/5} \left(\frac{t}{10^4{\rm yr}}\right)^{2/5} {\rm pc} \quad (2.6)$$

$$v_{\rm s} = 490 \left(\frac{E_0}{10^{51}{\rm erg}}\right)^{1/5} \left(\frac{n_0}{1{\rm cm}^{-3}}\right)^{-1/5} \left(\frac{t}{10^4{\rm yr}}\right)^{-3/5} {\rm km\ s}^{-1} \quad (2.7)$$

$$T_{\rm s} = 0.28 \left(\frac{E_0}{10^{51}{\rm erg}}\right)^{2/5} \left(\frac{n_0}{1{\rm cm}^{-3}}\right)^{-2/5} \left(\frac{t}{10^4{\rm yr}}\right)^{-6/5} {\rm keV}, \quad (2.8)$$

where t is the elapsed time after the SN explosion.

Radiative cooling phase

Atoms behind the shock front are highly ionized by the reverse shock at first. As the SNR expands and cools adiabatically, the ionized atoms start to capture free electrons and they can lose their excitation energy by radiation. In this phase, the radiative cooling becomes significant. The efficient radiative cooling decreases the thermal pressure behind the shock front and the expansion slows down.

Dispersion phase

More and more ISM is accumulated and the swept-up mass becomes much larger than that of the ejecta. The expansion velocity of the SNR drops to the sound velocity in the ISM, and the shock wave no longer lasts. Finally, the expansion velocity decreases to the values of the random motion of the ISM, and then the SNR disperses.

2.2 X-ray emission from SNRs

So far, more than $\sim$ 100 SNRs have been detected in the X-ray band. The thermal X-ray emission originates from optically-thin plasma heated by the shock wave. The plasma consists of the ejecta and the swept-up ISM. In this section, basic physics of the X-ray emitting thermal plasma and processes of the X-ray radiation are explained.

2.2.1 Emission components

X-ray emission from the plasma consists of three major components: continuum emission, line emission and radiative recombination continuum (RRC).

Continuum emission; Bremsstrahlung

Continuum emission is produced by free electrons in the plasma via the Coulomb interaction with ions. This emission is called thermal bremsstrahlung, when the energy distribution of electrons follows the Maxwellian distribution. The emissivity of the thermal bremsstrahlung is given by

$$\epsilon = \frac{2^5 \pi e^6}{3 m_{\rm e} c^3} \left(\frac{2\pi}{3 k_{\rm B} m} \right)^{1/2} T_{\rm e}^{-1/2} Z^2 n_{\rm e} n_{\rm i} e^{-h\nu/k_{\rm B}T} g_{ff}, \tag{2.9}$$

where e is the electron charge, c is the light speed, $k_{\rm B}$ is the Boltzmann constant, $T_{\rm e}$ is the electron temperature, Z is the ion charge, $n_{\rm e}$ is the electron number density, $n_{\rm i}$ is the ion number density and $g_{\rm ff}$ is the gaunt factor for the free-free emission (e.g. Rybicki & Lightman, 1979). Figure 2.1 shows the theoretical spectrum of the thermal bremsstrahlung. Each color indicates the spectrum from plasma with a temperature of 0.5 keV, 1.0 keV, 2.0 keV, 5.0 keV and 10.0 keV. Since the spectral shape of the thermal bremsstrahlung depends only on $T_{\rm e}$, the electron temperature can be estimated from the spectral shape of the continuum emission.

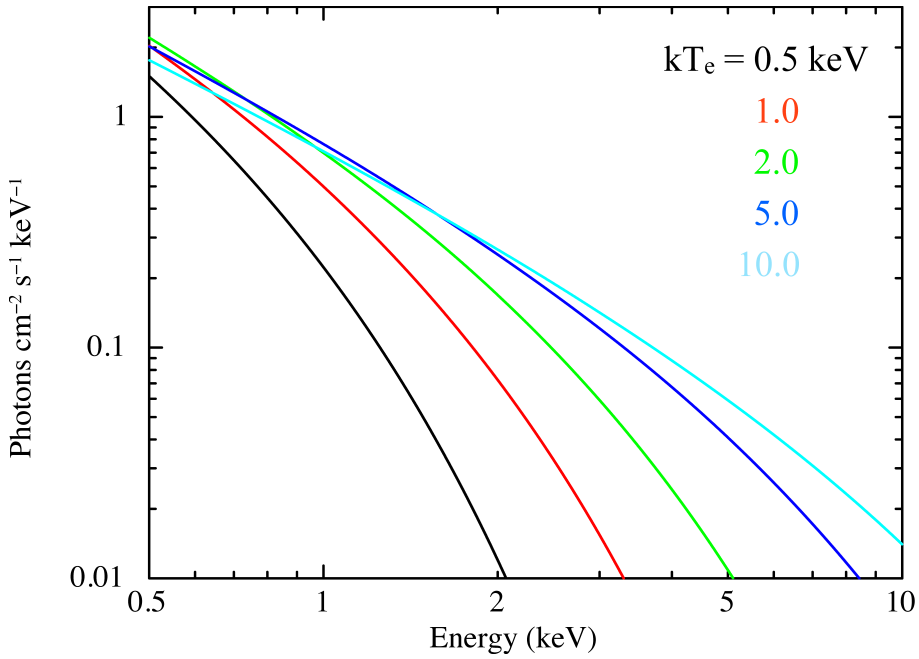

Figure 2.1: Theoretical spectrum of the bremsstrahlung in the cases of the electron temperature of 0.5 keV (Black), 1.0 keV (red), 2.0 keV (green), 5.0 keV (blue) and 10.0 keV (cyan).

Line emission

Line emission is produced by the bound-bound transition between two quantum levels. A Hydrogen like (H-like) ion, which has one electron, radiates the line emission with an energy of

$$E = Z^2 R_{\rm y} \left(\frac{1}{n} - \frac{1}{n'} \right), \tag{2.10}$$

where the Z, R_y, n, and n' indicate the atomic number, the Rydberg constant ($R_{\rm y} = 13.6$ eV), and the principal quantum number of before and after the transition, respectively. In the case of a Helium like (He-like) ion, which contains two electrons, the transition is more complicated. The Kα line from the He-line ion consists of three fine structures: the resonance ($1s2p\ ^1{\rm P}_1 \rightarrow 1s^2\ ^1{\rm S}_0$), forbidden ($1s2s\ ^3{\rm S}_1 \rightarrow 1s^2\ ^1{\rm S}_0$), and inter-combination ($1s2p\ ^3{\rm P}_{2,1} \rightarrow 1s^2\ ^1{\rm S}_0$) lines.

The energy centroid of the line emission depends on the ionization degree, and thus is a useful tool to estimate the ionization state. Figure 2.2 shows the energy centroid of the Fe Kα line as a function of the ionization degree. The energy centroid is almost constant from the ion charge of 0 (Fe I) to 8 (Fe I) at 6.4 keV. Above the ion charge of 8, it varies from about 6.4 keV (Fe I) to 6.7 keV (Fe XXV). The energy centroid of the Kα emission from the H-like ion (Fe XXVI) is 6.97 keV.

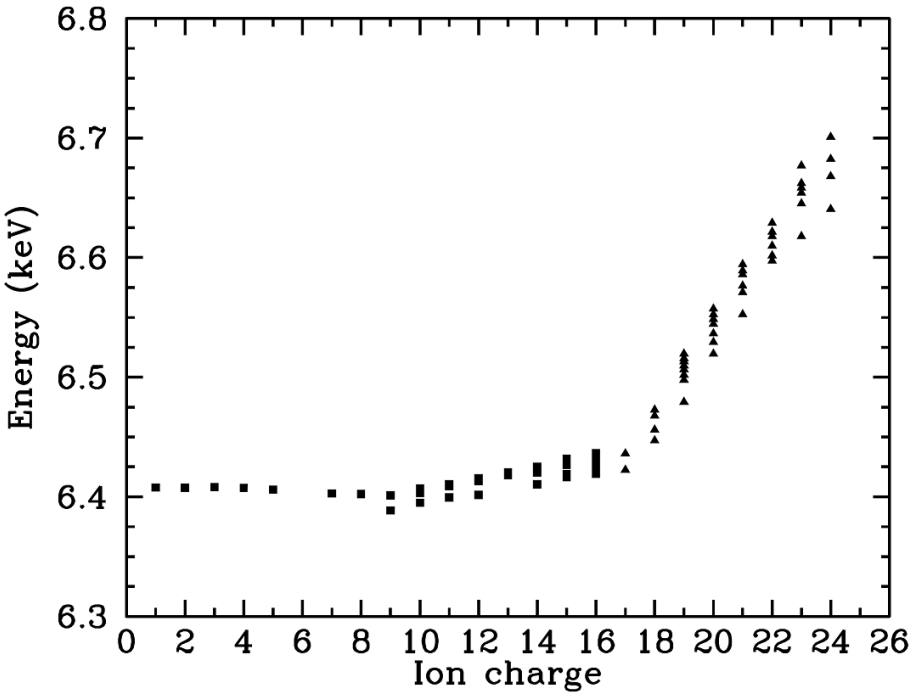

Figure 2.2: The energy centroids of Fe Kα lines determined theoretically(squares) and observationally (triangles). This figure is taken from Vink (2012).

Radiative Recombination Continuum (RRC)

Radiative Recombination Continuum (RRC) emission is produced when a free electron in the plasma is captured into the atomic shells. The energy of the emitted photon is described as $h\nu = E_{\rm e} + \chi$, where $E_{\rm e}$ and χ are the energy of the free electron and the binding energy of the captured electron, respectively. The spectral shape of the RRC is a continuum with a sharp edge at the binding energy, since the energy of the free electron is not uniquely determined in the thermal plasma. The emissivity is given by

$$\epsilon_{\rm RRC} = 4 n_{\rm e} n_{i+1} h\nu \left(\frac{h\nu - \chi}{kT_{\rm e}}\right) \left(\frac{1}{2\pi m_{\rm e} kT_{\rm e}}\right)^{1/2} \sigma^{rec} \exp\left(-\frac{h\nu - \chi}{kT_{\rm e}}\right), \tag{2.11}$$

where n_{i+1} is the density of ions with a charge state of $i+1$ and σ^{rec} is the recombination cross-section.

2.2.2 Non-equilibrium ionization

The status of the optically thin thermal plasma depends on two temperatures: ionization temperature ($kT_{\rm z}$) and the electron temperature ($kT_{\rm e}$). Here the ionization temperature $kT_{\rm z}$ indicates the ionization degree of ions in the plasma, while the electron temperature determines the energy distribution of electrons through the Maxwell-Boltzmann distribution. When $kT_{\rm z} = kT_{\rm e}$, the ionization rate and the recombination rate is the same. This state is called the collisional ionization equilibrium (CIE). When $kT_{\rm z} < kT_{\rm e}$, the plasma is in the non-equilibrium ionization state (NEI) and is called the ionizing plasma (IP). The ionizing process is more dominant than the recombining process in the IP.

The IP is usually seen in young SNRs due to the following reasons. The SNR shock converts the translational motion of the gas into the random motion and then thermal plasma is generated. However, the particles in the plasma are not much ionized at first. The timescale to reach the CIE is estimated as

$$\tau_{\rm ion} = \Sigma_{j=1}^{Z} (n_{\rm e} S_j)^{-1} \simeq 10^{12} n_{\rm e}^{-1} \text{ s}, \tag{2.12}$$

where $n_{\rm e}$ is the electron number density and S_j is the ionization rate coefficient from the jth ion (Masai, 1984). When we assume the electron density of $n_{\rm e} = 1$ cm^{-3}, it takes about 3×10^4 yr to reach the CIE. This timescale is comparable to the SNR age, and thus the plasma in young SNRs are IPs.

In addition to the IP and the CIE plasma, recombining plasma (RP) has been discovered in some SNRs (e.g. Yamaguchi et al., 2009). In the RP, the ionization temperature is higher than

the electron temperature ($kT_{\rm e} < kT_{\rm z}$), so that the recombining process is predominant. The RP cannot be explained by the standard SNR evolution, but two new scenarios have been proposed. The one is that the ionization of the plasma is advanced by strong X-ray irradiation (Nakashima et al., 2013) or high-energy cosmic-rays. The other one is that the electron temperature drops down by adiabatic rarefaction (Itoh & Masai, 1989; Yamaguchi et al., 2009) or by a thermal conduction with molecular clouds (Kawasaki et al., 2002). It is still unclear which process leads to the RP plasma.

2.2.3 Iron K-shell emission from the optically-thin thermal plasma

Figure 2.3 shows simulated X-ray spectra of the CIE plasma focusing on the Fe Kα lines, in the case of the plasma temperatures of 0.5 keV, 1.0 keV, 2.0 keV, 5.0 keV and 10.0 keV. Here the iron abundance is assumed to be that of the Sun (Lodders, 2003). We can see quite weak lines near 6.4 keV in the spectrum of the plasma with the temperature of 0.5 keV. The line intensity becomes stronger as the plasma temperature increases from 0.5 keV to 2.0 keV, since there are more electrons having enough energy to excite or ionize the inner shell. In addition, the electron and the ion interact more frequently in the plasma with higher temperature. Above 5 keV, on the other hand, the line intensity becomes weaker as the plasma temperature increases. This is explained by the decrease in the number of the iron having electrons.

The energy centroid of the lines becomes higher as the plasma temperature increases, since the iron is more ionized. Figure 2.4 shows the energy centroid of the Fe Kα line as a function of the ionization temperature.

The 6.4 keV line, which is the target of this work, is emitted from the plasma with the low ionization temperature of $kT_{\rm z} \lesssim 0.5$ keV. The electron temperature of $kT_{\rm e} = 0.5$ keV, on the other hand, is too low to emit strong iron K-shell lines (see figure 2.3). Thus the 6.4 keV line is not observed from the CIE plasma. In the case of the IP, significant 6.4 keV line can be emitted if the ionization temperature is low enough ($kT_{\rm z} \lesssim 0.5$ keV) and the electron temperature is high enough ($kT_{\rm e} \gtrsim 1$ keV).

2.2.4 Non-thermal X-ray radiation from SNRs

Diffuse non-thermal X-ray radiation has been detected from some SNRs (e.g. Koyama et al., 1995). The emission mechanism is thought to be synchrotron radiation by accelerated electrons. The energy of the electron is required to be ~ 100 TeV to emit X-rays assuming a magnetic field of $\sim$ 1–10 μG. The existence of such high energy electrons is confirmed by the clear detection of TeV gamma-rays from the SNRs(e.g. Aharonian et al., 2006a).

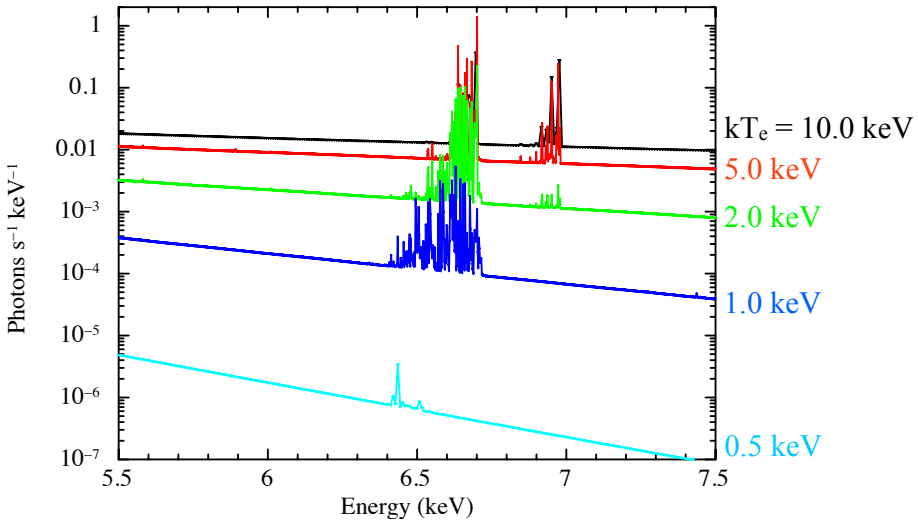

Figure 2.3: Simulated X-ray spectra of the CIE plasma with the temperatures of 10.0 keV (black), 5.0 keV (red), 2.0 keV (green), 1.0 keV (blue) and 0.5 keV (cyan), focusing on the Fe Kα lines. The spectra were simulated using apec model in XSPEC.

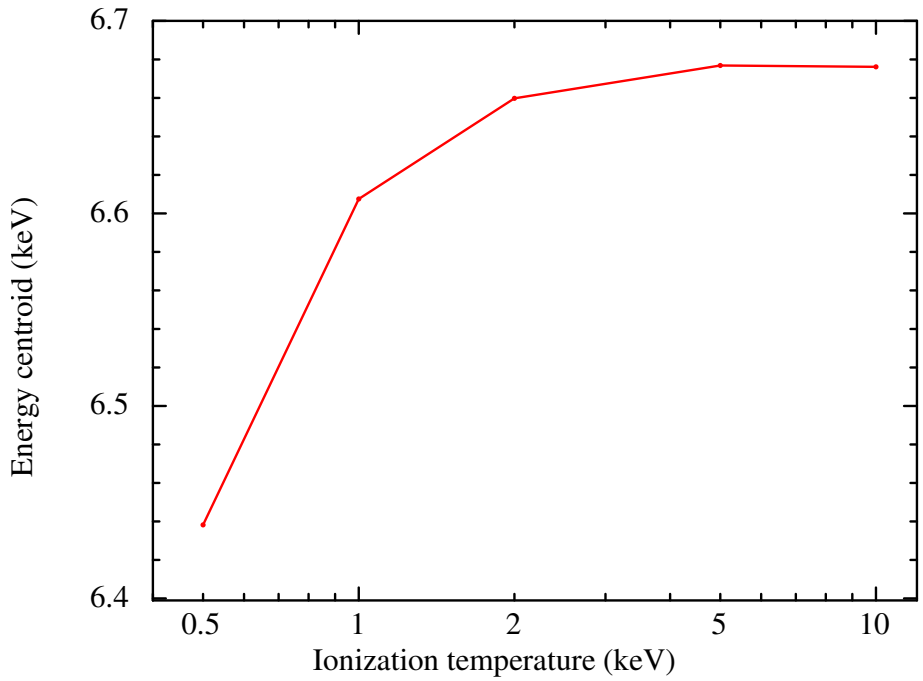

Figure 2.4: Energy centroid of the Fe Kα line as a function of the ionization temperature. The plasma is assumed to be in CIE.

2.3 Non-thermal Iron K-shell emission line

Many SNRs show iron Kα emission lines. Generally the line emission originates from the optically thin thermal plasma. Since the energy centroids of the lines are lower than 6.7 keV

in general, the iron is less ionized than the helium-like state. Yamaguchi et al. (2014) reported the energy centroid of the Fe Kα line in 23 young or middle-aged SNRs. The energy centroids are distributed from 6.408 eV (RCW 86) to 6.674 eV (IC 443) (see figure 2.5). The authors suggested that the energy centroids are clearly separated by the progenitor types: the Type Ia remnants show lower centroids than that of the core-collapse SNRs.

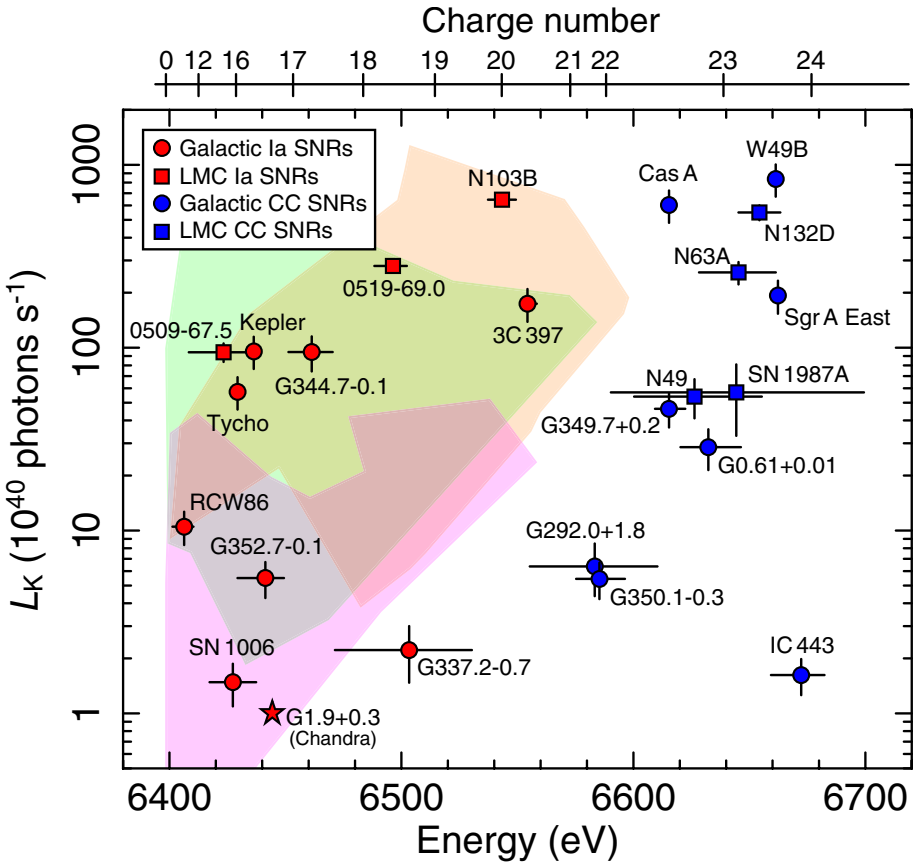

Figure 2.5: Energy centroids and luminosities of the Fe Kα lines from type Ia (red) and CC (blue) SNRs. The corresponding effective charge number is shown in the top of the panel. The circle and squares shows the SNRs in the Galaxy and in the LMC, respectively. The shaded regions indicate the energy centroids and the luminosities predicted by the theoretical models of the Type Ia SNRs: green, magenta and orange represent DDTa, DDTg and PDD models, respectively. The DDTa and DDTg are models assuming a delayed detonation explosion, while the PDD model adopts a pulsating delayed detonation explosion. The figure is taken from Yamaguchi et al. (2014).

Sato et al. (2016) reported peculiar line emission centroids on ~ 6.4 keV from the Galactic SNR Kes 79. The spatial distribution of the line emission is correlated with a molecular cloud rather than the thermal X-ray radiation. Sato et al. (2014) also discovered a hint of the 6.4 keV emission line from 3C 391, which can be associated with molecular clouds. Such a

6.4 keV line was also reported from five Galactic SNRs even though the electron temperature of their thermal plasma is lower than ~ 1 keV (Nobukawa et al., 2017). Since almost no iron K-shell lines are emitted from such low-temperature plasma, the 6.4 keV line emission is thought to be generated by non-thermal processes such as interactions between low-energy cosmic-ray particles and adjacent cold gases, or photoionization. Because of the large equivalent width of $\gtrsim 400$ eV and the absence of X-ray irradiating sources, the authors claimed that the low-energy cosmic-ray proton with an energy of $\sim$MeV is the most plausible origin of the 6.4 keV line.

2.4 Fe line emitted by non-thermal processes

Fe K-shell line can be produced by non-thermal processes such as K-shell ionization by photons, cosmic-ray electrons or protons with energy above the Fe K-edge (7.112 keV). In this section the non-thermal processes are reviewed.

2.4.1 Photoionization

Photoionization by X-rays with an energy higher than the Fe K-edge produces the Fe K-shell line. The irradiating X-rays ionize the K-shell electrons of the Fe atoms, and the Fe K-shell line is emitted via the de-excitation. This process is called the X-ray irradiation or the X-ray reflection. Continuum emission is also produced due to the Thomson scattering by either the outer-shell and free electrons. The equivalent width depends on the cross sections of the photo-electric and Thomson scattering, density of the electrons and Fe atoms, and the geometry. When we assume that the spectrum of the irradiating X-rays is represented by a power-law with the photon index of Γ, the equivalent width is written as

$$\mathrm{EW} = 3\left(\frac{1}{\Gamma+2}\right)\left(\frac{6.4}{7.1}\right)^{\Gamma}\left(\frac{1}{1+\cos^2\theta}\right) \quad \mathrm{keV}, \tag{2.13}$$

here θ indicates the angle between the incident and scattered X-rays (Tsujimoto et al., 2007). The Fe abundance is set to be that of the Sun (Lodders, 2003). When the reflection angle is $\theta = 90°$, the equivalent width becomes the largest value. Figure 2.6 shows the relation between the equivalent width and the photon index of the irradiating X-rays in the case of $\theta = 90°$. When the photon index of the irradiating X-rays is $\Gamma = 2$, for example, the equivalent width is 600 eV. The equivalent width is larger as the photon index becomes lower.

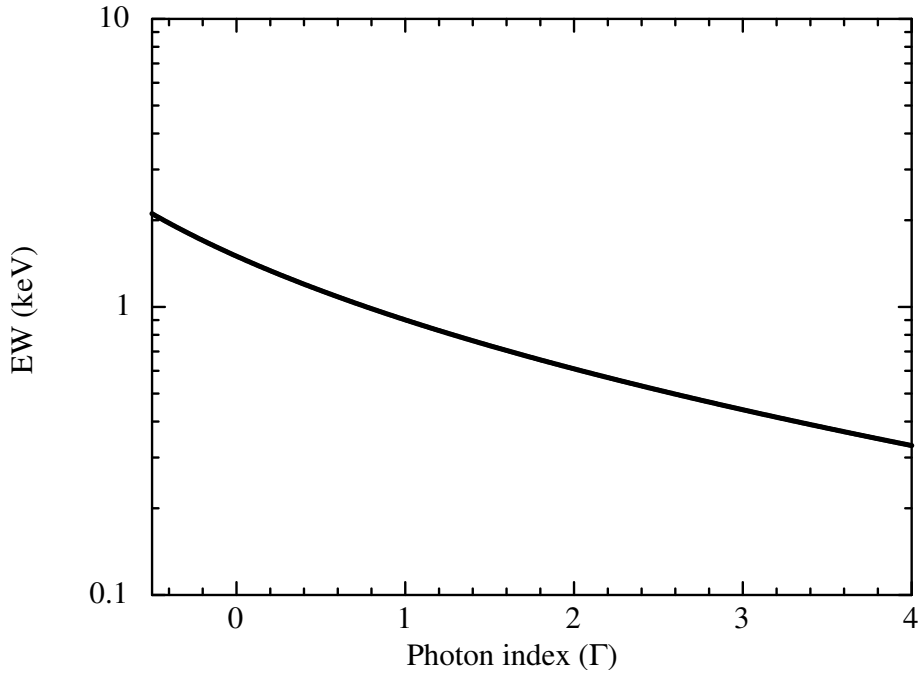

Figure 2.6: Equivalent width of the Fe Kα as a function of the photon index of the irradiating X-rays. The Fe abundance is assumed to be that of the Sun.

2.4.2 Ionization by non-thermal electrons or protons

Non-thermal electrons

Non-thermal electrons can produce the 6.4 keV line via the ionization of the K-shell electrons. In addition to the line emission, strong continuum emission is also generated by the bremsstrahlung. These X-ray emission produced by the non-thermal electrons is investigated in Tatischeff et al. (2012). The solid line in figure 2.7 (a) shows the cross-section for producing the 6.4 keV line by the impact of a fast electron, while the dashed line shows that for the bremsstrahlung at 6.4 keV. The vertical axis is shown in the cross-section per one H atom in the ambient medium. The Fe abundance is assumed to be that of the Sun (Lodders, 2003).

Non-thermal protons

Non-thermal protons can also generate the 6.4 keV line. In this process, the X-ray continuum is emitted by the collision of a high-speed proton with an electron in the ambient medium. This process is called the "inverse bremsstrahlung". The cross-sections for producing the line and the continuum X-rays by a non-thermal proton is shown in figure 2.7 (b) with the solid and dashed lines, respectively. The cross-section for producing the 6.4 keV line has a peak around 10 MeV, and thus the 6.4 keV line is mainly produced by the protons with the energy

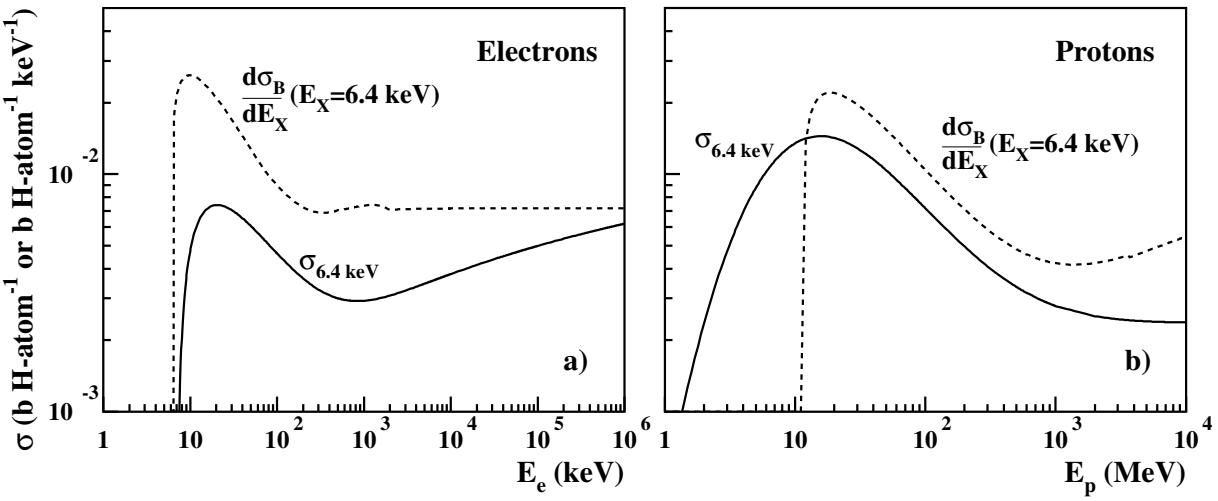

Figure 2.7: Solid lines shows the cross-sections in units of barn per ambient H-atom for producing the 6.4 keV line by a fast electron (left panel) and proton (right panel). The dashed lines show the differential cross-section for producing the continuum emission at 6.4 keV in units of barn per ambient H-atom per keV. The figures are taken from Tatischeff et al. (2012).

of ~ 10 MeV.

Equivalent width

The equivalent width of the 6.4 keV line produced by the non-thermal electrons or protons was estimated in Dogiel et al. (2011). The relation between the equivalent width and the particle index of the incident non-thermal electrons is shown in figures 2.8 with a blue curve, while that of the protons is plotted with a red curve. The equivalent width of the 6.4 keV line produced by the non-thermal electrons does not exceed 400 eV. The equivalent width of the line produced by the protons, on the other hand, strongly depends on the spectral index of the incident particles. When the spectral index of the incident protons is 2, the equivalent width is about 2 keV.

Both of the non-thermal electrons and protons generate secondary electrons by the ionization of the ambient gas. The secondary electrons can also contribute to the X-ray emission. Tatischeff et al. (2012) considered a model in which cosmic-ray particles penetrate into a nearby cloud composed of neutral gas at a constant rate. In the model, the fast particles slow down by the ionization and radiative energy losses, and finally stop or escape from the cloud. The X-ray spectra produced by the cosmic-ray particles depend on the cosmic-ray particle's spectral index, mean path length in the cloud, minimum energy entering the cloud, and the metallicity of the cloud. Based on the simulated X-ray spectra using several sets of the parameters, it was estimated that the contribution of the secondary electrons to the X-ray spectra is about 15% at most around 6.4 keV. Therefore the secondary electrons do not strongly affect the equivalent

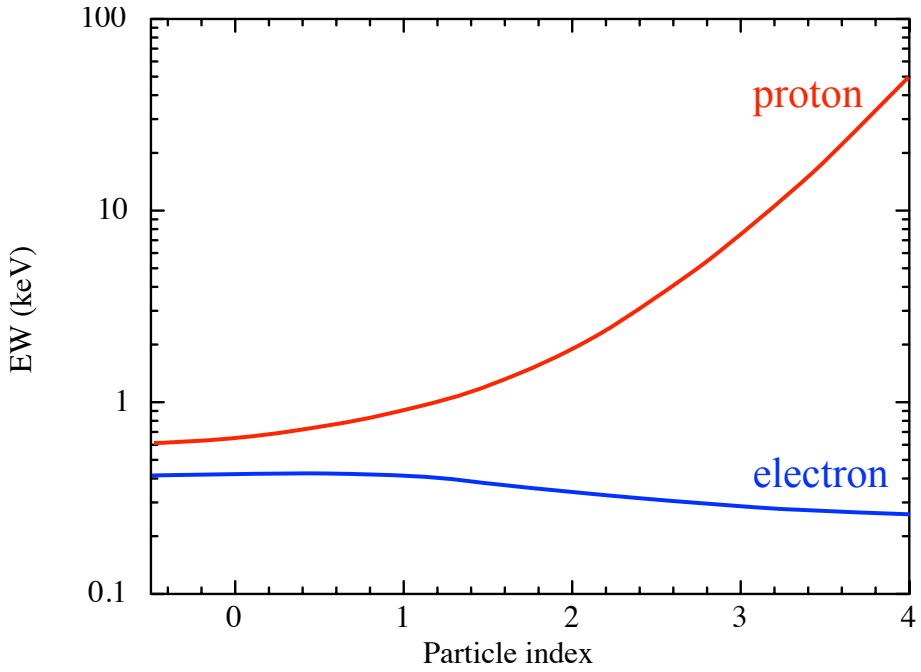

Figure 2.8: Relation between the equivalent width of the Fe Kα and the particle index of the cosmic-ray electrons (blue) and protons (red). The Fe abundance is assumed to be that of the Sun.

width shown in figure 2.8.

2.5 Diffuse iron Kα emission along the Galactic plane

The Galactic Ridge X-ray Emission (GRXE) is spatially unresolved X-rays along the Galactic plane discovered by HEAO 1 (Worrall et al., 1982). In addition to the GRXE, the X-ray intensity has a large peak at the Galactic center (Koyama et al., 1989; Yamauchi et al., 1990). The emission prevailing in the Galactic center region is called the Galactic Center X-ray Emission (GCXE). The GRXE and the GCXE are collectively called the Galactic Diffuse X-ray Emission (GDXE). Strong Fe I, Fe XXV and Fe XXVI K-shell lines are seen in the spectrum of the GRXE. The GDXE composes some part of the X-ray background in our analysis for the Galactic SNRs.

Both of the GRXE and the GCXE exhibit clear K-shell emission lines of Mg, Si and S mainly emitted from the low-temperature ($kT \sim 1$ keV) plasma and Fe from the high-temperature ($kT \gtrsim 5$ keV) plasma. Indeed, the GRXE spectrum cannot be explained by a one-temperature thermal plasma model, but can fairly be represented by a two-temperature thermal plasma model (Kaneda et al., 1997). Similar two-temperature model is also required in the GCXE (Uchiyama et al., 2013). In addition to the thermal plasma, a component to

emit the Fe Kα line at 6.4 keV is required to well represent the spectra. Figures 2.9 show the GCXE and GRXE spectra fitted with the two-temperature models as well as the 6.4 keV line and continuum components radiated from cold material (Uchiyama et al., 2013).

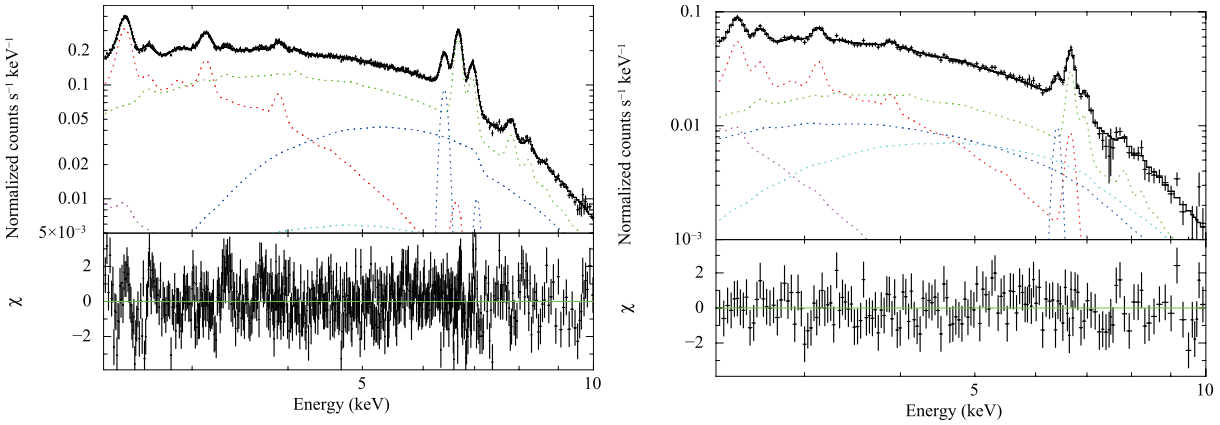

Figure 2.9: X-ray spectra of the GCXE (left) and GRXE (right). The solid lines are the best-fit models. The dotted lines show the low-temperature plasma (green), high-temperature plasma (red), cold matter (blue), cosmic X-ray background (cyan), and the foreground (magenta) model components. The figures are taken from Uchiyama et al. (2013).

The spatial distribution of the GDXE has often been expressed by exponential models. Uchiyama et al. (2013) modeled the intensity profile of the several emission lines and the continuum components adopting coordinates of $(l_*, b_*) = (l + 0.^\circ056, b + 0.^\circ046)$, where the origin $(l_*, b_*) = (0^\circ, 0^\circ)$ is the position of Sgr A*. The model is given by

$$\begin{aligned} I(l_*, b_*) = \quad & I_{\rm c} \times \exp\left(-\frac{|l_*|}{l_{\rm C}}\right) \times \exp\left(-\frac{|b_*|}{b_{\rm C}}\right) \\ & + I_{\rm R} \times \exp\left(-\frac{|l_*|}{l_{\rm R}}\right) \times \exp\left(-\frac{|b_*|}{b_{\rm R}}\right), \end{aligned} \tag{2.14}$$

where $l_{\rm C}$ and $l_{\rm R}$ are the e-folding scales along the Galactic plane, while $b_{\rm C}$ and $b_{\rm R}$ are the e-folding scales perpendicular to the Galactic plane, for the GCXE and GRXE, respectively. The normalizations of the GCXE and GRXE components are written by $I_{\rm C}$ (GCXE) and $I_{\rm R}$ (GRXE). The parameters of the Fe Kα line intensity profiles were obtained as shown in table 2.1. The errors in table 2.1 are in the 1σ confidence range.

More detailed intensity profiles of the Fe Kα lines were investigated in Yamauchi et al. (2016). They defined four regions along the Galactic plane; (a) $|l| < 0.^\circ5$, (b) $l = 358.^\circ5$, (c) $l = 356.^\circ0$–$356.^\circ4$, and (d) $|l| = 10^\circ$–30°. The latitude profiles of the Fe Kα lines in each region were modeled assuming that the GDXE is composed of three components; GRXE, GCXE, and Galactic Bulge X-ray Emission (GBXE). The GBXE is the X-ray emission associated to the Galactic bulge, and its spatial distribution is more extended than that of the GCXE. In the

Table 2.1: Parameters of the Fe Kα line profiles obtained by the two-exponential model fitting (Uchiyama et al., 2013).

Component	I_C[1]	I_R[1]	$l_C(^\circ)$	$b_C(^\circ)$	$l_R(^\circ)$	$b_R(^\circ)$
Fe I Kα	6.2 ± 0.6	0.21 ± 0.09	0.62 ± 0.09	0.23 ± 0.03	57 ± 50	1.1 ± 0.6
Fe XXV Kα	14.57 ± 0.47	0.91 ± 0.08	0.63 ± 0.03	0.27 ± 0.01	45 ± 10	2.9 ± 0.5
Fe XXVI Kα	6.08 ± 0.30	0.18 ± 0.04	0.63[2]	0.27[2]	45[2]	2.9[2]

[1] The units are 10^{-7} photons s^{-1} cm^{-2} $arcmin^{-2}$.
[2] These e-folding scales are linked to those of the Fe XXV Kα.

regions (a), (b) and (c), the GDXE is dominated by the GCXE and GBXE. Then the latitude profiles were modeled by an equation given by

$$I(b_*) = I_{\rm GCXE}\exp\left(-\frac{|b_*|}{b_{\rm GCXE}}\right) + I_{\rm GBXE}\exp\left(-\frac{|b_*|}{b_{\rm GBXE}}\right), \tag{2.15}$$

where $I_{\rm GCXE}$ and $I_{\rm GBXE}$ are the normalizations, while $b_{\rm GCXE}$ and $b_{\rm GBXE}$ are the e-folding scales along the Galactic latitude, for the GCXE and GBXE, respectively. In the region (d), on the other hand, the GDXE is composed of the almost pure GRXE. The latitude profile in the region (d) was modeled by

$$I(b_*) = I_{\rm GRXE}\exp\left(-\frac{|b_*|}{b_{\rm GRXE}}\right), \tag{2.16}$$

where $I_{\rm GRXE}$ and $b_{\rm GRXE}$ are the normalization and the e-folding scale of the GRXE, respectively. The best-fit values for the GCXE, GBXE, and GRXE were obtained as summarized in table 2.2. The errors in table 2.2 show the 1σ confidence level.

Yamauchi et al. (2016) also obtained the intensity profiles of the Fe Kα lines along the Galactic longitude. Figure 2.10 shows the Galactic longitude profiles of the Fe I, Fe XXV and Fe XXVI Kα line intensities. The longitude distribution, in particular of the Fe I Kα line, is different between the eastern side and the western side of the Galactic plane. The Fe I Kα line intensity around $l_* = 357^\circ$–358° (western side) is higher than that around $l_* = 2^\circ$–3° (eastern side). In addition, a significant enhancement in the Fe I Kα line intensity is seen at $l = 330^\circ$–340° (see figure 2.10). There is no such enhancement of the Fe I Kα intensity in the eastern side, $l = 20^\circ$–30°.

The origin of the GDXE is still under the discussion. A popular idea for the origin is a superposition of many faint point sources such as active binaries (ABs) and cataclysmic variables (CVs). Indeed, in a small area near the Galactic center, more than 80% of the flux of the GDXE has been resolved into point-like sources (Revnivtsev et al., 2009). However, more than a half of the Fe I Kα line intensity of the GRXE cannot be explained by the assembly of the CVs and ABs (Nobukawa et al., 2016). The origin of the excess in the Fe I Kα line is

Table 2.2: Best-fit parameters of the GCXE, GBXE, and GRXE profiles obtained in Yamauchi et al. (2016).

Region	Component	Parameter			
		Normalization (I)[1]			e-folding scale (b)[2]
		$l = 0^\circ$	$l = 358.^\circ5$	$l = 356.^\circ0$–$356.^\circ4$	
GCXE	Fe I Kα	4.2 ± 0.2	$= I_{l=0^\circ} \times 0.11$	$= I_{l=0^\circ} \times 0.004$	0.22 ± 0.02
	Fe XXV Kα	11.9 ± 0.6	$= I_{l=0^\circ} \times 0.11$	$= I_{l=0^\circ} \times 0.004$	0.26 ± 0.02
	Fe XXVI Kα	4.9 ± 0.2	$= I_{l=0^\circ} \times 0.11$	$= I_{l=0^\circ} \times 0.004$	0.24 ± 0.02
GBXE	Fe I Kα	0.31 ± 0.15	0.35 ± 0.10	0.28 ± 0.07	1.15 ± 0.36
	Fe XXV Kα	1.14 ± 0.34	1.15 ± 0.27	1.04 ± 0.21	2.25 ± 0.68
	Fe XXVI Kα	0.40 ± 0.12	0.39 ± 0.10	0.19 ± 0.06	2.13 ± 0.66
		$l = 10^\circ$–30°	$l = 330^\circ$–350°		
GRXE	Fe I Kα	0.23 ± 0.03	0.28 ± 0.04		0.50 ± 0.12
	Fe XXV Kα	0.76 ± 0.02	0.54 ± 0.03		1.02 ± 0.12
	Fe XXVI Kα	0.09 ± 0.02	$= I_{l=10^\circ-30^\circ}$		0.71 ± 0.29

[1] The units are 10^{-7} photons s^{-1} cm^{-2} arcmin^{-2}.
[2] The unit is degree.

unclear.

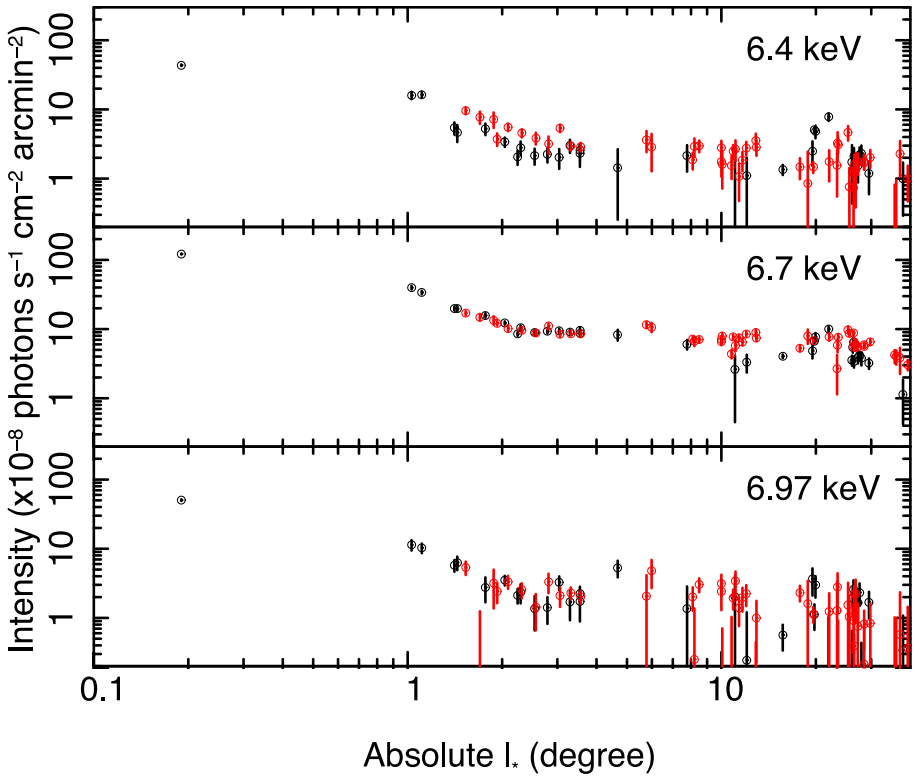

Figure 2.10: Galactic longitude distribution of the Fe I, Fe XXV and Fe XXVI Kα line fluxes. The red and black colors show the data of the eastern side and the western side of the Galactic plane, respectively. The figure is taken from Yamauchi et al. (2016).

Chapter 3

Instruments

3.1 Suzaku satellite overview

Suzaku (Astro-E2; Mitsuda et al., 2007) is the fifth Japanese X-ray observatory developed by Japan Aerospace Exploration Agency (JAXA), launched from JAXA's Uchinoura Space Center (USC) on 2005 July 10. The operation had been processed until 26 August 2015. The orbit is a near-circular path with an altitude of 550 km and an orbital period of about 96 minutes. The length of the spacecraft is 6.5 m along the telescope axis and the total weight is $\sim$ 1700 kg. Figures 3.1 shows a schematic view of the Suzaku satellite.

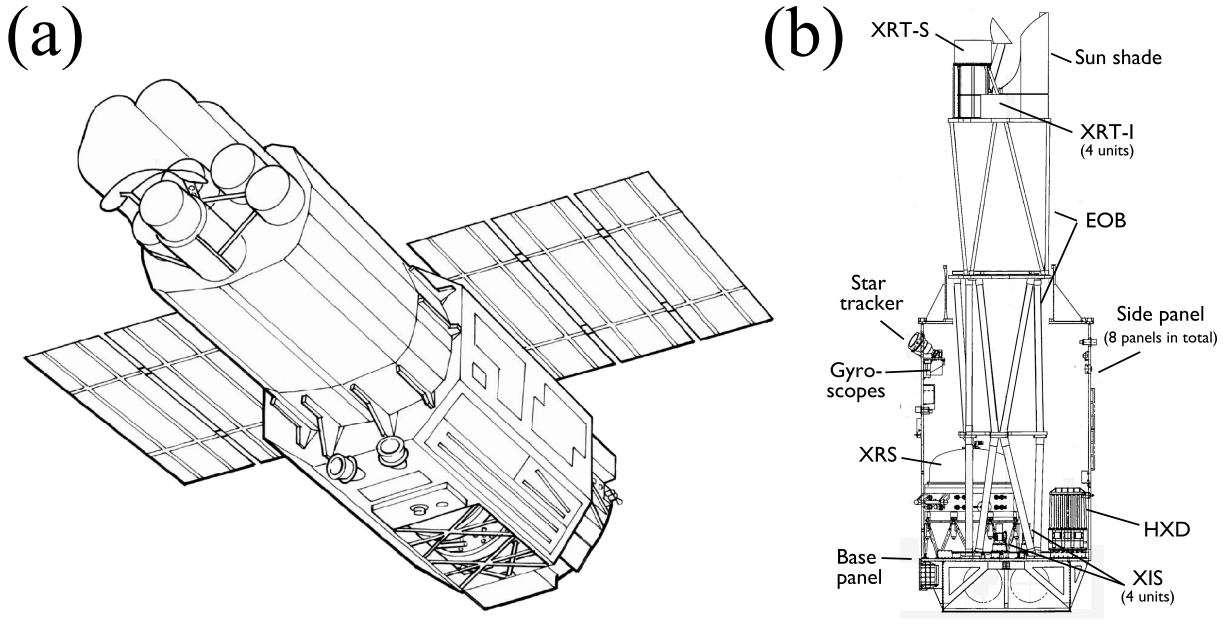

Figure 3.1: (a) : Schematic view of the Suzaku satellite in orbit. (b) : Side view of Suzaku with the internal structure (Mitsuda et al., 2007).

Suzaku is equipped with three types of soft and hard X-ray detectors. There are four X-ray Imaging Spectrometers (XISs; Koyama et al., 2007a), the X-ray Spectrometer (XRS; Kelley et al., 2007), and the Hard X-ray Detector (HXD; Takahashi et al., 2007). Each XIS or XRS is placed in the focal point of a dedicated X-ray Telescope (XRT; Serlemitsos et al., 2007). Unfortunately, the XRS does not provide the planned science because its liquid helium coolant was lost on August 8, 2005. We will not discuss the XRS further in this thesis. The XISs employ X-ray sensitive silicon Charge-Coupled Devices (CCDs) and perform imaging and spectroscopy in the 0.5–12 keV band. The HXD actually consists of two types of detectors: PIN silicon diodes and GSO scintillator. The sensitive energy range for the PIN and GSO are 10–70 keV and 40–600 keV, respectively. Since we used the data of the XIS, the details of the HXD are beyond the scope of this thesis.

The capability of the XRT and XIS is summarized in table 3.1. The details of these instruments will be described in the following sections.

Table 3.1: Overview of Suzaku capabilities

XRT	Focal length	4.75 m(XRT-I), 4.5 m(XRT-S)
	Field of View	$17'$ at 1.5 keV
		$10\farcm3$ at 8 keV
	Effective Area	440 cm^2 at 1.5 keV
		250 cm^2 at 8 keV
	Angular Resolution	$1\farcm79$–$2\farcm28$(Half Power-Diameter)
XIS	Field of View	$17\farcm8 \times 17\farcm8$
	Bandpass	0.2–12 keV
	Pixel grid	1024×1024
	Pixel size	24 μm $\times$24 μm
	Energy resolution	$\sim$ 130 eV at 6 keV (FWHM)
	Effective area	330 cm^2 (FI), 370 cm^2 (BI) at 1.5 keV
		160 cm^2 (FI), 110 cm^2 (BI) at 8 keV
	Time Resolution	8 s (Normal mode)

3.2 X-Ray Telescope (XRT)

Five XRT modules are set on the top of the Extensible Optical Bench (EOB) (see figure 3.1). XRT-S is adapted to the XRS, and the other four modules (XRT-I0, I1, I2 and I3) are dedicated for the XISs. The focal length of the XRT-I is 4.75 m. Figure 3.2 shows a photograph of one of the telescope modules (XRT-I1).

The XRT employs Wolter-I grazing-incidence reflection optics, which is illustrated in figure 3.3. Although the ideal Wolter-I optics consists of a pair of paraboloidal and hyperboloidal

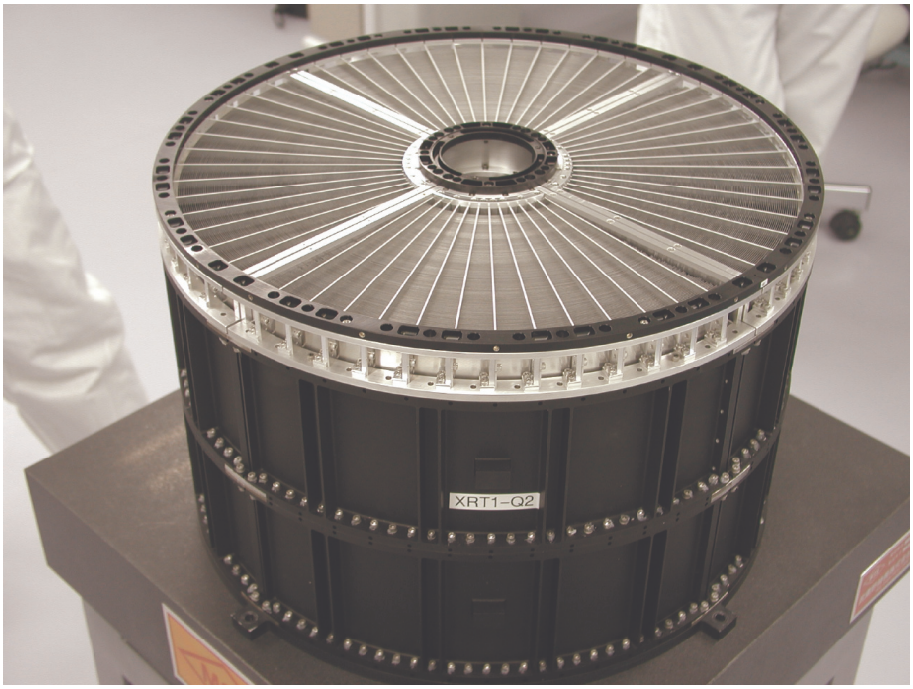

Figure 3.2: Picture of the XRT-I. The thermal shield is not yet attached (Serlemitsos et al., 2007).

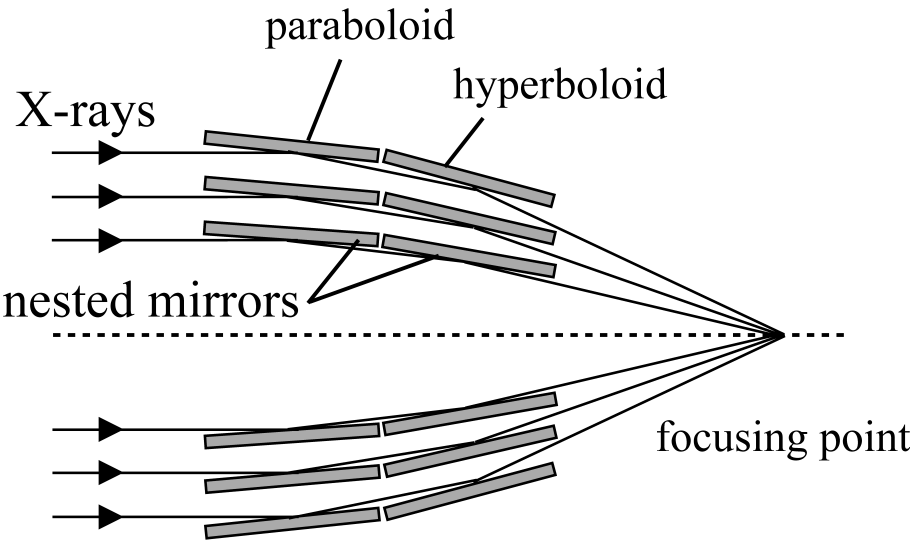

Figure 3.3: Schematic illustration of Wolter-I optics. X-rays travel along the arrows and concentrate on a detector placed at the focusing point.

mirrors, two-stage conical mirrors are adopted in the XRT. In each XRT module, 175 layers of thin reflectors are tightly nested co-focally and co-axially, and thus provides a large aperture efficiency. The effective area per unit is about 440 cm^2 at 1.5 keV and 250 cm^2 at 8 keV.

Figure 3.4 shows the effective area as a function of the energy including the response of the XIS. The effective area for an off-axis source is smaller than that for on-axis one. This effect is called vignetting. Figure 3.5 shows the relation between the effective area and the off-axis angle in two energy bands; 3–6 keV and 8–10 keV. The vignetting effect is prominent in the higher energy.

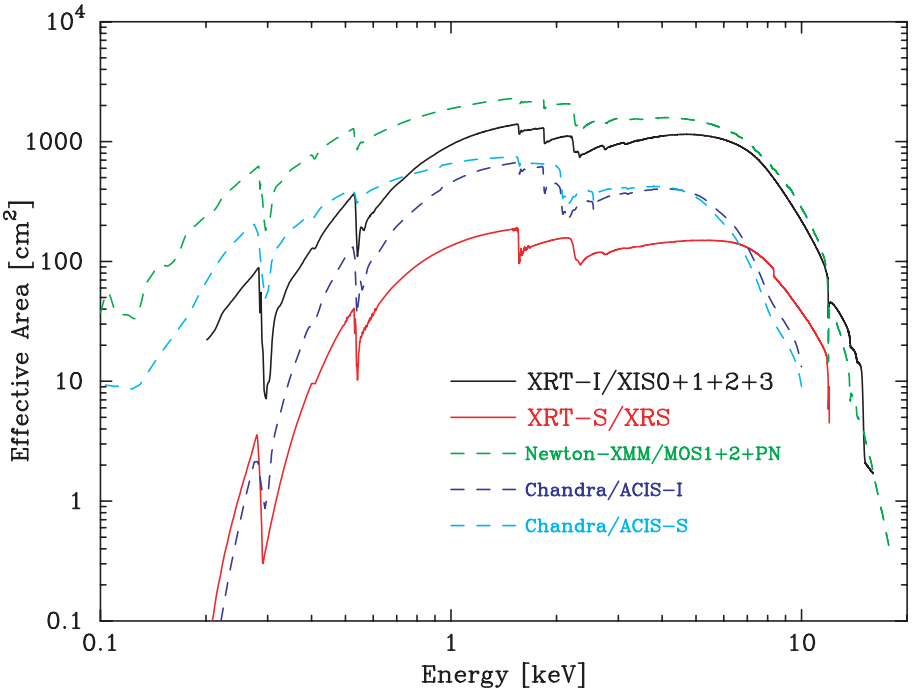

Figure 3.4: Effective areas of the four XRT modules compared with that of XMM-Newton and Chandra. The quantum efficiency of the CCD, and the transmissions of the thermal shield and the optical blocking filter are all taken into account (Serlemitsos et al., 2007).

Figures 3.6 show images of a point-like X-ray source, SS Cyg, obtained with the XRT + XIS system. The angular resolution of the XRT-I0 through I3 is 1.′8, 2.′3, 2.′0, and 2.′0 in Half-Power Diameter (HPD), respectively. The sky position of a point source can be determined within a 90% error circle with a radius of 19" (Uchiyama et al., 2008).

3.3 X-ray Imaging Spectrometer (XIS)

3.3.1 Overview

Suzaku is equipped with four sets of CCD cameras (XIS0-3) (Koyama et al., 2007a). Each XIS is placed on the focal plane of the XRT. The overview of the XIS is shown in figure 3.7 and 3.8.

The imaging area is composed of pixels of 24×24 μm^2, which is arranged in an array of

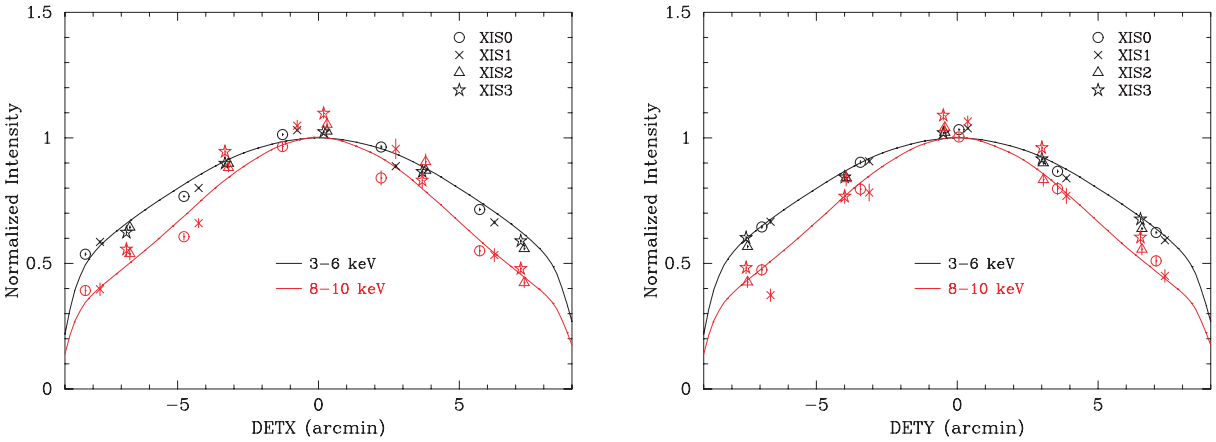

Figure 3.5: Relation between the effective area and the off-axis angle (vignetting) of the XRT-I modules using the data of the Crab Nebula in the 3–6 keV and 8–10 keV bands (Serlemitsos et al., 2007).

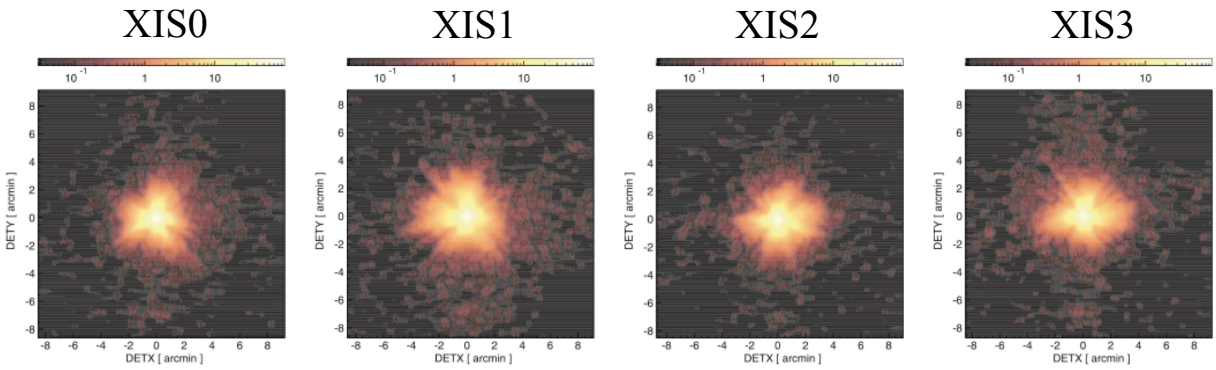

Figure 3.6: Point source images on the focal planes of the XRT-I modules. The images are smoothed with a Gaussian function of $\sigma = 3$ pixels, where the pixel size is 24 μm. (Serlemitsos et al., 2007).

1024×1024 pixels. The Field of View (F.o.V.) is $17\farcm8 \times 17\farcm8$. While the CCD consists of four segments (A, B, C, and D) with a dedicated readout node, there is no physical gap between the segments. For on-orbit calibration, ^{55}Fe calibration sources emitting a Mn Kα line (5.895 keV) are attached to illuminate the corners of XIS sensors (see figure 3.8). One side of the CCD is coated with the gate structure mainly made of Si and SiO_2 (front side). Front-Illuminated (FI) CCD detects X-rays that penetrate the gate structure, whereas the BI CCD detects X-rays coming from the back-side. XIS0, 2 and 3 are FI CCDs, while XIS1 is a BI CCD. Due to the absence of the gate structure, BI CCD reaches a high quantum efficiency even below ~ 1 keV. On the other hand, FI CCD have higher efficiency above 5 keV since the FI CCD employs thicker depletion layer than BI CCD (~ 65 μm for the FI CCD and ~ 42 μm for the BI CCD)

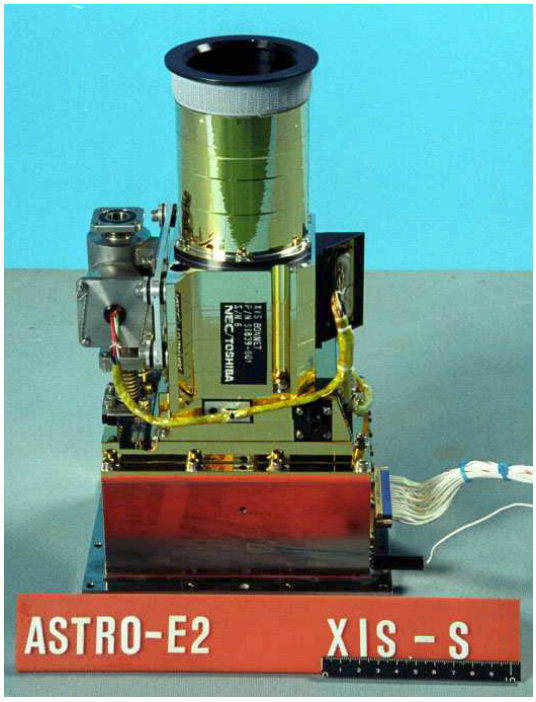

Figure 3.7: A picture of the XIS sensor (Koyama et al., 2007a).

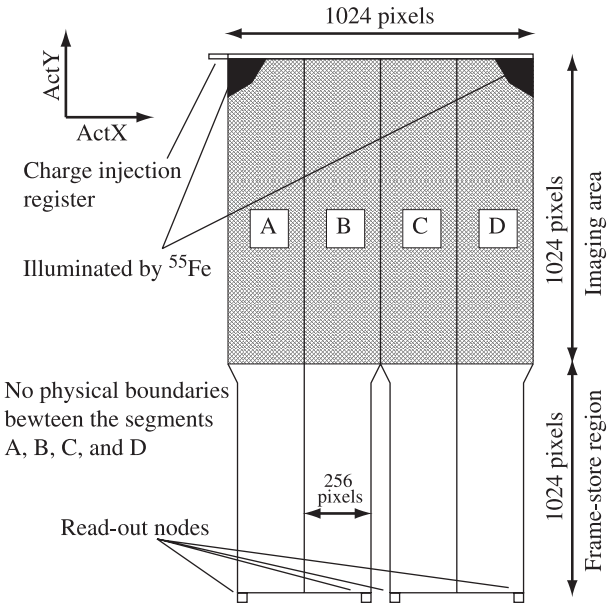

Figure 3.8: Schematic view of the XIS CCD (top view). The CCD consists of four segments (A, B, C, and D), each with a dedicated read-out node (Koyama et al., 2007a).

Figure 3.9 shows the quantum efficiency of the FI and BI CCDs of Suzaku.

3.3.2 Performance

When the XIS started the observation at first, the energy resolution was $\sim$ 130 eV at 6 keV in full width at half maximum (FWHM). However, CCDs are damaged by the radiation in a space environment, and increase the charge transfer inefficiency (CTI). It is mainly caused by charge traps, that capture signal carriers, generated by cosmic-rays. Since the capture of the charge occurs stochastically, the amount of the captured charge fluctuate and then the energy resolution becomes worse. To reduce the CTI, a spaced-row charge injection (SCI) technique has been adopted (Bautz et al., 2007; Uchiyama et al., 2009). By the SCI technique, small amounts of artificial charges are injected into the pixels. The injected charges fill traps and then the subsequent charges (signals) are transferred with less charge loss. The SCI has been a normal observation mode since October 2006. Figure 3.10 shows the long-term variety of the measured energy and width of the Mn Kα line (5.9 keV) emitted from the ^{55}Fe calibration sources. The energy resolution improved from $\sim$ 200 eV to $\sim$ 140 eV (Uchiyama et al., 2009) by the start of the SCI in October 2006.

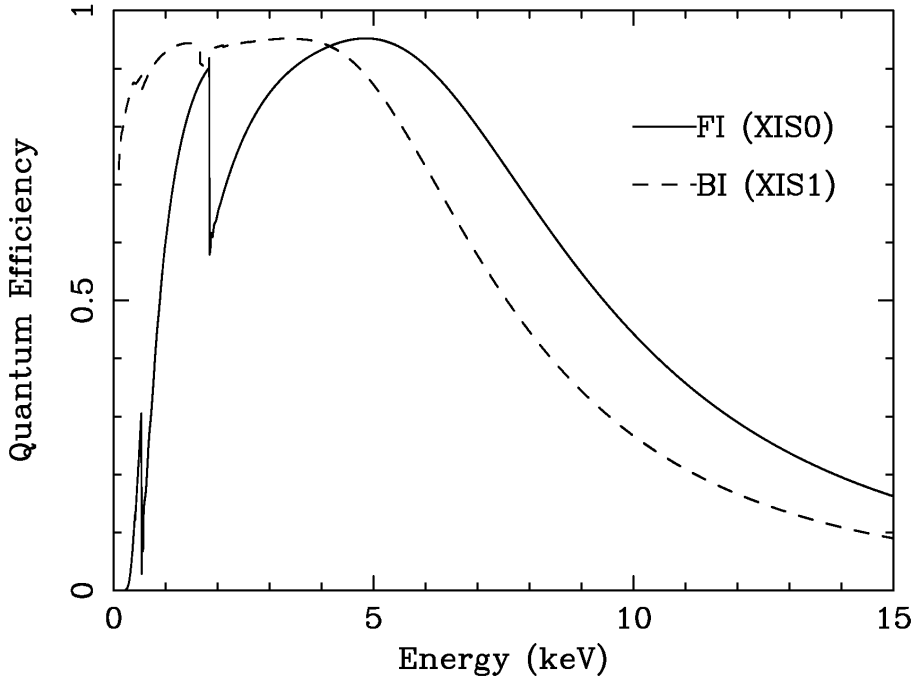

Figure 3.9: The quantum efficiency as a function of the incident energy. The solid and dashed lines represent that of the FI CCD (XIS0) and BI CCD (XIS1), respectively (Koyama et al., 2007a).

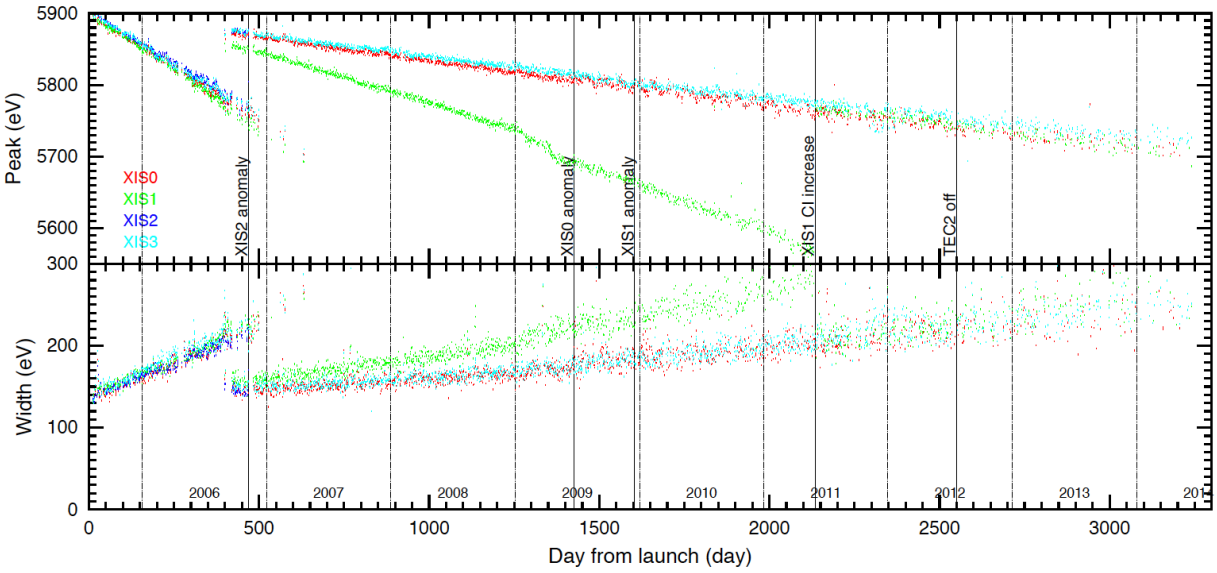

Figure 3.10: Long-term variety of the measured energy (top panel) and width (bottom panel) of the Mn Kα line emitted from the ^{55}Fe calibration sources (Suzaku Technical Description).

3.3.3 Non X-ray background

In the orbit, charged cosmic-ray particles and gamma rays produce background signals. In addition, fluorescence X-rays from the materials used in the spacecraft and the ^{55}Fe calibration

sources also produce the background. The background which is not caused by the celestial X-rays is called the Non X-ray Background (NXB). Figure 3.11 shows the NXB spectrum of each XIS sensor, except for the regions illuminated by the calibration sources. Major line structure is fluorescence lines from Al, Si, Mn, Ni and Au. The Mn Kα (5.9 keV) and Kβ (6.5 keV) lines are the scattered X-rays from the calibration sources. XIS0 shows relatively strong Mn K-shell lines. The background count rate is 0.1–0.2 counts s^{-1} (FI CCDs) and 0.3–0.6 counts s^{-1} (BI CCD) in the 0.4–12 keV band.

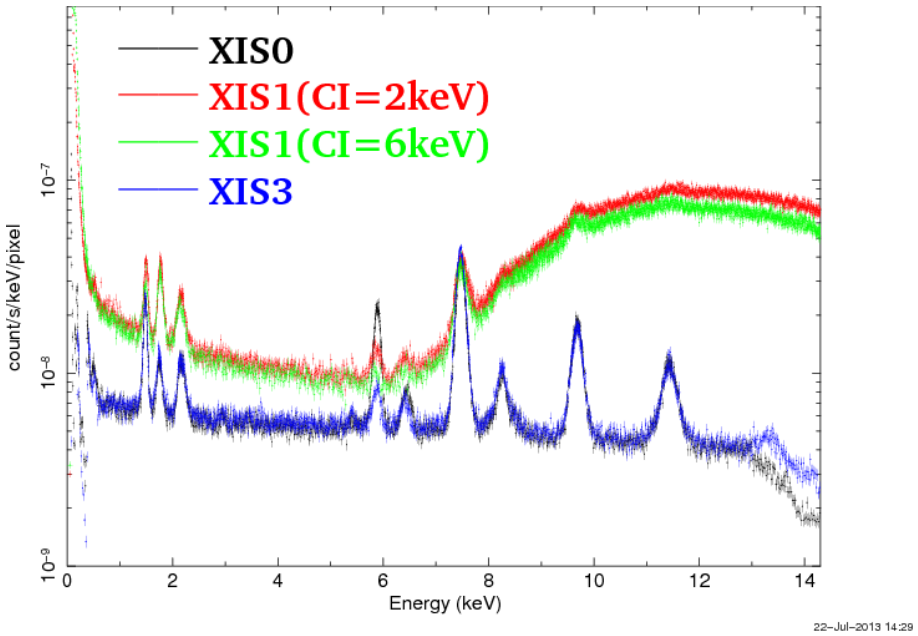

Figure 3.11: NXB count rate of XIS0 (black), XIS1 (red) and XIS3 (blue). The spectra were estimated from night Earth observations. The figure is taken from Suzaku technical description[2].

The NXB of the XIS is relatively low and stable compared with Chandra and XMM-Newton owing to the lower altitude of the orbit. The NXB can be estimated using the data obtained when the spacecraft is pointed toward the night-Earth. The count rate of the NXB anti-correlates with the geomagnetic cut-off rigidity. Figure 3.12 shows the relation between the NXB count rate and the cut-off rigidity. The NXB is modeled in Tawa et al. (2008) as a function of the position on the CCDs and the cut-off rigidity. The reproducibility of the model is 2.79–4.36% in the 5–12 keV band for each 5 ks exposure of the NXB data.

Owing to the large effective area, high energy resolution, and the low and stable NXB, the Suzaku XIS is the best instrument to investigate the diffuse X-ray emission especially in the high-energy band. Thus we used the Suzaku data to study the diffuse structure of the 6.4 keV line in SNRs.

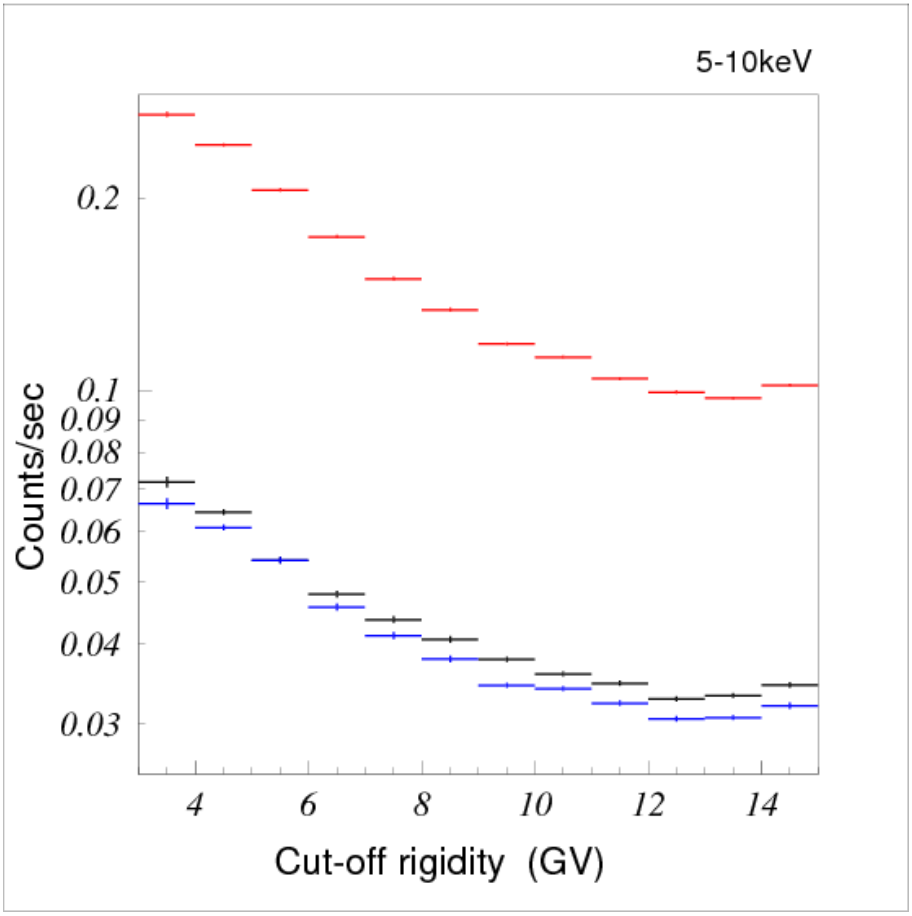

Figure 3.12: Relation between the NXB intensity in the 5–10 keV band and the cut-off rigidity. Black, red and blue data points show those of XIS0, 1 and 3, respectively. The figure is taken from Suzaku Technical Description.

Chapter 4

Observation and data reduction

4.1 Sample selection

To search for the 6.4 keV line and investigate the origin, we chose the SNRs based on three criteria as follows.

First, SNRs observed by Suzaku with enough exposure were selected. As described in section 1.2, the Suzaku XIS is the best instrument for this work. To obtain the data with enough statistics, the SNRs observed with an exposure more than 15 ks were chosen.

Next, the SNRs locate on the Galactic plane were picked-up. To emit the non-thermal 6.4 keV line, target material containing low-ionized iron is necessary independent on the emission mechanism. From this point of view, SNRs locate on the Galactic plane are expected to exhibit stronger 6.4 keV line. For this reason, the SNRs along the Galactic plane of $|b| < 1.^{\circ}0$ were selected. So far, no SNRs showing the non-thermal 6.4 keV line have been reported in the western side of the Galactic plane. Thus all SNRs in the western side of the Galactic plane ($l > 180^{\circ}$) were selected.

As shown in section 2.2.1, thermal plasma can emit the Fe Kα line. Since the Fe Kα line emitted via thermal processes can be a contamination of our analysis. The Fe Kα intensity emitted from thermal plasma with a temperature lower than 1 keV is negligible. Thus the SNRs which are known to have thermal plasma with the temperature higher than 1 keV were removed from our sample.

After the selection, 11 SNRs meet the criteria; G290.1−0.8, G298.6−0.0, G304.6+0.1, G323.7−1.0, G330.2+1.0, G346.6−0.2, G348.5+0.1, G348.7+0.3, G355.6−0.0, G359.0−0.9 and G359.1−0.5. In this thesis, the 6.4 keV line emission is searched for these 11 SNRs at first. Then detailed analyses are performed for the SNRs which show significant excess in the 6.4 keV line.

4.2 Previous research for the sample SNRs

Table 4.1 and 4.2 show the property of the sample SNRs revealed in the previous researches. The SNR names are listed in the first column of each table. In table 4.1, the second column shows the previous research in which the object was identified as an SNR at first. The size of and the flux of the SNR in the radio continuum at 1 GHz is summarized in the third and fourth columns, respectively. Table 4.1 also shows the property of the X-ray emitting thermal plasma; the ionization state (fifth column) and the electron temperature (sixth column). The last column summarizes the presence of gamma-ray emission in the GeV and/or TeV bands. Table 4.2 summarizes the SNR age, the progenitor type, and the confirmation of the interaction between molecular clouds.

Table 4.1: Summary of the previous researches for the SNRs

SNR name	Discover[1]	Size[2]	Radio flux[3]	Thermal X-ray[4]	Temperature[5]	Gamma-ray[6]
G290.1−0.8	[7]	19×14	42	IP[15]	0.57–0.89[15]	GeV[25]
G298.6−0.0	[8]	12×9	5	CIE[16]	$0.78^{+0.09}_{-0.08}$[16]	GeV[26]
G304.6+0.1	[8]	8	14	RP[17]	0.73 ± 0.03[17]	GeV[26]
G323.7+1.0	[9]	51×38[22]	> 0.61[22]	–	–	GeV[27], TeV[28]
G330.2+1.0	[10]	11	5	CIE[18]	$0.70^{+1.34}_{-0.32}$[18]	–
G346.6−0.2	[10]	8	8	RP[19]	$0.30^{+0.03}_{-0.01}$[19]	–
G348.5+0.1	[11]	15	72	RP[20]	$0.49^{+0.09}_{-0.06}$[20]	GeV[26], TeV[29]
G348.7+0.3	[11]	17	26	IP[21]	0.9 ± 0.2[21]	GeV[30], TeV[31]
G355.6−0.0	[12]	8×6	3	CIE[22]	0.56 ± 0.10[22]	–
G359.0−0.9	[13]	23	23	IP[23]	0.35 ± 0.03[23]	GeV[26]
G359.1−0.5	[14]	24	14	RP[24]	0.29 ± 0.02[24]	GeV[26]

[1] Previous research in which the object was identified as an SNR at first.
[2] Size of the radio shell at 1 GHz in the unit of arcmin (Green, 2014).
[3] Radio flux at 1 GHz in the unit of mJy arcmin^{-2} (Green, 2014).
[4] Ionization state of the X-ray plasma, indicated by "CIE", "IP", or "RP".
[5] Electron temperature of the X-ray plasma in the unit of keV.
[6] "GeV" means that gamma-rays coincident with the SNR have been detected in the GeV band.
"TeV" means the same but in the TeV band.
[7]Kesteven (1968), [8]Shaver & Goss (1970), [9]Green et al. (2014), [10]Clark et al. (1975), [11]Clark et al. (1975)
[12]Gray (1994b), [13]Downes et al. (1979), [14]Reich & Fuerst (1984), [15]García et al. (2012), [16]Bamba et al. (2016a)
[17]Washino et al. (2016), [18]Park et al. (2009), [19]Yamauchi et al. (2013), [20]Yamauchi et al. (2014), [21]Nakamura et al. (2009)
[22]Minami et al. (2013), [23]Bamba et al. (2009), [24]Ohnishi et al. (2011)
[25]Auchettl et al. (2015), [26]Acero et al. (2016), [27]Araya (2017), [28]Puehlhofer et al. (2015), [29]Aharonian et al. (2008c),
[30]Xin et al. (2016), [31]Aharonian et al. (2008b)

4.3 Observation and data reduction

Table 4.3 summarizes the observations for the SNRs analyzed in this thesis. The data obtained at the South Atlantic Anomaly, during the Earth occultation, and at a low elevation angles of

Table 4.2: Summary of the previous researches for the SNRs

SNR name	SNR age (yr)	SN type[4]	MC interaction[5]
G290.1−0.8	$10,000$–$20,000$[8]	CC[32]	possible[42]
G298.6−0.0	unknown	unclear	–
G304.6+0.1	$28,000$–$64,000$[9]	CC[33]	yes[43]
G323.7+1.0	unknown	unclear	–
G330.2+1.0	$1,000$–$1,200$[10]	CC[34]	–
G346.6−0.2	$14,000$–$16,000$[11]	unclear[11,35]	yes[44,45]
G348.5+0.1	$\sim 24,000$[12]	CC?[36]	yes[43]
G348.7+0.3	350–$3,150$[13]	unclear	yes[43]
G355.6−0.0	$\sim 20,000$[14]	unclear	–
G359.0−0.9	$\sim 9,700$[15]	unclear	–
G359.1−0.5	$\gtrsim 10,000$[16]	CC?[37]	yes[46]

[3] "GeV" means that gamma-rays coincident with the SNR have been detected in the GeV band. "TeV" means the same but in the TeV band.
[4] Progenitor type of the SNR; Core-Collapse(CC), type Ia (Ia), or unclear.
[5] If the SNR is confirmed to be interacted with molecular clouds (MCs), "yes". "possible" means that there are signs for the interaction.
[8]Slane et al. (2002), [9]Combi et al. (2010), [10]Park et al. (2009), [11]Yamauchi et al. (2013), [12]Yamauchi et al. (2014)
[13]Nakamura et al. (2009), [14]Minami et al. (2013), [15]Leahy (1989), [16]Bamba et al. (2000),[32]García et al. (2012)
[33]Washino et al. (2016), [34]Park et al. (2006), [35]Sezer et al. (2011a), [36]Yamauchi et al. (2013), [41]Giacani et al. (2009)
[42]Filipovic et al. (2005), [43]Frail et al. (1996), [44]Green et al. (1997), [45]Koralesky et al. (1998) [46]Lazendic et al. (2002)

$< 5^\circ$ from the night-earth rim and of $< 20^\circ$ from the day-earth rim, were excluded. We analyzed the data with the processing version of 3.0.22.43, using `HEAsoft` version 6.21. The XIS pulse-height data of each X-ray event were converted to Pulse Invariant (PI) channels using the `xispi` software and the calibration database released on 2016 Jun 7. The ancillary response files (arf) and redistribution files (rmf) were produced using `xissimarfgen` and `xisrmfgen` packages of `HEAsoft`, respectively.

Table 4.3: Summary of the Suzaku observations analyzed in this thesis.

SNR name	Obs.ID	Start time (UTC)	Exposure[1]	Pointing direction[2]
G290.1−0.8	506061010	2011/06/25 10:55:24	110.6	(290.°1195, −0.°7436)
G298.6−0.0	507037010	2012/08/11 20:26:45	17.2	(298.°5950, −0.°0841)
	507037020	2013/02/18 18:14:00	39.7	(298.°5919, −0.°0714)
G304.6+0.1	505074010	2010/09/03 21:54:15	99.6	(304.°5764, +0.°1308)
G323.7−1.0	508013010	2013/09/08 10:25:42	36.9	(323.°8857, −1.°1033)
	508014010	2013/09/09 00:31:34	38.9	(323.°5092, −0.°8166)
	508015010	2013/09/09 16:05:38	38.8	(323.°7331, −1.°3685)
	508016010	2013/09/10 04:19:22	42.2	(323.°8535, −0.°8132)
G330.2+1.0	504083010	2009/09/04 03:33:13	127.8	(330.°1401, +0.°9841)
	504083010	2009/09/07 11:38:35	30.9	(330.°1401, +0.°9843)
	504083010	2010/02/12 19:58:07	92.5	(330.°1835, +1.°0299)
G346.6−0.2	504096010	2009/10/07 16:54:31	56.8	(346.°6290, −0.°2222)
G348.5+0.1	504097010	2010/02/29 15:10:15	53.8	(348.°4422, +0.°0965)
G348.7+0.3	501007010	2006/08/27 01:27:07	82.9	(348.°6456, +0.°3768)
G355.6−0.0	504098010	2010/02/19 12:35:52	52.5	(355.°69101, −0.°0379)
G359.0−0.9	502017010[3]	2008/03/06 13:26:36	72.6	(359.°0475, −0.°6478)
	508057010	2014/03/04 23:05:56	49.8	(359.°0947, −0.°4452)
	508058010	2014/03/07 13:13:32	52.1	(358.°8810, −0.°8397)
	508059010	2014/03/08 19:36:03	53.5	(359.°0343, −1.°0595)
G359.1−0.5	502016010	2008/03/02 18:08:00	70.5	(358.°9171, −0.°4784)
	502017010[3]	2008/03/06 13:26:36	72.6	(359.°0475, −0.°6478)
	503012010	2008/09/14 19:35:07	57.7	(359.°0993, −0.°8700)

[1] Effective exposure of the screened data (ks).

[2] In the Galactic coordinate, $(l, b.)_{\mathrm{J2000.0}}$.

[3] The data of the observation 508057010 were used for both of the analysis for G359.0−0.9 and G359.1−0.5.

Chapter 5

Systematic search for 6.4 keV line in Galactic SNRs

5.1 Method of the systematic analysis

This chapter shows the analysis and results of the systematic search for the 6.4 keV line enhancement. To investigate the enhancement of the 6.4 keV line, all SNRs were systematically analyzed by the following way.

First, an X-ray image in the 6.3–6.5 keV band was created for each SNR. In the image, there should be diffuse structure. The structure is produced by a superposition of the X-ray intensity distribution which reflects the real stellar structure and the statistical fluctuation. To assess whether the enhancement is significant or not, two regions were defined; the "excess" region and the "reference" region. The excess region was defined to surround the bright part in the 6.3–6.5 keV band, while the reference region was defined as the other part.

To evaluate the excess quantitatively, 5–8 keV spectra were extracted from the excess and the reference regions. Since all SNRs in this thesis are located on the Galactic plane ($|b| < 1.^{\circ}0$), there should be emission lines of the GRXE (e.g. Yamauchi et al., 2016). The GRXE exhibits the lines of the Fe I Kα, Fe XXV Kα, Fe XXVI Kα and Fe I Kβ at 6.40 keV, 6.68 keV, 6.97 keV and 7.06 keV, respectively. Thus each spectrum was fitted with a model consisting of a power-law and four Gaussian functions. The energy centroid of each Gaussian was fixed to be the theoretical value (6.40 keV, 6.68 keV, 6.97 keV or 7.06 keV). The intensity of the Fe I Kβ line was fixed to 0.125 times that of the Fe I Kα line (Kaastra & Mewe, 1993), while those of the other lines were free parameters. The widths of the Gaussian functions were fixed to be zero, except for the Fe XXV Kα line. Since the Fe XXV Kα line is a blend of the resonance, inter-combination and forbidden lines, the line width was fixed to be 23 eV based on Koyama et al. (2007b). Both of the photon index and the normalization of the power-law function were

allowed to vary.

Since the SNRs in our sample locate on the Galactic plane, the spectra would be suffered from the interstellar absorption. However, the absorption has no significant effect in the 5–8 keV band, although the Fe K-shell absorption edge is at 7.112 keV. Therefore the absorption column density was fixed to the value of the GRXE (4.22×10^{22} cm^{-2}) or the GCXE (5.59×10^{22} cm^{-2}) obtained in Uchiyama et al. (2013) assuming the solar abundance obtained in (Anders & Grevesse, 1989). G359.0−0.9 and G359.1−0.5 locate in the Galactic center region and thus the absorption column density was fixed to 5.59×10^{22} cm^{-2}. In the spectral fitting of the other SNRs, the column density was set to 4.22×10^{22} cm^{-2}.

The spectral fitting was performed using `XSPEC` (Arnaud, 1996). For the fitting, the data points of the spectra were binned so that each bin contains at least 20 events. Through the spectral fitting, the 6.4 keV line intensities in the excess region and the reference region were obtained. Then the significance level of the 6.4 keV line excess was calculated by comparing the line intensities in the excess region and the reference region.

More detailed explanation of the analysis is described in section 5.2, taking G290.1−0.8 for an example.

5.2 G290.1−0.8

X-ray images

First, XIS images were created in the 0.5–3 keV, 5–8 keV and 6.3–6.5 keV bands. XIS1 (BI-CCD) data were not used to make the images above 5 keV, since the signal-to-noise ratio in the hard band is worse than that of the FI-CCDs. The corners of the CCD chips illuminated by the ^{55}Fe calibration sources were excluded from the images above 5 keV. Then NXBs were estimated from the data within ±150 days of the observation using `xisnxbgen` (Tawa et al., 2008), and were subtracted from the images. After the NXB subtraction, each image was divided by an exposure map simulated using the XRT+XIS simulator `xissim` (Ishisaki et al., 2007) for vignetting corrections. Figures 5.1 show the NXB subtracted and exposure corrected XIS images of G290.1−0.8 in the 0.5–3 keV (a), 5–8 keV (b) and 6.3–6.5 keV (c) bands. The 0.5–3 keV and 5–8 keV bands images are binned with 8×8 pixels and then smoothed with a Gaussian function of $\sigma = 3$ bins. The 6.3–6.5 keV band image is binned with 32×32 pixels and then smoothed with a Gaussian function of $\sigma = 6$ bins.

In the 0.5–3 keV band, diffuse X-ray emission can be seen. The soft X-rays correspond to the previously known thermal emission. On the other hand, there is no clear structure in the 5–8 keV band. This is consistent with the previous research: the temperature of the thermal plasma is low with 0.6–0.9 keV. In the 6.3–6.5 keV band, diffuse structure is seen.

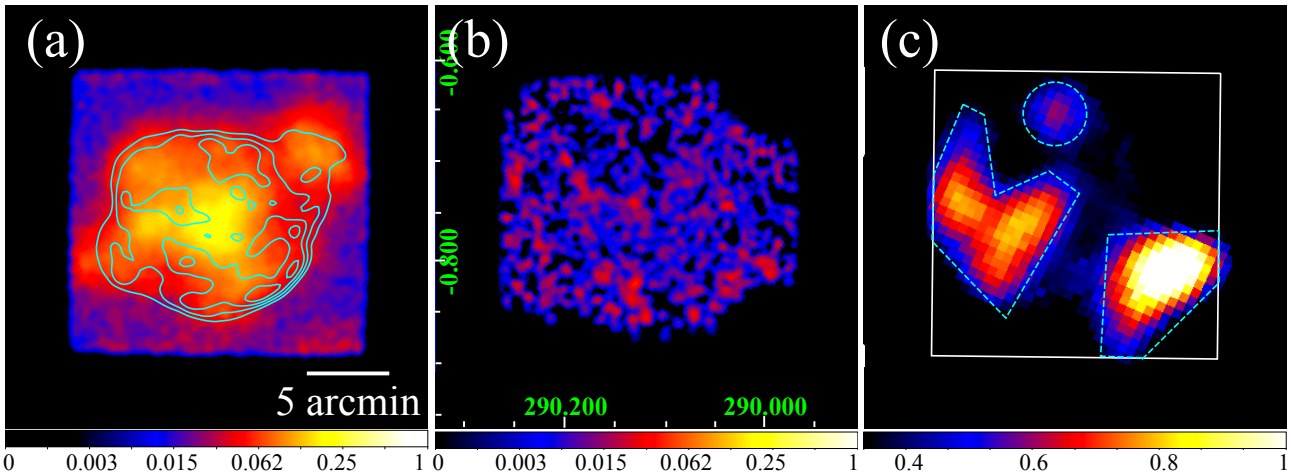

Figure 5.1: (a) : XIS0+1+3 image of G290.1−0.1 in the 0.5–3 keV band. The image is binned with 8×8 pixels and then smoothed with a Gaussian function of $\sigma = 3$ bins. The cyan contours show the 843 MHz radio continuum intensity (Whiteoak & Green, 1996). (b) : XIS0+3 image in the 5–8 keV band. The size of the binning and smoothing are the same with that of (a). (c) : XIS0+3 image in the 6.3–6.5 keV band. The image is binned with 32×32 pixels and then smoothed with a Gaussian function of $\sigma = 6$ bins. The areas surrounded with the white dashed curves are the "excess" region, while the whole field except for the excess region is the "reference" region.

X-ray spectra

To assess whether the enhancement is a real structure or not, the "excess" region and the "reference" region were defined. The excess region was defined to surround the bright part in the 6.3–6.5 keV band as illustrated with dashed lines in figure 5.1(c). The whole field except for the excess region was defined as the reference region. X-ray spectra were extracted from the excess and reference regions. Although the excess region consists of three separated parts, the data extracted from all areas were added to improve the statistics. Then, the spectra of XIS0 and 3 were combined altogether.

Figures 5.2 show the XIS0+3 spectra (Black data points) with the NXB spectra (Red data points). Here the NXB spectra were estimated using `xisnxbgen` based on the data between ±300 days from the observation. The spectra after the NXB subtraction are plotted in the bottom panels. In particular the NXB subtracted spectrum of the reference region shows residuals with an "S" like shape around the instrumental Ni Kα line at 7.5 keV. The residuals arise due to the difference in the centroids of the Ni Kα lines between the data and the NXB. The difference is caused by the uncertainty of the response for the NXB spectrum.

The results of the following spectral analysis can be affected by the residuals. Thus the NXB

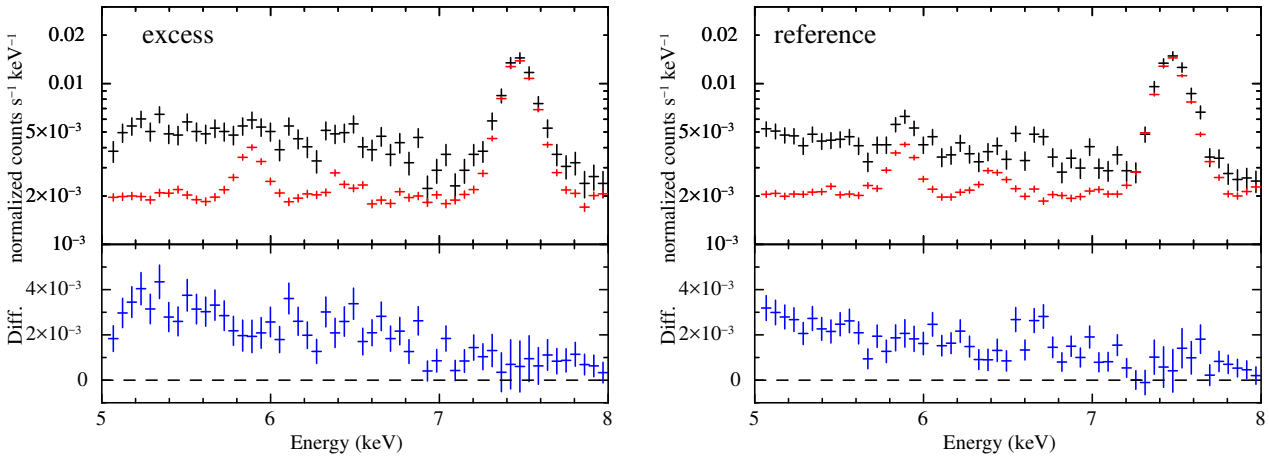

Figure 5.2: *Top panels* : Comparison of the 5–8 keV spectra between that extracted from the regions (red) and NXB (blue). The left and right panels show the spectra of the excess region and the reference region, respectively. *Bottom panels* : The data spectra after the NXB subtraction.

spectra were shifted and re-normalized as follows. First, the data spectrum was fitted with a power-law plus Gaussian function in the 7–8 keV band. Here the Gaussian function represents the Ni Kα line, and hence the width was fixed to be zero. Then the best-fit values of the energy centroid and the normalization of the Gaussian function were obtained. In the same way, the energy centroid and the normalization for the Ni Kα line in the NXB spectrum were obtained. In the case of the spectrum of the reference region, for example, the best-fit centroids of the Gaussian function were 7.486 keV for the data spectrum and 7.478 keV for the NXB spectrum. Since the energy scale of the XIS is 3.65 eV/PI-channel, the NXB spectrum was shifted for the lower energy with $(7486 - 7478)/3.65 = 2$ channels. The normalizations of the Gaussian functions were 3.07×10^{-4} for the data spectrum and 3.01×10^{-4} for the NXB spectrum. Thus we multiplied the NXB spectrum by a factor of $(3.07 \times 10^{-4})/(3.01 \times 10^{-4}) = 1.02$. The comparison of the spectra between the data and the NXB after the shift and the re-normalization are shown in figures 5.3. In the same way, the shift and the normalization factor for the NXB spectrum of the excess region were obtained as 1 channel and 0.98, respectively.

The NXB subtracted spectra were fitted with the model consisting of a power-law and four Gaussian functions. The details of the model are shown in section 5.1. Figures 5.4 show the spectra fitted with the phenomenological model. Both of the spectra of the excess region and the reference region are well represented by the model with $\chi^2_{\rm red} = 0.87$ (48 d.o.f.) (excess region) and $\chi^2_{\rm red} = 0.76$ (44 d.o.f.) (reference region). The best-fit parameters are summarized in table 5.1. The intensity of the power-law component is significantly higher in the excess region than the reference region. The photon index of the power-law component is smaller in the excess region than the reference region. The intensities of the Fe I, Fe XXV and Fe XXVI

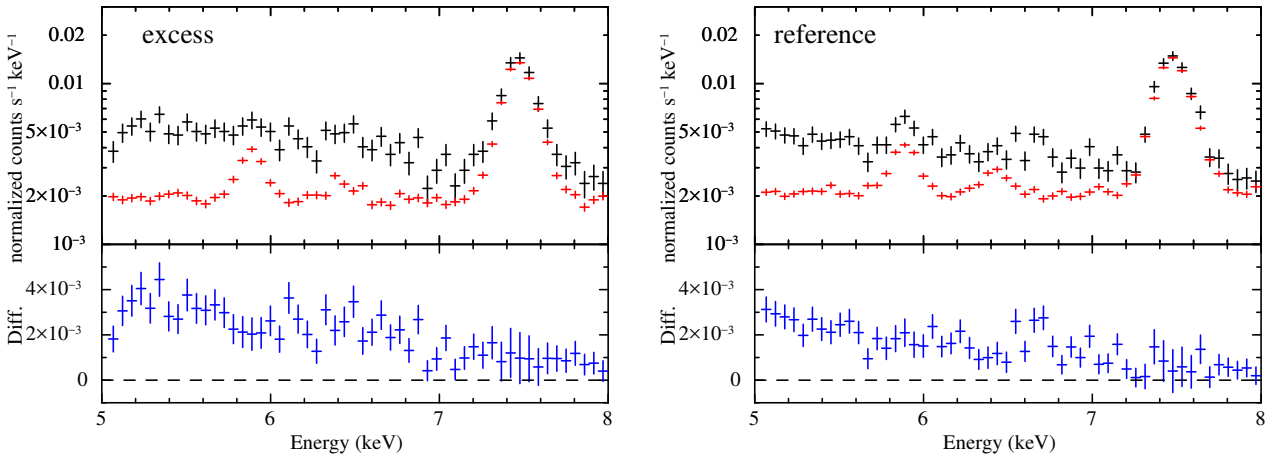

Figure 5.3: The composition is the same as that of figures 5.2, but the NXB spectra are shifted and re-normalized.

Kα lines are all consistent between the excess and reference regions. In both of the excess and the reference regions, we obtained only upper limits for the Fe I Kα intensities within the 90 % confidence level.

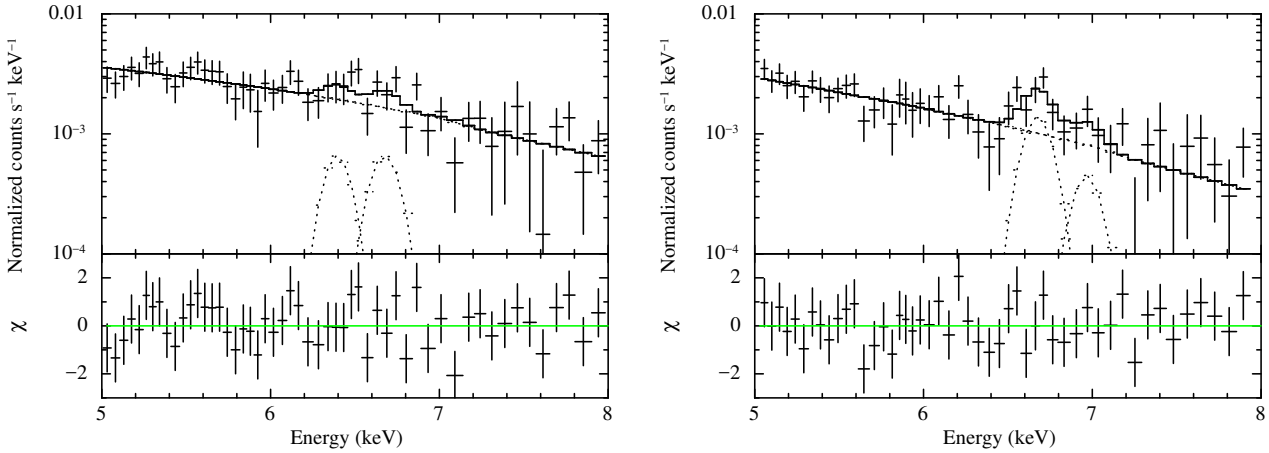

Figure 5.4: Top panels: 5–8 keV spectra extracted from the excess (left panel) and the reference (right panel) regions, fitted with the power-law plus four Gaussian functions model. The vertical axes are normalized with the areas of the regions. The best-fit models are plotted with the solid lines, while each component is plotted with the dotted line. Bottom panels: Residuals between the data and the best-fit models.

5.3 G298.6−0.0

X-ray images

Figures 5.5 show the NXB subtracted and exposure corrected XIS images of G298.6−0.0 in the 0.5–3 keV (a), 5–8 keV (b) and 6.3–6.5 keV (c) bands. The 0.5–3 keV and 5–8 keV bands

Table 5.1: Best-fit parameters for the excess and reference regions of G290.1−0.8

Parameter	Best-fit value	
	Excess region	Reference region
Power-law photon index	$2.1^{+0.7}_{-0.6}$	$3.2^{+1.0}_{-0.9}$
Power-law intensity[1]	38 ± 3	26 ± 3
Fe I Kα Intensity[2]	< 1.8	< 0.4
Fe XXV Kα Intensity[2]	< 2.0	2.0 ± 0.8
Fe XXVI Kα Intensity[2]	< 0.5	< 1.5

[1] Observed intensity in the 5.0–8.0 keV band in the unit of photons cm^{-2} s^{-1} arcmin^{-2}.
[2] Observed intensity in the unit of 10^{-8} photons cm^{-2} s^{-1} arcmin^{-2}.

images are binned with 8×8 pixels and then smoothed with a Gaussian function of $\sigma = 3$ bins. The 6.3–6.5 keV band image is binned with 32×32 pixels and then smoothed with a Gaussian function of $\sigma = 6$ bins.

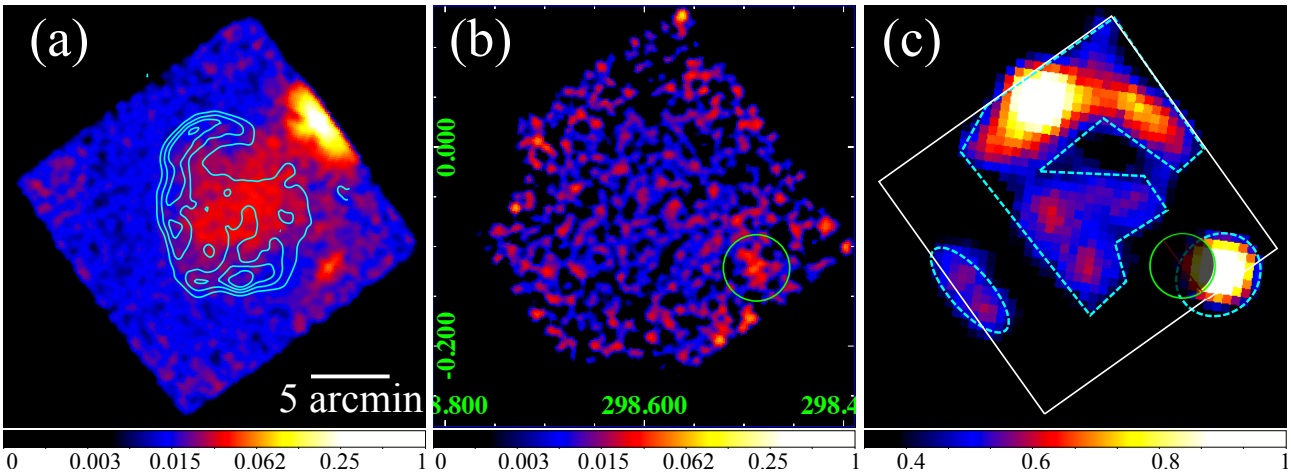

Figure 5.5: (a) : XIS0+1+3 image of G298.6−0.0 in the 0.5–3 keV band. The image is binned with 8×8 pixels and then smoothed with a Gaussian function of $\sigma = 3$ bins. The cyan contours show the 843 MHz radio continuum intensity (Whiteoak & Green, 1996).(b) : XIS0+3 image in the 5–8 keV band. The size of the binning and smoothing are the same as that of (a). (c) : XIS0+3 image in the 6.3–6.5 keV band. The image is binned with 32×32 pixels and then smoothed with a Gaussian function of $\sigma = 6$ bins. The areas surrounded by the dashed curves are the "excess" region, while the whole field except for the excess region and the point-like source seen in the 5–8 keV band image is the "reference" region.

A bright X-ray source is seen at the northwestern rim of the 0.5–3 keV band image. The source is coincident with 1RXS J121248.7−623027. In addition, diffuse emission filling the radio shell is seen. The spatial nature of the diffuse X-ray emission is consistent with the previously known thermal emission. In the 5–8 keV band, a faint point-like source is seen at

$(l, b) = (298.^\circ4871, -0.^\circ1215)$ as surrounded by a green circle. The source is called the hard point-like source hereafter. The point-like source is also seen in the 0.5–3 keV band. In the 6.3–6.5 keV band, extended structure is seen. A part of the structure is positionally coincident with the thermal X-ray emission seen in the 0.5–3 keV band. However, the brightest part of the 6.3–6.5 keV band emission is apart from the thermal X-ray emission.

X-ray spectra

The excess region and the reference region were defined as areas illustrated with dashed lines in figure 5.5(c). The hard point-like source can be a contamination in the spectral analysis. Thus a circular region centroids on the hard point-like source was removed with a radius of $2'$. The areas surrounded by the dashed curves in figure 5.5(c) except for the circle centroids on the hard point-like source was defined as the excess region. The whole field except for the excess region and the point-like source was defined as the reference region.

The XIS0+3 spectra were extracted from the excess and the reference regions. The NXB was estimated using the data within ±300 days of the observation and then subtracted from each spectrum. Each spectrum was fitted with the model consisting of a power-law and four Gaussian functions described in section 5.1. Figures 5.6 show the NXB subtracted spectra of the excess and the reference regions, with the best-fit models. Both of the model fittings are statistically acceptable with $\chi^2_{\rm red} = 0.97$ (33 d.o.f.) for the excess region and $\chi^2_{\rm red} = 1.10$ (30 d.o.f.) for the reference region. The best-fit parameters are summarized in table 5.2. All of the parameters are consistent between the excess and the reference regions. In both of the regions, only upper limits were obtained for the Fe I Kα line intensity within the 90 % confidence level.

Table 5.2: Best-fit parameters for the excess and reference regions of G298.6−0.0

Parameter	Best-fit value	
	Excess region	Reference region
Power-law photon index	$2.2^{+1.7}_{-1.4}$	$2.1^{+1.3}_{-1.2}$
Power-law intensity[1]	22^{+5}_{-4}	27 ± 4
Fe I Kα Intensity[2]	< 2.0	< 0.6
Fe XXV Kα Intensity[2]	< 1.7	< 2.6
Fe XXVI Kα Intensity[2]	1.8 ± 1.3	< 0.4

[1] Observed intensity in the 5.0–8.0 keV band in the unit of photons cm^{-2} s^{-1} arcmin^{-2}.
[2] Observed intensity in the unit of 10^{-8} photons cm^{-2} s^{-1} arcmin^{-2}.

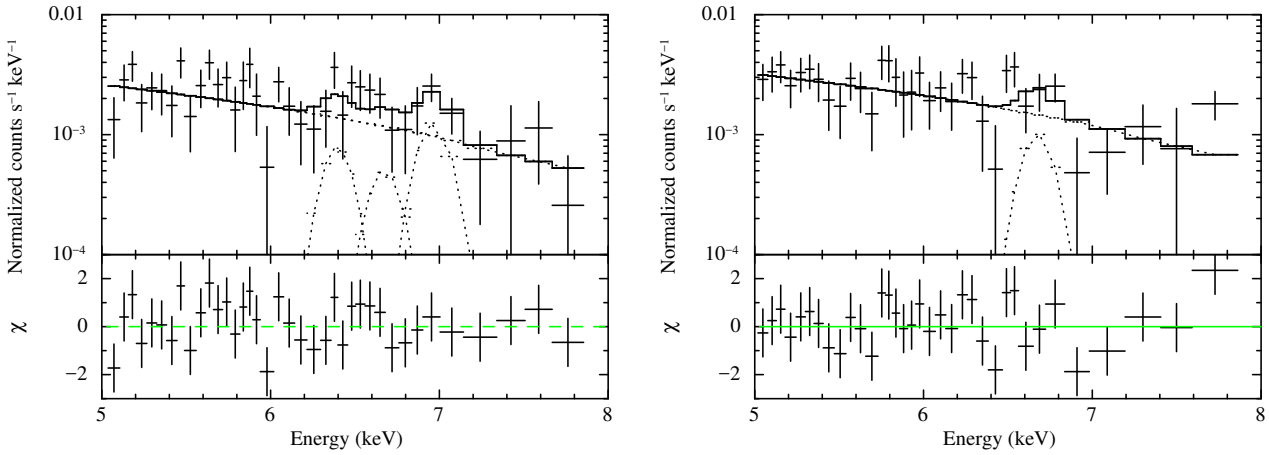

Figure 5.6: Top panels: NXB subtracted spectra of G298.6−0.0 extracted from the excess (left) and reference (right) regions, fitted with the power-law plus four Gaussian functions models in the 5–8 keV band. The vertical axes are normalized with the areas of the regions.The best-fit models are plotted with the solid lines, while each component is plotted with the dotted line. Bottom panels: Residuals between the data and the best-fit models.

5.4 G304.6+0.1

X-ray images

Figures 5.7 show the NXB subtracted and exposure corrected XIS images of G304.6+0.1 in the 0.5–3 keV (a), 5–8 keV (b) and 6.3–6.5 keV (c) bands. The 0.5–3 keV and 5–8 keV bands images are binned with 8×8 pixels and then smoothed with a Gaussian function of $\sigma = 3$ bins. The 6.3–6.5 keV band image is binned with 32×32 pixels and then smoothed with a Gaussian function of $\sigma = 6$ bins.

In the 0.5–3 keV band image, diffuse emission coincident with the radio continuum emission is seen. The soft X-rays correspond to the previously known thermal emission. In the 5–8 keV band, a point-like source is seen as surrounded by a green circle in figure 5.7(b). The source is coincident with the X-ray source 3XMM J130635.2−624619. In the 6.3–6.5 keV band, structure with an "S" like shape is seen.

X-ray spectra

Since 3XMM J130635.2−624619 can be a contamination in the spectral analysis, a circular region centroids on the source was removed with a radius of $2'$. The excess region was defined as an area surrounded by the dashed lines except for the circle centroids on 3XMM J130635.2−624619 (see figure 5.7(c)) The whole field except for the excess region and 3XMM J130635.2−624619 was defined as the reference region.

The XIS0+3 spectra were extracted from the excess and the reference regions. The NXB

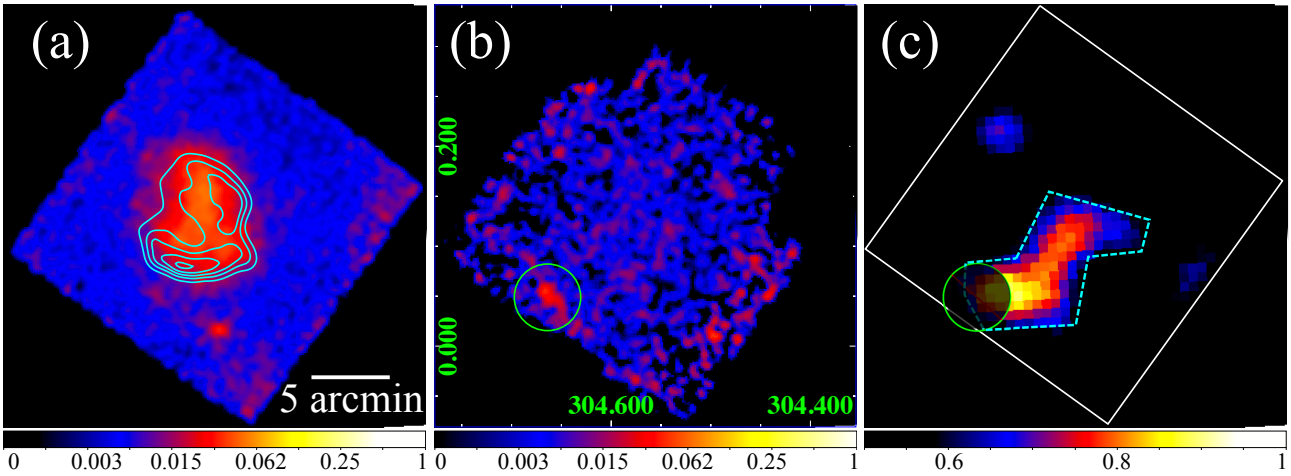

Figure 5.7: (a) : XIS0+1+3 image of G304.6+0.1 in the 0.5–3 keV band. The image is binned with 8×8 pixels and then smoothed with a Gaussian function of $\sigma = 3$ bins. The cyan contours show the 843 MHz radio continuum intensity (Whiteoak & Green, 1996). (b) : XIS0+3 image in the 5–8 keV band. The size of the binning and smoothing are the same as that of (a). (c) : XIS0+3 image in the 6.3–6.5 keV band. The image is binned with 32×32 pixels and then smoothed with a Gaussian function of $\sigma = 6$ bins. The areas surrounded with the dashed curves are the "excess" region, while the whole field except for the excess region and the point-like source seen in the 5–8 keV band image is the "reference" region.

was estimated using the data within ±300 days of the observation and then subtracted from each spectrum. Each spectrum was fitted with the model consisting of a power-law and four Gaussian functions described in section 5.1. Figures 5.8 show the NXB subtracted spectra of the excess and the reference regions with the best-fit models. Both of the model fittings are statistically acceptable with $\chi^2_{\rm red} = 1.10$ (27 d.o.f.) for the excess region and $\chi^2_{\rm red} = 1.16$ (41 d.o.f.) for the reference region. The best-fit parameters are summarized in table 5.3.

Table 5.3: Best-fit parameters for the excess and reference regions of G304.6+0.1

Parameter	Best-fit value	
	Excess region	Reference region
Power-law photon index	$2.9^{+1.4}_{-1.1}$	$2.5^{+0.8}_{-0.7}$
Power-law intensity[1]	39 ± 6	32 ± 3
Fe I Kα Intensity[2]	4.2 ± 1.6	< 1.0
Fe XXV Kα Intensity[2]	2.4 ± 1.5	2.4 ± 0.8
Fe XXVI Kα Intensity[2]	< 3.0	< 1.1

[1] Observed intensity in the 5.0–8.0 keV band in the unit of photons cm^{-2} s^{-1} arcmin^{-2}.
[2] Observed intensity in the unit of 10^{-8} photons cm^{-2} s^{-1} arcmin^{-2}.

The intensity of the Fe I Kα line in the excess region is significantly higher than that in the

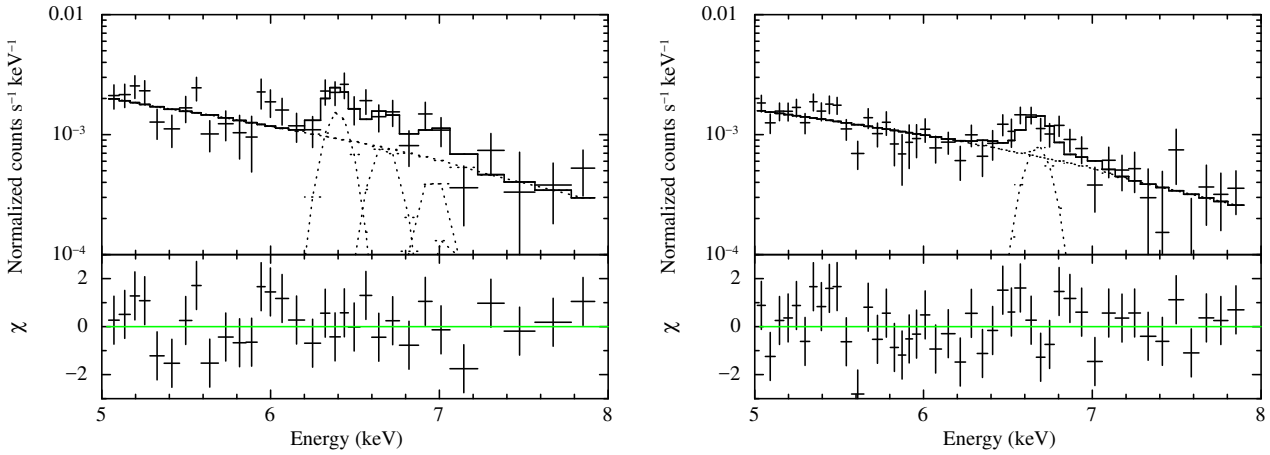

Figure 5.8: Top panels : NXB subtracted spectra of G304.6+0.1 extracted from the excess (left) and reference (right) regions, fitted with the power-law plus four Gaussian functions models in the 5–8 keV band. The vertical axes are normalized with the areas of the regions. The best-fit models are plotted with the solid lines, while each component is plotted with the dotted line. Bottom panels: Residuals between the data and the best-fit models.

reference region. The significance level of the excess is 3.6σ. The intensities of the other two lines, on the other hand, are consistent between the regions. The photon index of the power-law component is also consistent with each other. Although there is a sign that the intensity of the power-law component in the excess region is higher than that in the reference region, the significance level of the difference is not so high with 1.7σ.

5.5 G323.7−1.0

G323.7−1.0 has a large and extremely faint radio shell, and hence would not be a young SNR. Based on the angular size of the radio shell ($\sim 45'$) and the distance from the solar system [5 kpc][] (Araya, 2017), the radius of the radio shell is estimated to be 33 pc. Using the Sedov solution (see equation 2.6) assuming the explosion energy of 1×10^{51} erg and the number density of the interstellar matter of 1H cm^{-3}, the age of G323.7−1.0 is estimated to be 10^5 yr.

No significant X-rays have been detected from G323.7−1.0 so far. We, therefore, searched for X-ray emission, thermal and/or non-thermal, from G323.7−1.0. Suzaku observed four regions of G323.7−1.0. Figure 5.9 shows the fields of view of the XIS on the 843 MHz radio image of G323.7−1.0 (Green et al., 2014). The Suzaku observations caught the eastern part of the radio shell. Suzaku did not observe the brightness peaks of the GeV and TeV gamma-ray emissions as shown with the white cross point and the contours in figure 5.9, respectively.

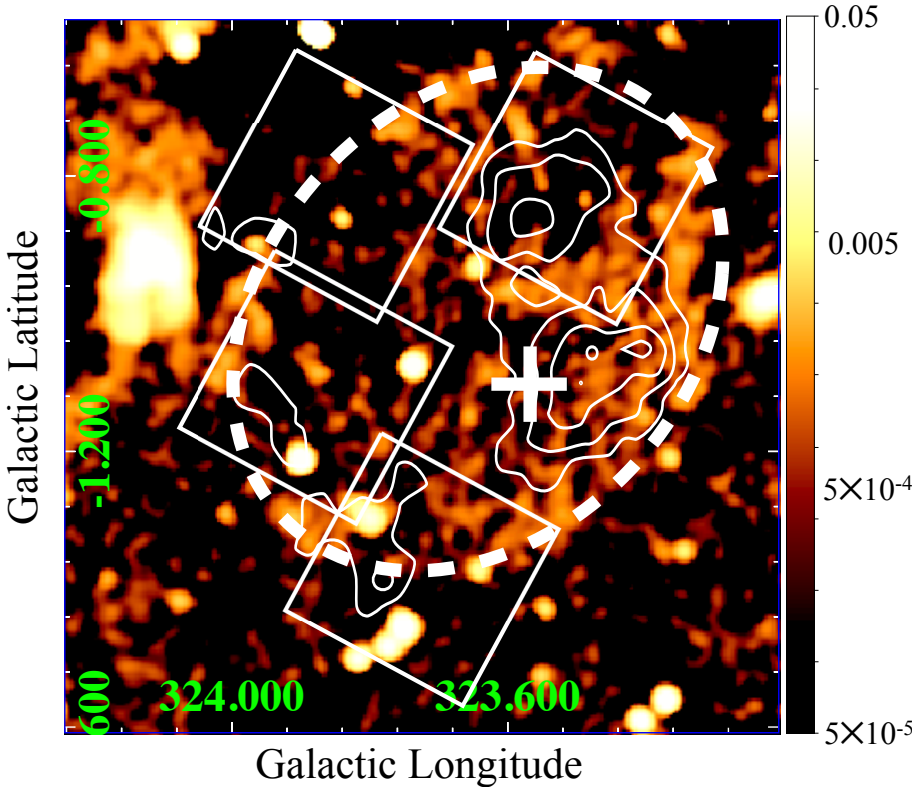

Figure 5.9: Suzaku XIS fields of view (white solid boxes) of the observations for G323.7−1.0 on the 843 MHz radio map taken from SkyView (https://skyview.gsfc.nasa.gov/). The while dashed ellipse indicates the approximate shape of the radio shell. The contours show the surface brightness map of > 1 TeV gamma-rays (Puehlhofer et al., 2015). The cross point shows the brightness peak position of the GeV gamma-ray emission (Araya, 2017).

5.5.1 X-ray images

Three panels in Figure 5.10 show the NXB subtracted and exposure corrected images in the 0.5–3 keV, 5–8 keV and 6.3–6.5 keV bands. The NXBs were estimated using the data within ±300 days from the observation. The 0.5–3 keV and 5–8 keV band images are binned with 8×8 pixels and then smoothed with a Gaussian function of $\sigma = 5$ bins. The 6.3–6.5 keV band image is binned with 32×32 pixels and then smoothed with a Gaussian function of $\sigma = 10$ bins.

In the 0.5–3 keV band image, there are several point-like sources marked with solid small circles, while a diffuse structure, indicated by the largest solid circle with a diameter of $8'.4$, is found in the southern field. This diffuse structure is called "the soft source" hereafter. On the other hand, there is no prominent structure in the 5–8 keV band except for one point source that is also seen in the 0.5–3 keV band. In the 6.3–6.5 keV band, some structures are seen as marked with dashed curves. Because of their angular sizes of $\gtrsim 5'$, which is larger than the HPD of the XRT ($\sim 2'$), they should not be point sources, but diffuse sources. These sources

are hereafter called "the 6.4 keV clumps".

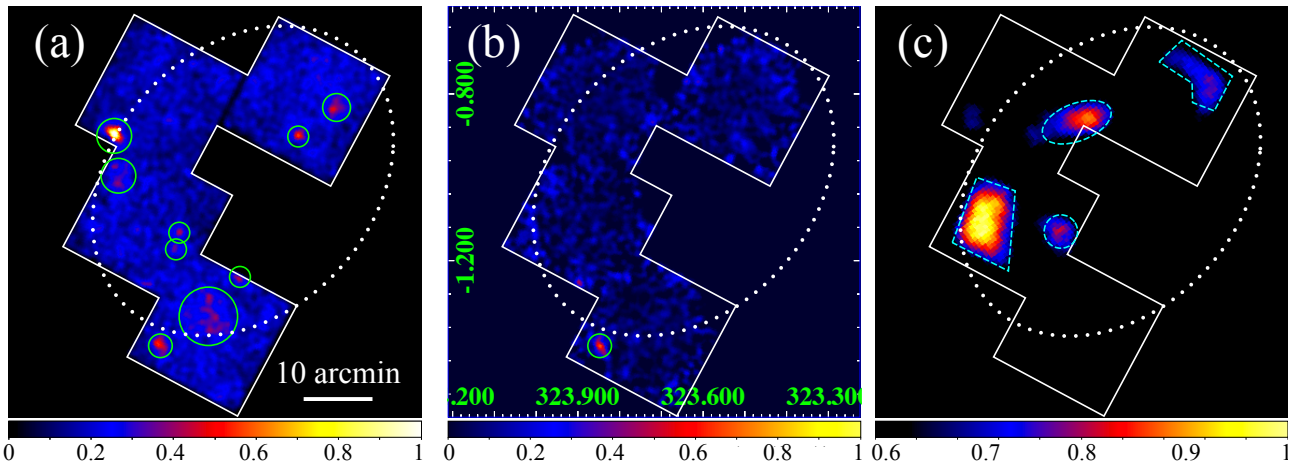

Figure 5.10: XIS images of G323.7−1.0 in the (a) 0.5–3 keV, (b) 5–8 keV and (c) 6.3–6.5 keV bands in the Galactic coordinates. The NXBs are subtracted and then the images are corrected the vignetting effect. The images (a) and (b) are binned with 8×8 pixels and then smoothed with a Gaussian function of $\sigma = 5$ bins. The image (c) is binned with 32×32 pixels and then smoothed with a Gaussian function of $\sigma = 10$ bins. The axes of the Galactic longitude and latitude are plotted on image (b). The largest dotted ellipse in each panel indicates the approximate shape of the radio shell (see figure 5.9)

5.5.2 X-ray spectra

The 6.4 keV clumps

In order to investigate the 6.4 keV clumps, the "excess region" was defined as illustrated with dashed curves in figure 5.10(c). The whole field excluding the soft source, the point sources and the excess region was defined as the reference region. XIS0 and 3 spectra were extracted from the excess and reference regions. Although the excess region consists of four parts, the data extracted from all areas were added to improve the statistics. The NXBs were estimated using the data within ±300 days of the observation, and were subtracted from the excess and reference spectra.

Figures 5.11 show the NXB subtracted spectra of the excess region and the reference region fitted with the power-law plus four Gaussian functions models. Both of the model fittings are statistically acceptable with $\chi^2_{\rm red} = 0.83$ (38 d.o.f.) for the excess region and $\chi^2_{\rm red} = 0.85$ (47 d.o.f.) for the reference region. The best-fit parameters are summarized in table 5.4. The 6.4 keV line intensity of the excess region is significantly higher than that of the reference

region. The significance level of the excess is 4.1σ. On the other hand, the other parameters are consistent between two regions.

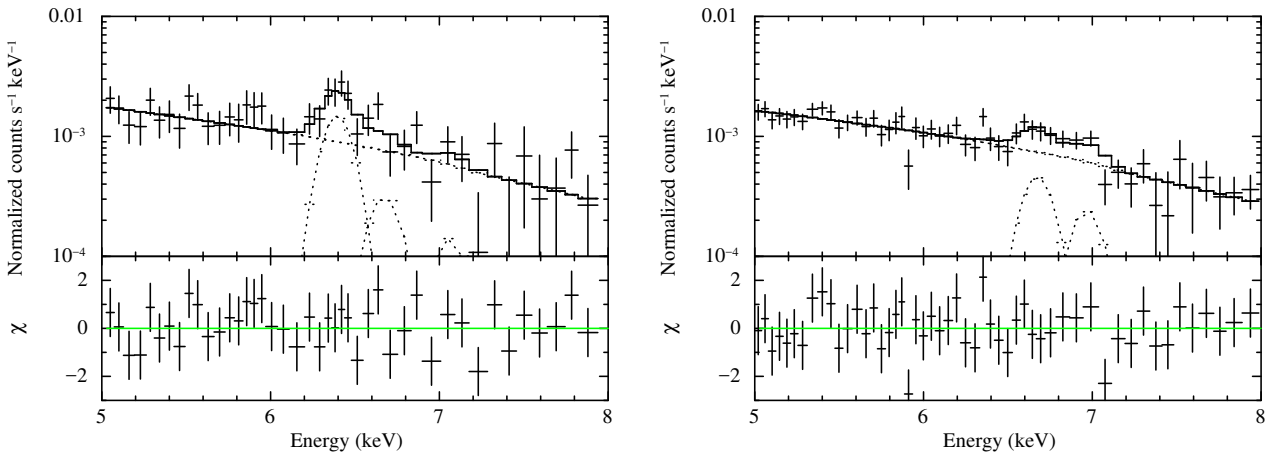

Figure 5.11: Top panels: XIS0 + 3 spectra extracted from the excess region (left) and the reference region (right) fitted with the model consisting a power-law and four Gaussian functions model. The best-fit models are plotted with the solid lines, while each component is plotted with the dotted line. The vertical axes are normalized by the ratio of the area including the vignetting correction. Bottom panels: Residuals between the data and the best-fit models.

Table 5.4: Best-fit parameters for the excess and reference regions of G323.7−1.0

Parameter	Best-fit value	
	Excess region	Reference region
Power-law photon index	$2.3^{+1.0}_{-0.9}$	$2.2^{+0.6}_{-0.5}$
Power-law flux[1]	37 ± 5	35^{+2}_{-3}
Fe I Kα Intensity[2]	4.3 ± 1.6	< 0.8
Fe XXV Kα Intensity[2]	< 2.4	1.5 ± 0.7
Fe XXVI Kα Intensity[2]	< 0.9	0.9 ± 0.7

[1] Observed intensity in the 5.0–8.0 keV band in the unit photons cm^{-2} s^{-1} arcmin^{-2}.
[2] Observed intensity in the unit of 10^{-8} photons cm^{-2} s^{-1} arcmin^{-2}.

The soft source

In order to investigate the soft source, we extracted an XIS0 + 3 spectrum from the largest solid circle in figure 5.10(a). The spectrum of the reference region was used as the background. Figure 5.12 shows the background-subtracted spectrum.

Although the spectrum has poor statistics, a hint of an emission line can be seen at $\sim$ 1.4 keV. We, then, tried fitting the spectrum with an optically-thin thermal plasma model (`APEC`) suffering from an interstellar absorption (`phabs`) fixing the metal abundance of a solar

value (Lodders, 2003). The model represents the spectrum well with the $\chi^2_{\rm red} = 0.44$ (8 d.o.f.). We obtained the plasma temperature $kT = 1.1^{+0.5}_{-0.3}$ keV and the absorption column density $N_{\rm H} = (1.8 \pm 0.6) \times 10^{22}$ cm^{-2} as well as the normalization $2.8^{+1.8}_{-1.1} \times 10^{-4}$. The normalization is the volume emission measure represented by $10^{-14} n_{\rm e} n_{\rm H} V / 4\pi d^2$, where $n_{\rm e}$, $n_{\rm H}$, V, and d are the electron density, the hydrogen density, the plasma volume, and the distance from the solar system, respectively. The observed 1–8 keV flux is estimated to be 8.4×10^{-14} erg s^{-1} cm^{-2}.

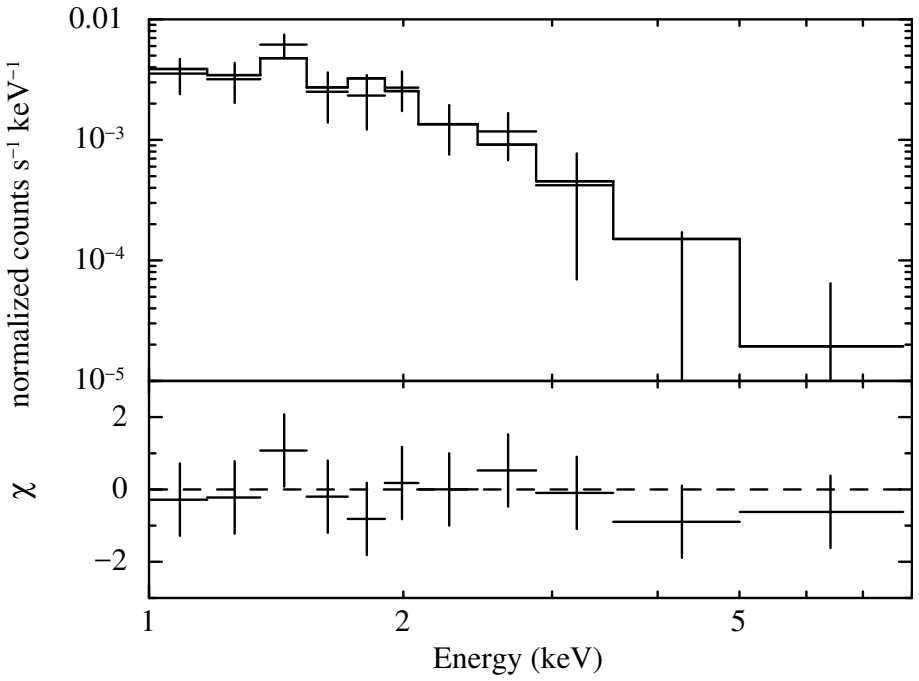

Figure 5.12: Top panel: Background subtracted spectrum of the soft source in the 1–8 keV band fitted with the absorbed thin-thermal plasma model. The solid line shows the best-fit model. Bottom panel: Residuals between the data and the best-fit model.

5.6 G330.2+1.0

X-ray images

Figures 5.13 show the NXB subtracted and exposure corrected XIS images of G330.2+1.0 in the 0.5–3 keV (a) and 5–8 keV (b) bands. Both of the images are binned with 8×8 pixels and then smoothed with a Gaussian function of $\sigma = 3$ bins. In the 0.5–3 keV band, shell structure and some point-like sources are seen. The point-like source in the shell, marked as "sourceA" in figure 5.13, corresponds to the CCO candidate of G330.2+1.0 (CXOU J160103.1−513353; Park et al., 2006, 2009). The brightest source locates in the south of the SNR, marked as "sourceB"

in figure 5.13(a), is the cataclysmic variable 3XMM J160050.4−514245. Unlike the other SNRs in this thesis, the shell structure of the SNR can clearly be seen even in the 5–8 keV band. This is consistent with the previously known fact that the X-ray radiation of G330.2+1.0 is dominated by the non-thermal emission.

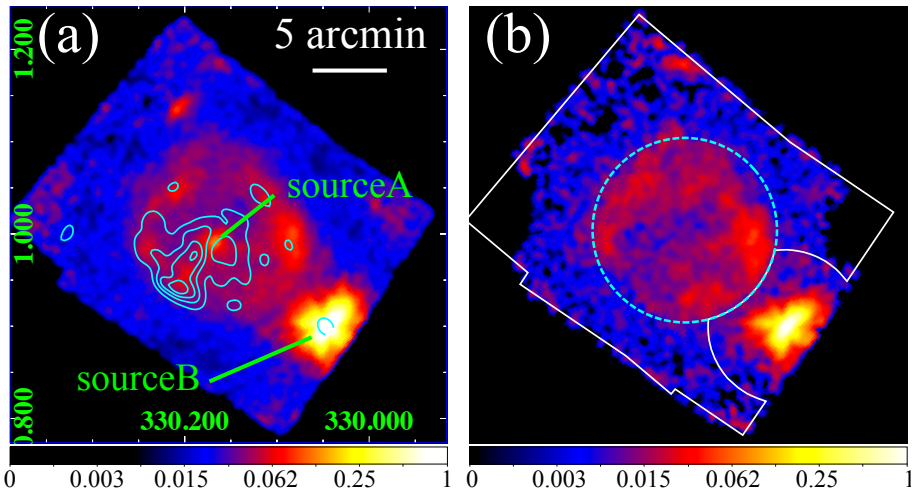

Figure 5.13: XIS images of G330.2+1.0 in the 0.5–3 keV band (a) and 5–8 keV band (b). The images are binned with 8×8 pixels and then smoothed with a Gaussian function of $\sigma = 3$ bins. The cyan contours show the 843 MHz radio continuum intensity (Whiteoak & Green, 1996). The data of XIS0, 1 and 3 are used for the 0.5–3 keV band image. The 5–8 keV band image is created using the data of XIS0 and 3. Cyan contours in image (a) show the intensity of 843 MHz radio continuum emission (Whiteoak & Green, 1996).

X-ray spectra

Due to the strong non-thermal emission, it was difficult to investigate the distribution of the 6.4 keV line emission using the 6.3–6.5 keV image. Thus the source region was defined as a circle surrounding the X-ray shell of the SNR at first. The radius of the source region is $6'$. The other part of the field of view was defined as reference region. A circle with a radius of $5'$ centroids on the sourceB was removed from the reference region to remove the contamination from the sourceB. The definition of the regions is seen in figure 5.13(b).

The XIS0+3 spectra were extracted from the source and the reference regions. The NXB was estimated using the data within ±300 days of the observation and then subtracted from each spectrum. Each spectrum was fitted with the model consisting of a power-law plus four Gaussian functions described in section 5.1. Figures 5.14 show the NXB subtracted spectra of the source and the reference regions, fitted with the power-law plus four Gaussian functions models. Both of the model fittings are statistically acceptable with $\chi^2_{\rm red} = 1.07$ (51 d.o.f.) for

the source region and $\chi^2_{\rm red} = 1.28$ (42 d.o.f.) for the reference region. The best-fit parameters are summarized in table 5.5. There is a sign that the intensity of the Fe I Kα line in the source region is higher compared to that in the reference region. The significance level of the excess in the source region is 2.0 σ. The line intensities of the Fe XXV and Fe XXVI Kα lines are consistent between the source and the reference region.

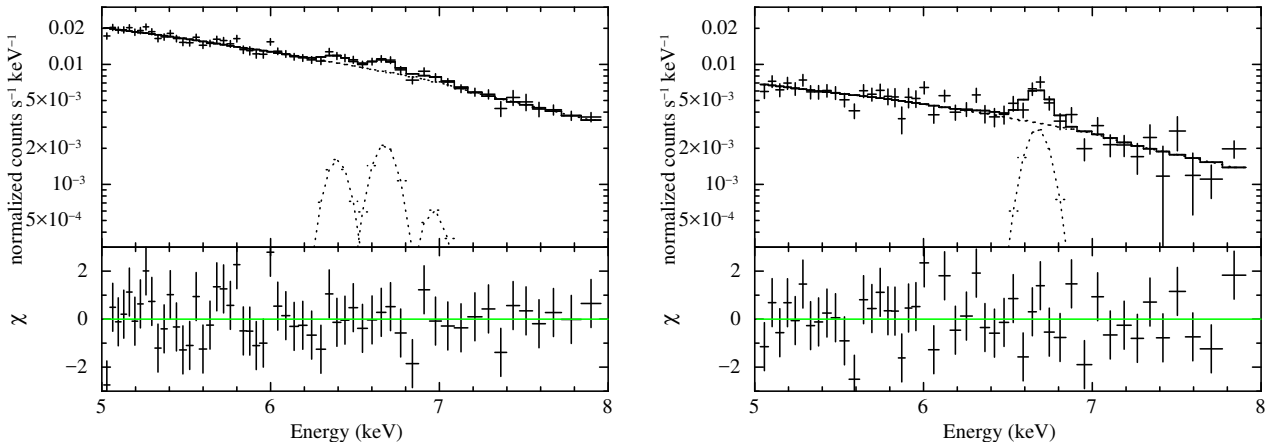

Figure 5.14: Spectra of the source region (left panel) and the reference region (*right panel*), fitted with the model consisting of a power-law and four Gaussian functions. The vertical axes are normalized with the areas of the regions. The solid lines in the top panels show the best-fit models, while the dotted line shows each component of the model.

Table 5.5: Best-fit parameters for the source and reference regions of G330.2+1.0

Parameter	Best-fit value	
	Source region	Reference region
Power-law photon index	2.5 ± 0.2	1.9 ± 0.4
Power-law intensity[1]	160 ± 3	57 ± 3
Fe I Kα Intensity[2]	1.5 ± 0.8	< 0.9
Fe XXV Kα Intensity[2]	2.4 ± 0.8	3.2 ± 0.8
Fe XXVI Kα Intensity[2]	< 1.5	< 0.5

[1] Observed intensity in the 5.0–8.0 keV band in the unit of 10^{-8} photons cm^{-2} s^{-1} arcmin^{-2}.
[2] Observed intensity in the unit of 10^{-8} photons cm^{-2} s^{-1} arcmin^{-2}.

Next, the spatial distribution of the line intensity is investigated. We divided the source region into 12 regions. The source region is divided by every 60 degrees from the north direction in the equatorial coordinates at first. Then the regions are divided into the inner part ($r < 4'$) and the outer part ($4' < r < 6'$). The divided regions, tagged as numbers from 1 to 12, are described in figure 5.15. The spectrum was extracted from each region and then the NXB was subtracted. Note that the NXB spectra were not shifted and re-normalized, since the

spectrum extracted from each region do not have enough statistics to correct the NXB. Then each spectrum was fitted with the model consisting of a power-law and four Gaussians model.

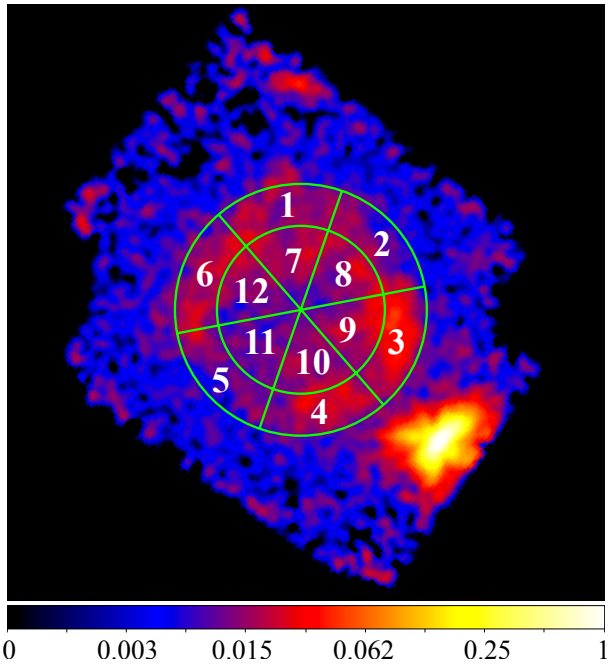

Figure 5.15: Definition of 12 regions to investigate the line intensity distribution in the source region, overlapped on the 5–8 keV band image.

Table 5.6 shows the summary of the line intensities of Fe I, Fe XXV and Fe XXVI Kα in each region obtained by the spectral fitting. Although most of the regions show only the upper limits of the Fe I Kα line intensity, the region number 5 shows stronger Fe I Kα line. The intensities of the Fe XXV and XXVI Kα lines, on the other hand, are consistent between all 12 regions.

Then we compared the spectrum between the region number 5 and the source region except for the region number 5. Figures 5.16 show the spectra extracted from the region number 5 (left panel) and the other part of the source region (right panel). Each spectrum is fitted with the power-law plus four Gaussian functions model. The vertical axes are normalized with the ratio of the areas, considering the vignetting effect. The best-fit parameters are summarized in table 5.7. The significance level of the enhancement of the Fe I Kα line in the region number 5 is 2.7σ compared to the reference region. The other part of the source region shows a sign that the Fe I Kα line intensity is also higher than that of the reference region with a significance level of 1.5σ. The intensity of the power-law component of the region number 5 is lower than that of the other part of the source region.

Table 5.6: Line intensities of Fe I, Fe XXV and Fe XXVI Kα in the region 1–12 of G330.2+1.0

Region number	Line intensity[1]		
	Fe I Kα	Fe XXV Kα	Fe XXVI Kα
1	< 5.5	< 6.1	< 6.7
2	< 1.5	3.2 ± 2.8	< 1.9
3	< 3.5	$3.7^{+3.4}_{-3.3}$	< 2.2
4	< 4.6	4.5 ± 3.2	< 4.1
5	4.9 ± 2.8	4.2 ± 2.8	< 3.1
6	< 3.7	< 5.1	< 2.4
7	< 3.6	< 4.6	< 1.6
8	< 4.5	< 3.2	< 4.1
9	< 5.2	4.1 ± 3.2	< 5.7
10	< 3.2	< 3.6	< 6.2
11	< 4.0	< 4.8	< 2.2
12	< 4.0	< 5.1	< 2.9

[1] Observed intensity in the unit of 10^{-8} photons cm^{-2} s^{-1} arcmin^{-2}.

Table 5.7: Best-fit parameters for the region number 5 and the other par of the source region

Parameter	Best-fit value	
	Region number 5	Source region except for the region number 5
Power-law photon index	$3.4^{+1.0}_{-0.8}$	2.4 ± 0.2
Power-law intensity[1]	102^{+10}_{-11}	172 ± 4
Fe I Kα Intensity[2]	4.9 ± 2.8	1.2 ± 0.5
Fe XXV Kα Intensity[2]	4.2 ± 2.8	2.3 ± 0.9
Fe XXVI Kα Intensity[2]	< 3.1	< 1.4

[1] Observed intensity in the 5.0–8.0 keV band in the unit of of 10^{-8} photons cm^{-2} s^{-1} arcmin^{-2}.
[2] Observed intensity in the unit of 10^{-8} photons cm^{-2} s^{-1} arcmin^{-2}.

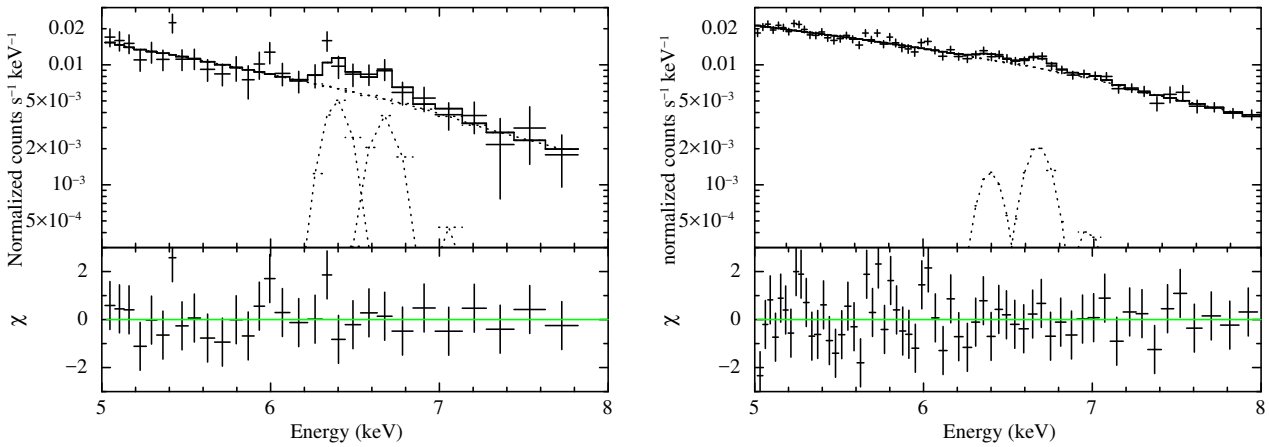

Figure 5.16: Comparison of the spectra of the region number 5 (left panel) and the other part of the source region (right panel). The upper panels show the spectra fitted with the power-law plus four Gaussian functions model. The vertical axes are normalized with the ratio of the areas, considering the vignetting effect. The bottom panels show the residuals between the data and the best-fit models.

5.7 G346.6−0.2

X-ray images

Figures 5.17 show the NXB subtracted and exposure corrected XIS images of G346.6−0.2 in the 0.5–3 keV (a), 5–8 keV (b) and 6.3–6.5 keV (c) bands. The 0.5–3 keV and 5–8 keV bands images are binned with 8×8 pixels and then smoothed with a Gaussian function of $\sigma = 3$ bins. The 6.3–6.5 keV band image is binned with 32×32 pixels and then smoothed with a Gaussian function of $\sigma = 8$ bins.

In the 0.5–3 keV band, diffuse X-ray emission filling the radio shell is seen. The spatial distribution of the diffuse emission is consistent with the previously known thermal emission. Above 5 keV, on the other hand, there is no significant diffuse X-ray emission. There are two point-like sources surrounded by green circles in figure 5.17(b). In the 6.3–6.5 keV band, an excess with a size of $\sim 9' \times 4'$.

X-ray spectra

In order to investigate the diffuse source in the 6.3–6.5 keV band, both of two point-like sources seen in the 5–8 keV band were removed with circular regions with the radius of $2'$ from the following analysis. The excess region was defined as an area surrounded by the dashed ellipse except for the green circles shown in figure 5.17(c) The whole field except for the excess region and the circular regions was defined as the reference region.

The XIS0+3 spectra were extracted from the excess and the reference regions. The NXB

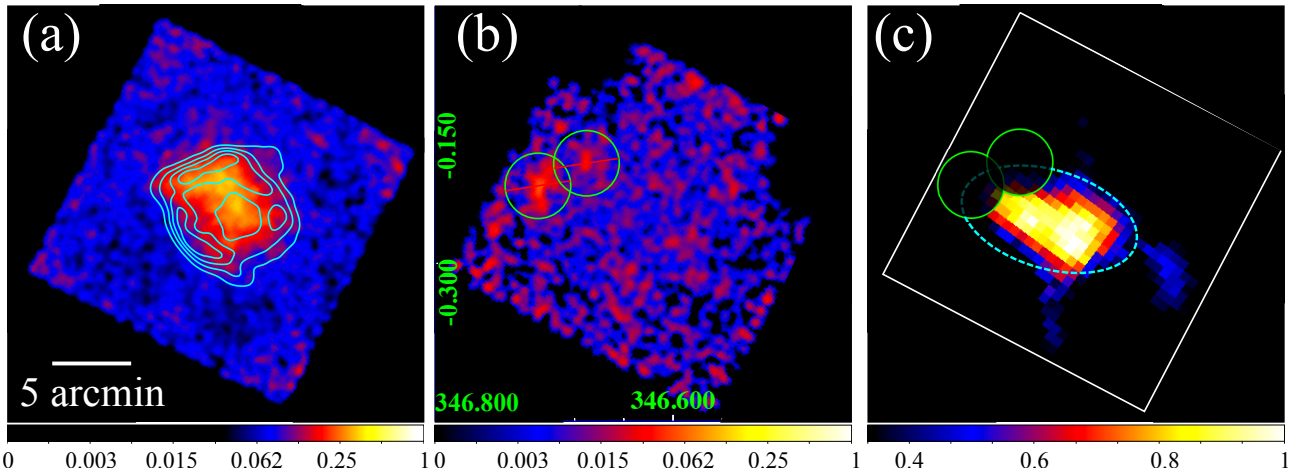

Figure 5.17: (a) : XIS0+1+3 image of G304.6+0.1in the 0.5–5 keV. The image is binned with 8×8 pixels and then smoothed with a Gaussian function of $\sigma = 3$ bins. Cyan contours in figure (a) show the 843 MHz radio intensity (Whiteoak & Green, 1996). (b) : XIS0+3 image in the 5–8 keV. The binning and the smoothing is same as that of (a). The green circle shows the position of the point-lie source. (c) : XIS0+3 image in the 6.3–6.5 keV band (c). The image is binned with 32×32 pixels and then smoothed with a Gaussian function of $\sigma = 8$ bins. The regions surrounded wth cyan dashed lines is the "excess" region, and the remaining part of the field of view is the "reference" region. The color scales are normalized so that the bright pixel is 1.

was estimated using the data within ±300 days of the observation and then subtracted from each spectrum. Each spectrum was fitted with the model consisting of a power-law and four Gaussian functions described in section 5.1. Figures 5.18 show the NXB subtracted spectra of the excess region and the reference region with the best-fit models. Both of the model fittings are acceptable with $\chi^2_{\rm red} = 0.73$ (22 d.o.f.) for the excess region and $\chi^2_{\rm red} = 1.21$ (29 d.o.f.). The best-fit parameters are summarized in table 5.8. The intensities of the Fe XXV and Fe XXVI Kα lines are consistent between the excess and reference regions. The intensity of the Fe I Kα line of the excess region, on the other hand, is significantly higher than that of the reference region. The significance level of the enhancement is 3.2σ. There is a sign that the photon index of the power-law component is larger in the excess region with a significance level of 2.2σ. The intensities of the power-law components in the energy band of 5–8 keV are consistent with each other.

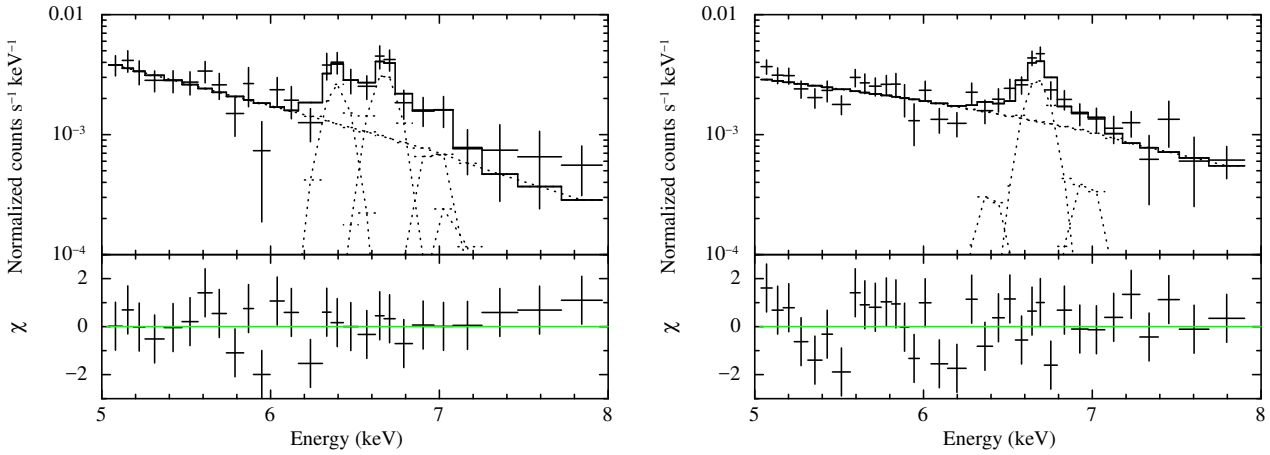

Figure 5.18: *Top panels* : 5–8 keV spectra of G346.6−0.2 extracted from the excess (left) and reference (right) regions, fitted with a power-law plus four Gaussian functions model. The vertical axes are normalized with the areas of the regions.The solid lines in the top panels show the best-fit models, while the dotted lines show the components of the model. *Bottom panels* : Residuals between the data and the best-fit models divided by the error of each bin.

Table 5.8: Best-fit parameters for the excess and reference regions of G346.6−0.2

Parameter	Best-fit value	
	Excess region	Reference region
Power-law photon index	$4.6^{+1.8}_{-1.4}$	$2.3^{+0.9}_{-0.8}$
Power-law intensity[1]	48^{+8}_{-7}	51 ± 5
Fe I Kα Intensity[2]	5.6 ± 2.3	< 1.8
Fe XXV Kα Intensity[2]	7.7 ± 2.4	6.8 ± 1.5
Fe XXVI Kα Intensity[2]	2.3 ± 2.0	< 2.4

[1] Observed intensity in the 5.0–8.0 keV band in the unit of photons cm^{-2} s^{-1} arcmin^{-2}.
[2] Observed intensity in the unit of 10^{-8} photons cm^{-2} s^{-1} arcmin^{-2}.

5.8 G348.5+0.1

X-ray images

Figures 5.19 show the NXB subtracted and exposure corrected XIS images of G348.5+0.1 in the 0.5–3 keV (a), 5–8 keV (b) and 6.3–6.5 keV (c) bands. The 0.5–3 keV and 5–8 keV bands images are binned with 8×8 pixels and then smoothed with a Gaussian function of $\sigma = 3$ bins. The 6.3–6.5 keV band image is binned with 32×32 pixels and then smoothed with a Gaussian function of $\sigma = 6$ bins.

In the 0.5–3 keV band image, diffuse emission is seen near the center of the field of view. The soft X-rays correspond to the previously known thermal emission. In the 5–8 keV band, two sources are seen as tagged as A and B in figure 5.19(b). The source A is coincident with

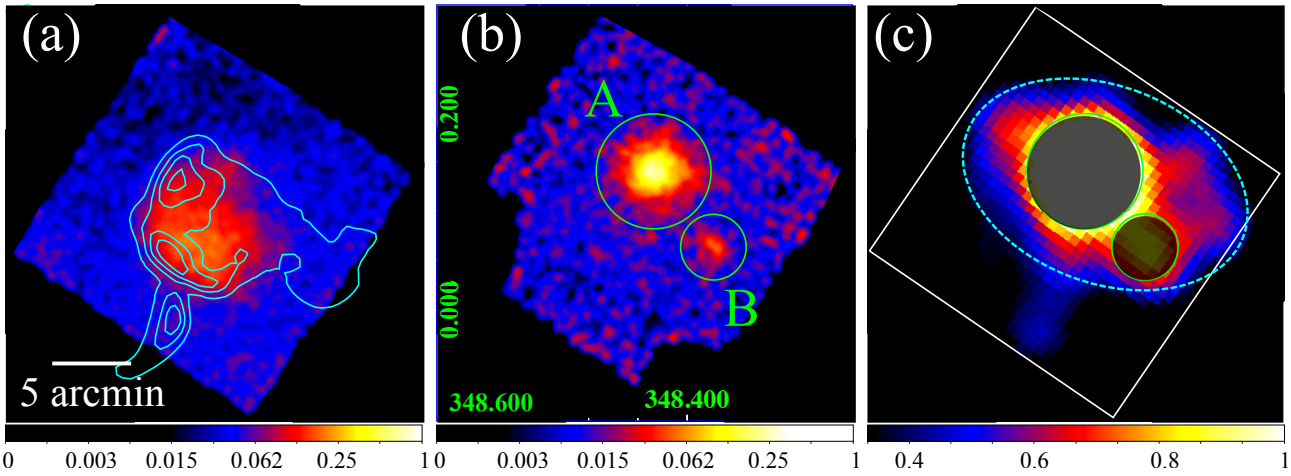

Figure 5.19: (a) : XIS0+1+3 image of G348.5+0.1 in the 0.5–3 keV band. The image is binned with 8×8 pixels and then smoothed with a Gaussian function of $\sigma = 3$ bins. The cyan contours show the 843 MHz radio continuum intensity (Whiteoak & Green, 1996). (b) : XIS0+3 image in the 5–8 keV band. The size of the binning and smoothing are the same as that of (a). (c) : XIS0+3 image in the 6.3–6.5 keV band. The image is binned with 32×32 pixels and then smoothed with a Gaussian function of $\sigma = 6$ bins. The areas surrounded with the dashed curves are the "excess" region, while the whole field except for the excess region and the sources A and B is the "reference" region.

the non-thermal source named as CXOU J171419.8−383023 (Aharonian et al., 2008c). The source B in figure 5.19(b) is coincident with the point source 3XMM J171428.5−383600. In the 5–8 keV band image, on the other hand, no clear diffuse emission is seen. In the 6.3–6.5 keV band, there is structure near the sources A and B.

X-ray spectra

The excess region was defined as an ellipse illustrated with the dashed line in figure 5.19(c). The sources A and B can be contaminants to estimate the iron Kα line intensities. The regions around the sources A and B were removed with circles with radii of $3\farcm5$ and $2\farcm0$, respectively. The whole field except for the excess region and the circular regions around the sources A and B was defined as the reference region.

The XIS0+3 spectra were extracted from the excess and the reference regions. The NXB was estimated using the data within ±300 days of the observation and then subtracted from each spectrum. Each spectrum was fitted with the model consisting of a power-law and four Gaussian functions described in section 5.1. Figures 5.20 show the NXB subtracted spectra of the excess and the reference regions with the best-fit models. Both of the model fittings are statistically acceptable with $\chi^2_{\rm red} = 1.09$ (38 d.o.f.) for the excess region and $\chi^2/_{\rm red} = 1.10$ (25

d.o.f.) for the reference region. The best-fit parameters are summarized in table 5.9.

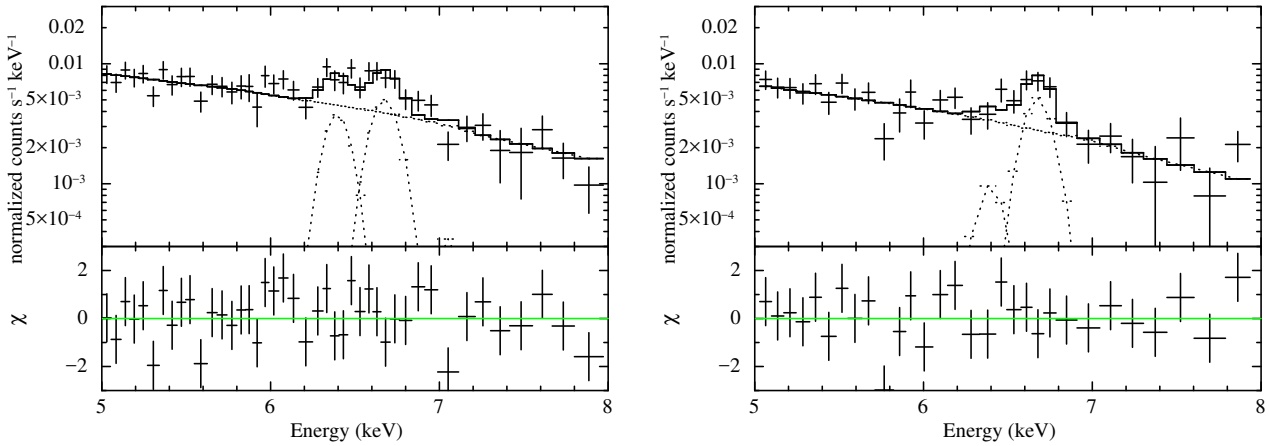

Figure 5.20: Top panels : NXB subtracted spectra of G348.5+0.1 extracted from the excess (left) and reference (right) regions, fitted with the power-law plus four Gaussian functions models in the 5–8 keV band. The vertical axes are normalized with the areas of the regions. The best-fit models are plotted with the solid lines, while each component is plotted with the dotted line. Bottom panels: Residuals between the data and the best-fit models.

Table 5.9: Best-fit parameters for the excess and reference regions of G348.5+0.1.

Parameter	Best-fit value	
	excess region	background region
Power-law photon index	$2.1^{+0.6}_{-0.5}$	$2.3^{+0.9}_{-0.8}$
Power-law intensity[1]	86^{+6}_{-7}	64 ± 7
Fe I Kα Intensity[2]	4.5 ± 1.8	< 3.0
Fe XXV Kα Intensity[2]	6.9 ± 1.9	7.3 ± 2.2
Fe XXVI Kα Intensity[2]	< 1.6	< 1.6

[1] Observed intensity in the 5.0–8.0 keV band in the unit photons cm^{-2} s^{-1} arcmin^{-2}.
[2] Observed intensity in the unit of 10^{-8} photons cm^{-2} s^{-1} arcmin^{-2}.

The spectrum extracted from the excess region shows a sign of the enhancement in the Fe I Kα line. The significance level of the enhancement is 2.2σ. The intensities of the Fe XXV Kα and the Fe XXVI Kα lines are consistent between the excess region and the reference region. The photon index of the power-law component is also consistent between the regions. The intensity of the power-law component, on the other hand, is significantly higher in the excess region with a confidence level of 3.9σ.

The X-rays from the source A (see figure 5.20) might affect the estimation of the line intensities of the excess region. To check the degree of the contamination, we extracted a spectrum of the source A. Figure 5.21 shows the XIS0+3 spectrum of the source A. The spectrum of the reference region was subtracted as the background. No clear signs of the lines are seen.

Then the spectrum was fitted with a model which is the same with that applied for the spectral fittings of the excess and the reference regions. The 6.4 keV line flux of the source A was obtained to be $< 2.2 \times 10^{-6}$ photons cm^{-2} s^{-1}. Based on the point-spread function of the Suzaku XRT simulated with the xissim toolkit, it is estimated that about 5 % of the photons from the source A leak into the excess region. Since the area of the excess region is 120 arcmin^{-2}, the contamination for 6.4 keV line intensity from the source A is estimated to be less than $2.2 \times 10^{-6} \times 5\ \%/120 = 9.1 \times 10^{-10}$ photons cm^{-2} s^{-1} arcmin^{-2}. This value is only 2 % of the 6.4 keV line intensity in the excess region and thus the contamination is negligible. It is also confirmed that the source B does not exhibit the significant 6.4 keV line. Since the source B is much fainter than the source A, we concluded that the contamination from the source B is also negligible.

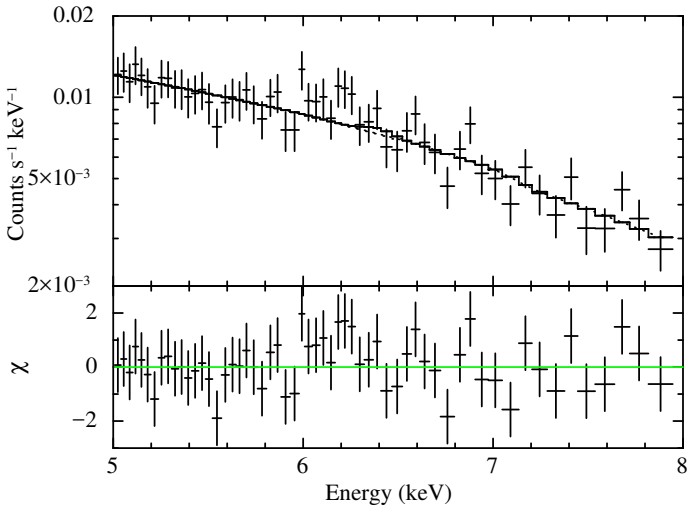

Figure 5.21: Top panel : Background subtracted spectrum of the source A, fitted with the power-law plus four Gaussian functions models in the 5–8 keV band. The best-fit models are plotted with the solid lines. Note that each Gaussian functions are not seen in the range of the figure. Bottom panel: Residuals between the data and the best-fit models.

5.9 G348.7+0.3

X-ray images

Figures 5.22 show the NXB subtracted and exposure corrected XIS images of G348.7+0.3 in the 0.5–3 keV (a), 5–8 keV (b) and 6.3–6.5 keV (c) bands. The 0.5–3 keV and 5–8 keV bands images are binned with 8×8 pixels and then smoothed with a Gaussian function of $\sigma = 3$ bins. The 6.3–6.5 keV band image is binned with 32×32 pixels and then smoothed with a Gaussian function of $\sigma = 6$ bins.

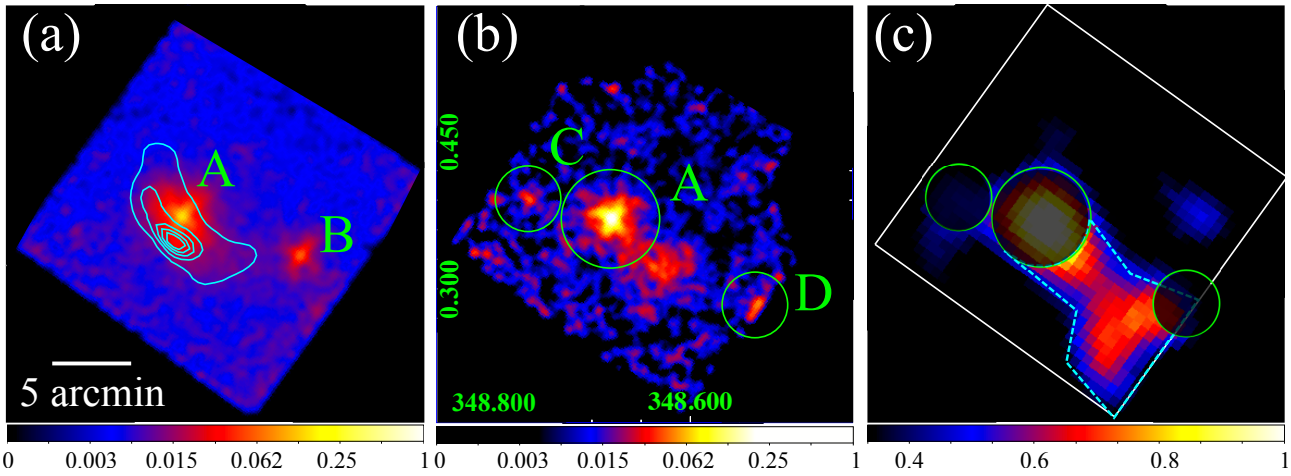

Figure 5.22: (a) : XIS0+1+3 image of G348.7+0.3 in the 0.5–3 keV band. The image is binned with 8×8 pixels and then smoothed with a Gaussian function of $\sigma = 3$ bins. The cyan contours show the 843 MHz radio continuum intensity (Whiteoak & Green, 1996). (b) : XIS0+3 image in the 5–8 keV band. The size of the binning and smoothing are the same as that of (a). (c) : XIS0+3 image in the 6.3–6.5 keV band. The image is binned with 32×32 pixels and then smoothed with a Gaussian function of $\sigma = 6$ bins. The regions surrounded with dashed lines except for the circular regions around the sources A, C and D is the "excess" region, while the whole field except for the excess region and the sources A, C and D is the "reference" region.

In the 0.5–3 keV band image, two point-like sources are seen (tagged as A and B in figure 5.22(a)). The source A is coincident with the AXP candidate CXOU J171405.7−381031 (Nakamura et al., 2009). The source B is coincident with 1RXS J171354.4−381740. In addition to the point-like sources, it is known that there is a faint extended source near the source A (Nakamura et al., 2009). Due to contamination by the PSF tail of the source A, the extended source cannot be seen clearly in figure 5.22(a).

In the 5–8 keV band, diffuse emission is seen in the south of the source A. This structure is coincident with the previously known diffuse emission consisting of the thermal and the non-thermal components. The point sources tagged as "C" and "D" in figure 5.22(b) is coincident with the point sources 3XMM J171416.4−380559 and 3XMM J171400.7−382054, respectively.

In the 6.3–6.5 keV band, extended emission spreads to the southern direction from the source A. Some part of the 6.3–6.5 keV enhancement is coincident with the diffuse structure seen in figure 5.22(b).

X-ray spectra

In the following analysis, areas around the sources A, C and D were removed by circles with radii of 2′.7 (source A) and 2′.0 (sources C and D). The excess region was defined as an area

surrounded by the dashed lines in figure 5.22 except for the circle centroids on the sources A, C and D. The whole field except for the excess region and three sources was defined as the reference region.

The XIS0+3 spectra were extracted from the excess and the reference regions. The NXB was estimated using the data within ±300 days of the observation and then subtracted from each spectrum. Each spectrum was fitted with the model consisting of a power-law and four Gaussian functions described in section 5.1. Figures 5.23 show the NXB subtracted spectra of the excess and the reference regions with the best-fit models. Both of the model fittings are statistically acceptable with $\chi^2_{\rm red} = 0.98$ (32 d.o.f.) for the excess region and $\chi^2_{\rm red} = 1.34$ (27 d.o.f.) for the reference region. The best-fit parameters are summarized in table 5.10.

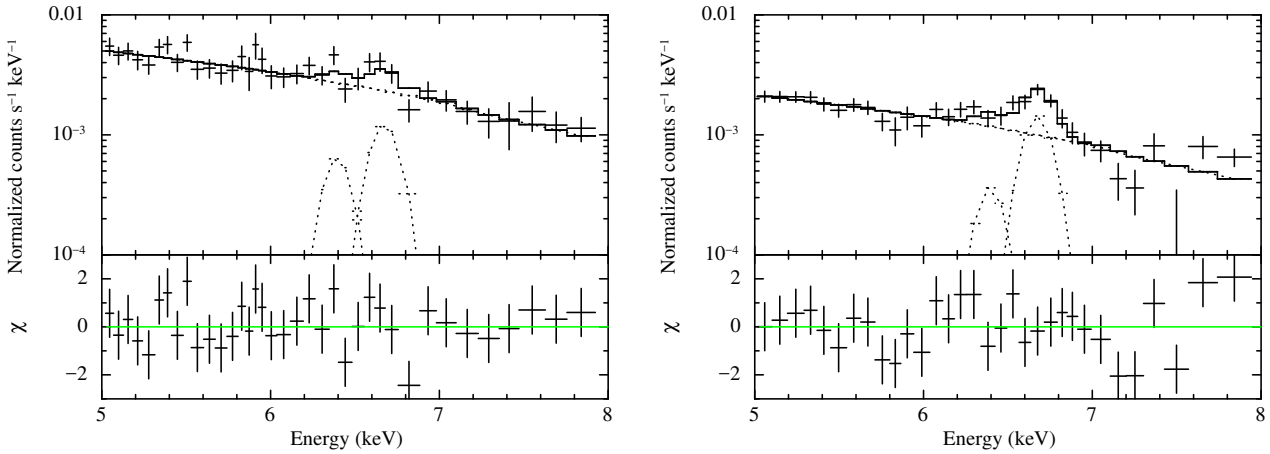

Figure 5.23: Top panels : NXB subtracted spectra of G348.7+0.3 extracted from the excess (left) and reference (right) regions, fitted with the power-law plus four Gaussian functions models in the 5–8 keV band. The vertical axes are normalized with the areas of the regions. The best-fit models are plotted with the solid lines, while each component is plotted with the dotted line. Bottom panels: Residuals between the data and the best-fit models.

Table 5.10: Best-fit parameters for the excess and reference regions of G348.7+0.3.

Parameter	Best-fit value	
	Excess region	Reference region
Power-law photon index	$2.1^{+0.6}_{-0.5}$	2.0 ± 0.5
Power-law intensity[1]	130^{+9}_{-11}	58 ± 4
Fe I Kα Intensity[2]	< 4.8	1.2 ± 1.0
Fe XXV Kα Intensity[2]	4.6 ± 2.9	5.5 ± 1.1
Fe XXVI Kα Intensity[2]	< 2.7	< 0.9

[1] Observed intensity in the 5.0–8.0 keV band in the unit photons cm^{-2} s^{-1} arcmin^{-2}.
[2] Observed intensity in the unit of 10^{-8} photons cm^{-2} s^{-1} arcmin^{-2}.

Only an upper limit is obtained for the intensity of the Fe I Kα line in the excess region,

although its best-fit value is higher than that in the reference region (see figure 5.23). The intensity of the power-law component of the excess region is significantly higher than that of the reference region. This result is reasonable because the excess region contains the diffuse non-thermal emission seen in the 5–8 keV band. The other parameters are consistent between the excess and reference regions.

5.10 G355.6−0.0

X-ray images

Figures 5.24 show the NXB subtracted and exposure corrected XIS images of G355.6−0.0 in the 0.5–3 keV (a), 5–8 keV (b) and 6.3–6.5 keV (c) bands. The 0.5–3 keV and 5–8 keV bands images are binned with 8×8 pixels and then smoothed with a Gaussian function of $\sigma = 3$ bins. The 6.3–6.5 keV band image is binned with 32×32 pixels and then smoothed with a Gaussian function of $\sigma = 6$ bins.

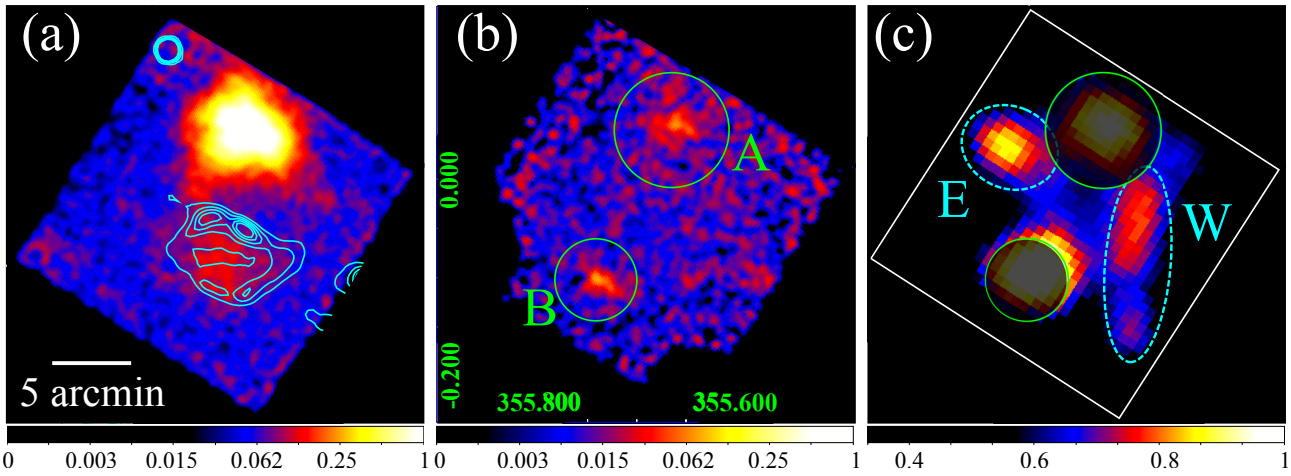

Figure 5.24: (a) : XIS0+1+3 image of G355.6−0.0 in the 0.5–3 keV band. The image is binned with 8×8 pixels and then smoothed with a Gaussian function of $\sigma = 3$ bins. Cyan contours show the 843 MHz radio continuum intensity (Whiteoak & Green, 1996). (b) : XIS0+3 image in the 5–8 keV band. The size of the binning and smoothing are the same as that of (a). (c) : XIS0+3 image in the 6.3–6.5 keV band. The image is binned with 32×32 pixels and then smoothed with a Gaussian function of $\sigma = 6$ bins.

In the 0.5–3 keV band image, a diffuse structure is seen in the radio shell. This emission is coincident with the previously known thermal plasma of G355.6−0.0 (Minami et al., 2013). A bright X-ray source at the west of G355.6−0.0 is the young open cluster NGC 6383 (Rauw et al., 2003). In the 5–8 keV band, two X-ray sources are seen. The one tagged as "A" in figure 5.24(b) is NGC 6383, while the other one tagged as "B" is a CV candidate named as

Suzaku J173530−3236 (Minami et al., 2013). On the other hand, there is no distinct diffuse structure.

In the 6.3–6.5 keV band, sources A and B are clearly seen. In addition to these sources, two enhancements tagged as E and W are seen. However, the enhancement E would not be involved with the SNR, since the enhancement is away from G355.6−0.0 over the diameter of the SNR.

X-ray spectra

Circular regions centroids on the source A with a radius of 3′.5 and centroids on the source B with a radius of 3′.5 were excluded from the following spectral analysis.

First, we investigated the spectrum extracted from a combined region of the enhancements E+W excluding the circular regions centroid on the sources A and B. The reference region was defined as whole field except for the enhancements E and W, and the sources A and B in figure 5.24. The XIS0+3 spectra were extracted from the E+W and the reference regions. The NXB was estimated using the data within ±300 days of the observation and then subtracted from each spectrum. Each spectrum was fitted with the model consisting of a power-law and four Gaussian functions described in section 5.1.

Figures 5.25 show the NXB subtracted spectra extracted from the E+W region and the reference region with the best-fit models. Both of the fittings are acceptable with $\chi^2_{\rm red} = 1.38$ (23 d.o.f.) for the E+W region and $\chi^2_{\rm red} = 0.83$ (49 d.o.f.) for the reference region. The best-fit parameters are summarized in table 5.11. The intensity of the 6.4 keV line emission in the E+W region is higher than that in the reference region with a significance of 2.9σ. All the other parameters are consistent between the E+W and the reference regions.

Table 5.11: Best-fit parameters for the E+W and reference regions of G355.6−0.0.

Parameter	Best-fit value	
	Excess region	Reference region
Power-law photon index	$2.7^{+0.9}_{-0.8}$	2.2 ± 0.5
Power-law intensity[1]	94 ± 10	97 ± 6
Fe I Kα Intensity[2]	7.2 ± 2.8	< 3.0
Fe XXV Kα Intensity[2]	12.5 ± 3.2	12.3 ± 2.1
Fe XXVI Kα Intensity[2]	< 4.4	2.5 ± 1.7

[1] Observed intensity in the 5.0–8.0 keV band in the unit photons cm^{-2} s^{-1} arcmin^{-2}.
[2] Observed intensity in the unit of 10^{-8} photons cm^{-2} s^{-1} arcmin^{-2}.

Next the spectrum of the region W was tested in the same way. Figure 5.26 shows the NXB subtracted spectrum extracted from the region W fitted with the power-law plus four Gaussian

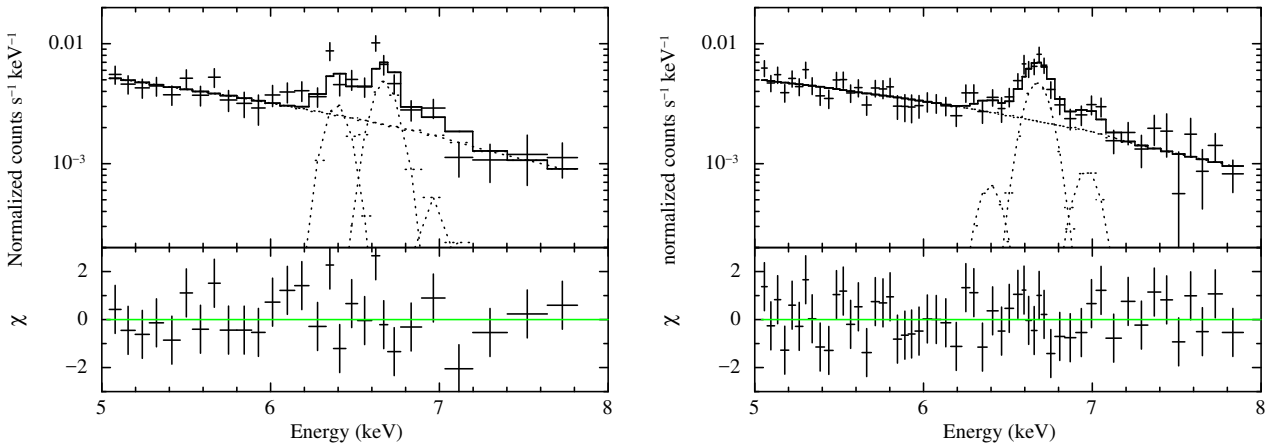

Figure 5.25: Top panels : NXB subtracted spectra of G355.6−0.0 extracted from the E+W region (left) and the reference (right) region, fitted with the power-law plus four Gaussian functions models in the 5–8 keV band. The vertical axes are normalized with the areas of the regions. The best-fit models are plotted with the solid lines, while each component is plotted with the dotted line. Bottom panels: Residuals between the data and the best-fit models.

functions model. The fittings is acceptable with $\chi^2_{\rm red} = 1.00$ (36 d.o.f.). The intensities of the Fe Kα lines are $(5.9 \pm 3.4) \times 10^{-8}$ (Fe I), $(14.7 \pm 4.1) \times 10^{-8}$ (Fe XXV) and $< 5.3 \times 10^{-8}$ photons cm^{-2} s^{-1} arcmin^{-2} (Fe XXVI). The enhancement of the Fe I Kα line is not significant with 1.9σ in the case that only the western part of the enhancement is involved with G355.6−0.0.

5.11 G359.0−0.9

X-ray images

Figures 5.27 show the NXB subtracted and exposure corrected XIS images of G359.0−0.9 in the 0.5–3 keV (a), 5–8 keV (b) and 6.3–6.5 keV (c) bands. The images of 0.5–3 keV and 5–8 keV bands are binned with 8×8 pixels and then smoothed with a Gaussian function of $\sigma = 3$ bins. The 6.3–6.5 keV image is binned with 32×32 pixels and then smoothed with a Gaussian function of $\sigma = 6$ bins

In the 0.5–3 keV band image, a diffuse structure is seen near the radio shell. In addition, bright emission is seen at the northeast corner of the image. This brightness peak is a composition of two X-ray sources; SLX 1744−299 and SLX 1744−300. SLX 1744−299 is a pulser, while SLX 1744−300 is a low-mass X-ray binary. These sources can also be seen in the 5–8 keV band image (see figure 5.27(b)). In addition, diffuse X-ray emission is seen in the 5–8 keV band image as marked with a white dashed rectangle. In the 6.3–6.5 keV band image, enhancement is seen near the radio shell of G359.0−0.9.

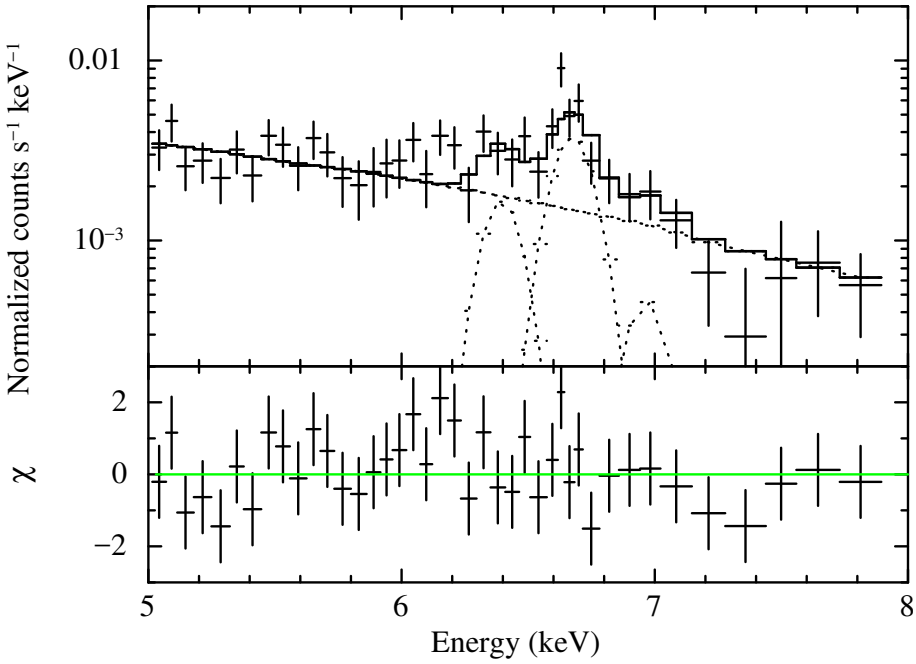

Figure 5.26: Top panel : NXB subtracted spectrum of G355.6−0.0 extracted from the region W fitted with the power-law plus four Gaussian functions model in the 5–8 keV band. The best-fit model is plotted with the solid line, while each component is plotted with the dotted line. Bottom panel: Residuals between the data and the best-fit model.

X-ray spectra

The excess region was defined as areas surrounded by dashed lines in figure 5.27(c). The point sources seen in the 5–8 keV band were removed with circles centroids on the sources with a radius of $2'$. Note that the excess region includes the diffuse emission seen in the 5–8 keV band, which indicate that the enhancement in figure 5.27(c) is possibly affected by the continuum emission. Thus a spectrum extracted from whole excess region will be investigated first, then a spectrum of the excess region except for the rectangle region, illustrated by white dashed line in figure 5.27(b), will be checked. A reference region is all of the field of view except for the excess region and the point-like source. First, spectra extracted from the whole excess region and the reference region are fitted with a power-law plus four Gaussians model. Both of the model fittings are statistically acceptable with $\chi^2_{\rm red} = 0.92$ (65 d.o.f.) for the excess region and $\chi^2_{\rm red} = 1.07$ (56 d.o.f.) for the reference region. The best-fit parameters are summarized in table 5.12.

Both of the intensities of the Fe I Kα and Fe XXV Kα in the excess region are slightly higher than that in the reference region with significance levels of 1.7σ and 2.6σ, respectively. The intensity of the continuum emission, on the other hand, is clearly higher in the excess region.

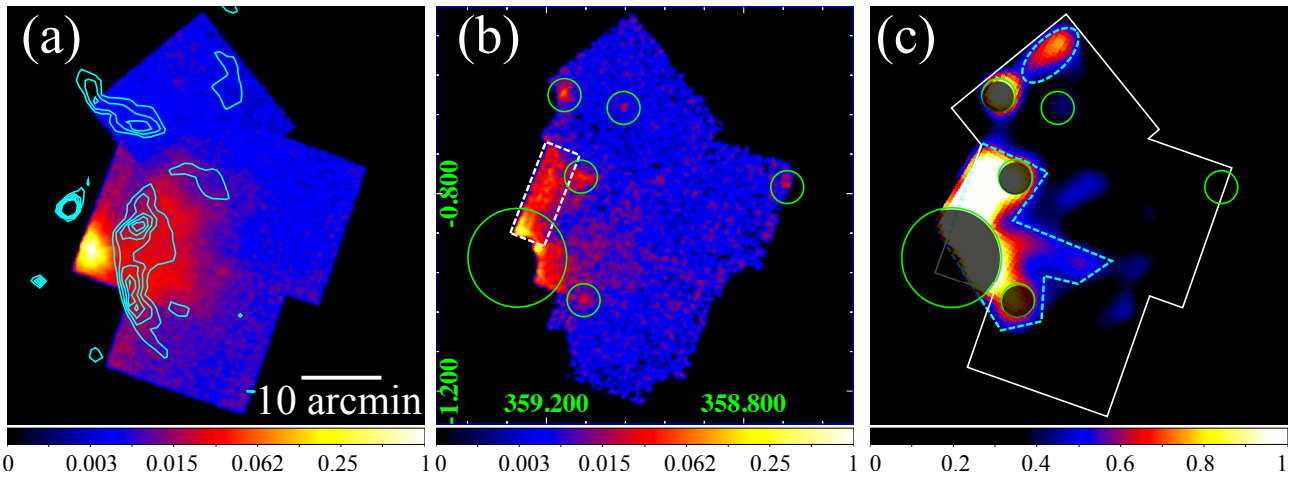

Figure 5.27: (a) : XIS0+1+3 image of G359.0−0.9 in the 0.5–5 keV. The image is binned with 8×8 pixels and then smoothed with a Gaussian function of $\sigma = 3$ bins. The cyan contours show the 843 MHz radio continuum intensity taken from the Skyview homepage. (b) : XIS0+3 image in the 5–8 keV. The binning and then smoothing is same as that of (a). Green circle shows the position of the point-lie source. (c) : XIS0+3 image in the 6.3–6.5 keV band (c). The image is binned with 32×32 pixels and then smoothed with a Gaussian function of $\sigma = 6$ bins. The regions surrounded with cyan dashed lines is the "excess" region, and the remaining part of the field of view is the "reference" region. The color scales are normalized so that the bright pixel is 1.

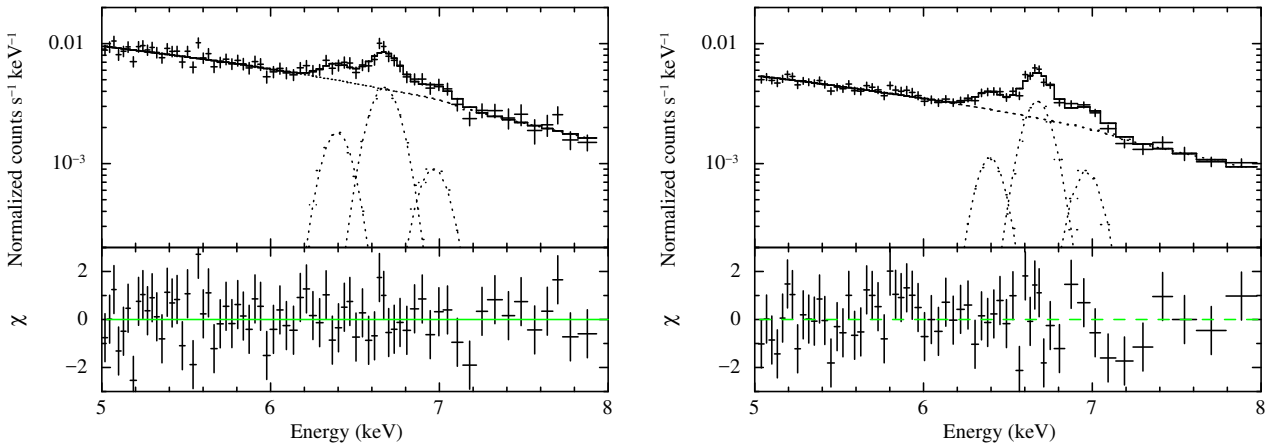

Figure 5.28: Top panels : NXB subtracted spectra of G359.0−0.9 extracted from the excess (left) and reference (right) regions, fitted with the power-law plus four Gaussian functions models in the 5–8 keV band. The vertical axes are normalized with the areas of the regions. The best-fit models are plotted with the solid lines, while each component is plotted with the dotted line. Bottom panels: Residuals between the data and the best-fit models.

Then a spectrum, which was extracted from the excess region except for the diffuse emission seen in the 5–8 keV band, was tested. Figure 5.29 shows the spectrum fitted with a power-law plus four Gaussians model. The fitting is acceptable with $\chi^2/\nu = 1.09$ ($\nu = 49$). The

Table 5.12: Best-fit parameters for the excess and reference regions of G359.0−0.9.

Parameter	Best-fit value		
	Excess region 1[1]	Excess region 2[2]	Reference region
Power-law photon index	2.4 ± 0.2	2.5 ± 0.3	2.4 ± 0.2
Power-law flux[3]	218 ± 7	188 ± 7	124 ± 2
Fe I Kα Intensity[4]	5.6 ± 1.9	5.2 ± 1.9	3.3 ± 0.7
Fe XXV Kα Intensity[4]	15.1 ± 2.2	15.5 ± 2.2	11.0 ± 0.9
Fe XXVI Kα Intensity[4]	3.5 ± 1.9	3.4 ± 1.9	3.3 ± 0.8

[1] Whole area of the excess region.
[2] Excess region except for the diffuse emission seen in the 5–8 keV band.
[3] Observed intensity in the 5.0–8.0 keV band in the unit photons cm^{-2} s^{-1} arcmin^{-2}.
[4] Observed intensity in the unit of 10^{-8} photons cm^{-2} s^{-1} arcmin^{-2}.

best-fit parameters are also summarized in table 5.12. Although the intensity of the power-law component decreases by the removing of the diffuse emission seen in the 5–8 keV band, it is still higher than that in the reference region. The intensities of three Gaussians, on the other hand, does not change significantly. Since the significance level of the enhancement of the Fe I Kα line is only 1.4σ, it is concluded that there is not a significant enhancement of 6.4 keV line at G359.0−0.9.

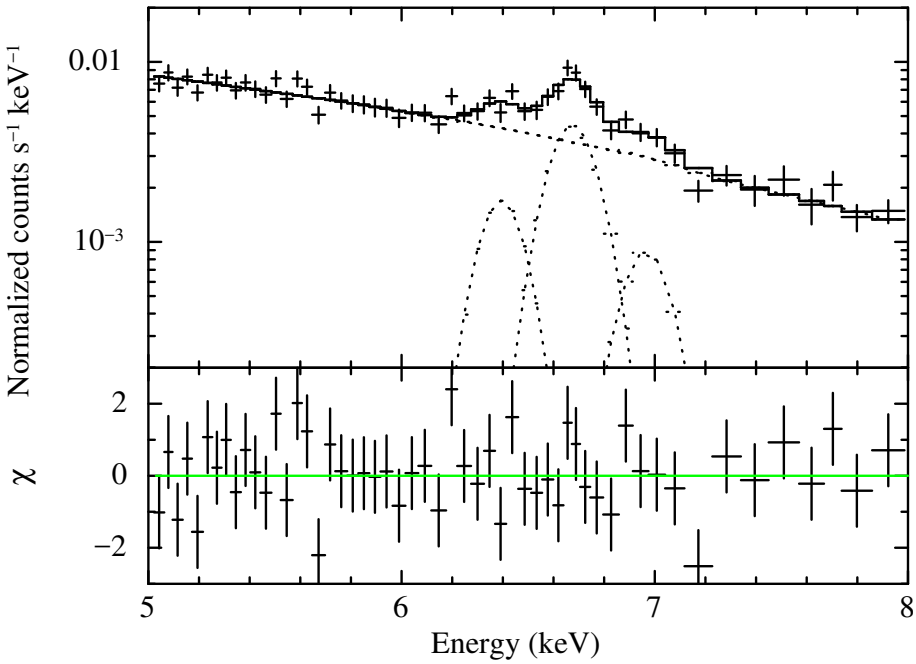

Figure 5.29: Top panel : 5–8 keV spectra of G359.0−0.9 extracted from the excess region, except for the diffuse emission seen in the 5–8 keV band fitted with a phenomenological model. The solid line in the top panel shows the best-fit model, while the dotted lines show the components of the model. Bottom panel : Residuals between the data and the best-fit model.

5.12 G359.1−0.5

X-ray images

Figures 5.30 show the NXB subtracted and exposure corrected XIS images of G359.1−0.5 in the 0.5–3 keV (a), 5–8 keV (b) and 6.3–6.5 keV (c) bands. The images of 0.5–3 keV and 5–8 keV bands are binned with 8×8 pixels and then smoothed with a Gaussian function of $\sigma = 3$ bins. The 6.3–6.5 keV image is binned with 32×32 pixels and then smoothed with a Gaussian function of $\sigma = 6$ bins.

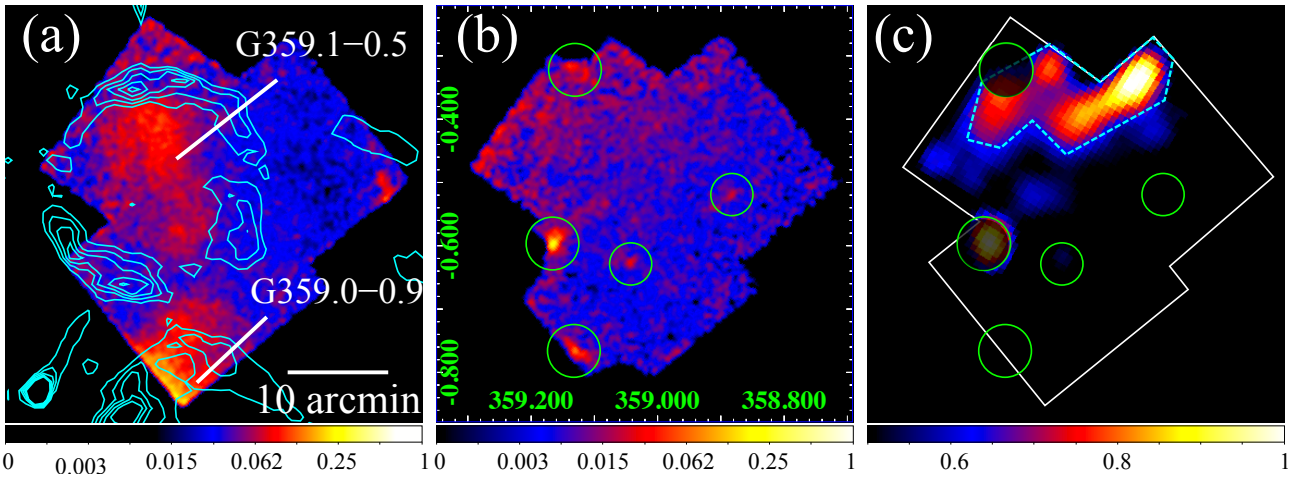

Figure 5.30: (a) : XIS0+1+3 image of G359.1−0.5 in the 0.5–3 keV. The image is binned with 8×8 pixels and then smoothed with a Gaussian function of $\sigma = 3$ bins. The cyan contours show the 843 MHz radio continuum intensity taken from the Skyview homepage. (b) : XIS0+3 image in the 5–8 keV. The binning and the smoothing is same as that of (a). Green circle shows the position of the point-lie source. (c) : XIS0+3 image in the 6.3–6.5 keV band (c). The image is binned with 32×32 pixels and then smoothed with a Gaussian function of $\sigma = 6$ bins. The regions surrounded with cyan dashed lines is the "excess" region, and the remaining part of the field of view is the "reference" region. The color scales are normalized so that the bright pixel is 1.

In the 0.5–3 keV band, there are two distinct diffuse enhancements which correspond to X-ray emission from G359.0−0.9 and G359.1−0.5. The diffuse X-ray emission of G359.1−0.5 locates in the radio shell. In the 5–8 keV band, on the other hand, no bright diffuse emission is seen in the radio shell. The northwestern part of the image is brighter than the southeastern part. This tendency is roughly consistent with the distribution of GRXE and GCXE, which are brighter for lower absolute Galactic latitude. In the 6.3–6.5 keV band, an enhancement is seen in the northwestern part of the image.

X-ray spectra

The excess region is defined as the areas surrounded by dashed lines in figure 5.30(c). Five point-like sources surrounded by green circles in figures 5.30 were removed from the excess region with circles with a radius of 2′.0. The whole field except for the excess region and the point-like sources was defined as the reference region.

The spectra of the excess and reference regions were fitted with the power-law plus four Gaussians function model. The model can explain both of the spectra with $\chi^2_{\rm red} = 1.08$ (46 d.o.f.) for the excess region and $\chi^2_{\rm red} = 1.09$ (97 d.o.f.) for the reference region. The best-fit parameters obtained in the fitting are summarized in table 5.13.

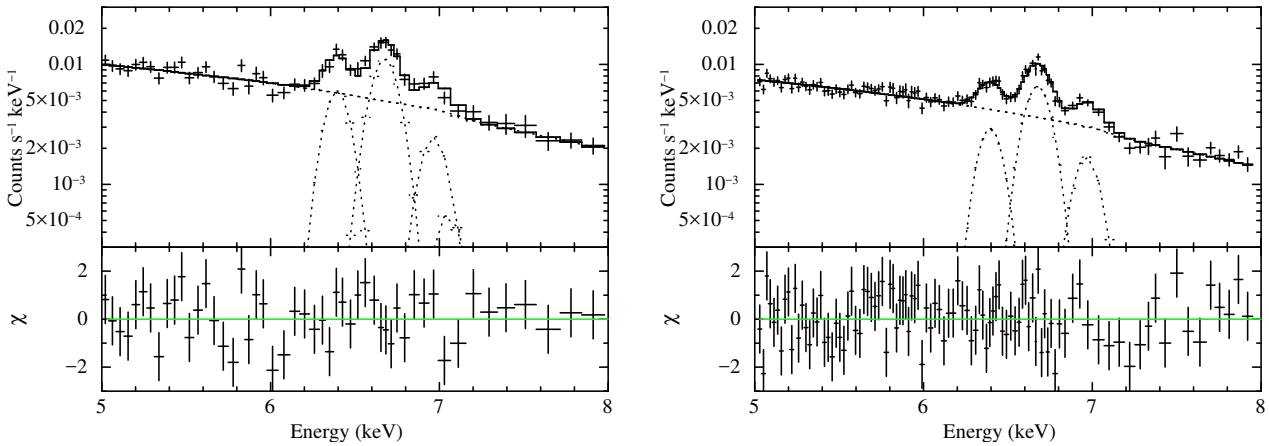

Figure 5.31: Top panels : NXB subtracted spectra of G359.1−0.5 extracted from the excess (left) and reference (right) regions, fitted with the power-law plus four Gaussian functions models in the 5–8 keV band. The vertical axes are normalized with the areas of the regions. The best-fit models are plotted with the solid lines, while each component is plotted with the dotted line. Bottom panels: Residuals between the data and the best-fit models.

Table 5.13: Best-fit parameters for the excess and reference regions of G359.1−0.5.

Parameter	Best-fit value		
	Excess region	Reference region	Reference region (corrected) [3]
Power-law photon index	1.9 ± 0.3	2.1 ± 0.2	
Power-law intensity[1]	200 ± 8	147 ± 3	173 ± 6
Fe I Kα Intensity[2]	12.1 ± 2.2	5.8 ± 0.8	10.5 ± 1.5
Fe XXV Kα Intensity[2]	25.9 ± 2.7	15.0 ± 1.0	23.2 ± 1.5
Fe XXVI Kα Intensity[2]	6.2 ± 2.2	4.3 ± 0.8	6.3 ± 1.2

[1] Observed intensity in the 5.0–8.0 keV band in the unit photons cm^{-2} s^{-1} arcmin^{-2}.
[2] Observed intensity in the unit of 10^{-8} photons cm^{-2} s^{-1} arcmin^{-2}.
[3] Parameters for the reference region after the correction by the latitude profiles of GCXE and GBXE.

All of the intensities of the power-law, Fe I Kα ,Fe XXV Kα and Fe XXVI Kα lines in the

excess region is significantly higher than those in the reference region. This would be caused by a latitude distribution of the GDXE, since the excess region locates closer to the Galactic plane. At the position of G359.1−0.5, the GDXE is dominated by the GCXE and GBXE. Assuming that the X-ray emission in the reference region consists of the combination of the GCXE and GBXE, the observed intensities of the Fe Kα lines and the power-law were corrected to the intensities predicted in the excess region, using the e-folding scales along the Galactic longitude obtained in Uchiyama et al. (2013), see table 2.2. Since the barycenters for the excess region and the reference region are $(l, b) = (359.^{\circ}024, -0.369)$ and $(l, b) = (358.^{\circ}999, -0.561)$, the intensities of the Fe I, Fe XXV Fe XXVI Kα lines and the power-law in the reference region were multiplied by 1.80, 1.55, 1.48 and 1.27, respectively. The corrected intensities are also summarized in table 5.13.

After the correction of the GCXE and GBXE distribution, the enhancements in the line intensities become not significant with 1.0σ (Fe I Kα), 1.7σ (Fe XXV Kα) and $< 1\sigma$ (Fe XXVI Kα). The intensity for the power-law component is also consistent with each other. Thus it is concluded that the Fe I Kα in the excess region is not significantly higher than the reference region, when the intensity profiles of the GCXE and GRXE are considered.

5.13 Summary of the systematic analysis

Table 5.14 shows a summary of the systematic search for the 6.4 keV line in the eleven Galactic SNRs. G304.6+0.1, G323.7+1.0 and G346.6−0.2 show clear excess of the 6.4 keV line with confidence levels greater than 3σ. In addition, G330.2+1.0 and G348.5+0.1 show the signs for the enhancement with confidence levels of $> 2\sigma$. It is concluded that these three samples show significant enhancement of the 6.4 keV line coincident with each SNR. To investigate the property of the 6.4 keV line enhancements, more detailed analysis for G304.6+0.1, G323.7+1.0 and G346.6−0.2, which show $> 3\sigma$ excess in the 6.4 keV line, is performed in the next section.

Although the absorption column density was fixed to the value obtained by Uchiyama et al. (2013), the degree of the absorption does not significantly affect the results. Even when we fit the spectra of the excess and reference regions of each SNR without any consideration of the absorption, the significance level of the enhancements in G304.6+0.1, G323.7+1.0 and G346.6−0.2 are higher than 3σ, while that of the other SNRs are lower than 3σ.

Table 5.14: Summary of the systematic analysis for 11 SNRs

SNR name	Fe I Kα line intensity[1]			Notation
	Excess region	Reference region	Excess significance	
G290.1−0.8	< 1.8	< 0.4	N/A	[2]
G298.6−0.0	< 2.0	< 0.6	N/A	[2]
G304.6+0.1	4.2 ± 1.6	< 1.0	3.6σ	
G323.7+1.0	4.3 ± 1.6	< 0.8	4.1σ	
G330.2+1.0	4.9 ± 2.8	< 0.9	2.7σ	[3]
G346.6−0.2	5.6 ± 2.3	< 1.8	3.2σ	
G348.5+0.1	4.5 ± 1.8	< 3.0	2.2σ	
G348.7+0.3	< 4.8	1.2 ± 1.0	N/A	[2]
G355.6−0.0	5.9 ± 3.4	< 3.0	1.9σ	[4]
G359.0−0.9	5.6 ± 1.9	3.3 ± 0.7	1.9σ	[5]
G359.1−0.5	12.1 ± 2.2	10.5 ± 1.5	1.0σ	[6]

[1] Line intensities in the units of 10^{-8} photons s^{-1} cm^{-2} $arcmin^{-2}$.
[2] Only upper limits are obtained for the Fe I Kα line intensity in the excess region.
[3] The excess region for G330.2+1.0 corresponds to the region number 5 in section 5.6.
[4] Only the enhancement in the region W (see section 5.10) is used in the summary.
[5] The area, where the diffuse emission in the 5–8 keV is seen, is included in the excess region
[6] The intensity in the reference region is the value after the correction for the intensity profiles of GCXE and GBXE.

Chapter 6

Detailed analysis and results of the 6.4 keV line enhancements

6.1 Comparison between the observed line intensities and the GRXE

Since the GRXE exhibits strong Fe Kα lines, the 6.4 keV line enhancements seen in the SNRs might be explained by the fluctuation of the GRXE. To investigate the possibility, the observed 6.4 keV line intensities in G304.6+0.1, G323.7−1.0 and G346.6−0.2 were compared with the Fe I Kα intensity profile of the GRXE.

Yamauchi et al. (2016) made the Galactic longitude profile of the Fe I Kα intensity using the data within $|b| \leq 1.^\circ0$ (see figure 2.10). Although the intensity depends on the Galactic latitude, the latitude distribution was not considered in Yamauchi et al. (2016). We corrected the latitude distribution and made a new Galactic longitude profile of the Fe I Kα intensity at the Galactic latitude of each SNR. The latitude distribution of the Fe I Kα intensity was assumed to be represented by an exponential function with an e-folding scale of $0.^\circ5$ based on Yamauchi et al. (2016).

In the case of G304.6+0.1, for example, the Galactic latitude of the SNR is $b = 0.^\circ1$ hence $b_* = 0.^\circ146$ (the definition of the coordinates (l_*, b_*) are shown in section 2.5). Thus an Fe I Kα intensity of the GRXE obtained using the data at b_* was multiplied by a factor of $\exp(-0.^\circ146/0.^\circ5)/\exp(-b_*/0.^\circ5)$. All data points of the GRXE intensity in the western side of the Galactic plane were corrected by the same way. Figure 6.1 shows the corrected Fe Kα intensity profile of the GRXE (blue) and the observed 6.4 keV line intensities in the excess (red) and reference (black) regions of G304.6+0.1. Because of the absence of the GRXE data at $|l_*| > 40^\circ$, the Fe I Kα intensity of the GRXE at the position of G304.6+0.1 is unclear.

The 6.4 keV line intensities of G323.7−1.0 and G346.6−0.2 were also compared with the

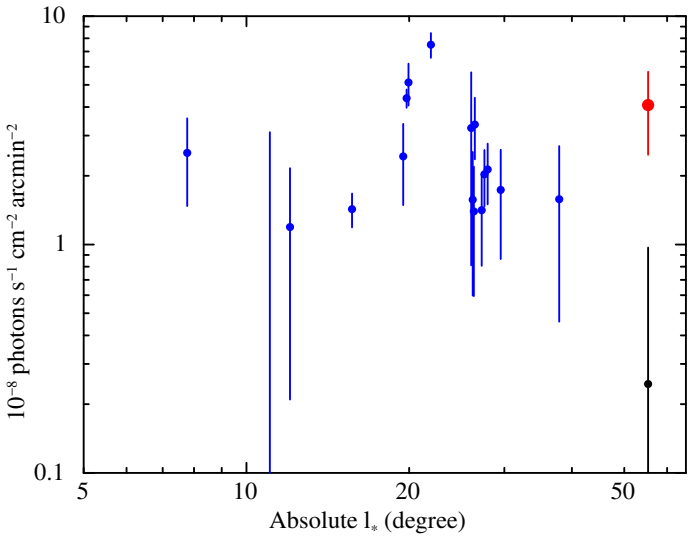

Figure 6.1: Comparison between the Fe I Kα intensity profile of the GRXE (blue) and the observed 6.4 keV line intensity in the excess (red) and reference (black) regions of G304.6+0.1. The error bar of each data point of the GRXE profile shows the 1σ confidence level, while that of the 6.4 keV line intensities in the excess and reference regions show the 90% confidence level.

GRXE. The Galactic latitude of G323.7−1.0 and G346.6−0.2 are $b = -1.^\circ0$ and $b = -0.^\circ2$, respectively, and thus the Fe I Kα intensity of the GRXE at $b = -1.^\circ0$ ($|b_*| = 0.^\circ954$) and $b = -0.^\circ2$ ($|b_*| = 0.^\circ154$) were estimated. Figures 6.2 show the Fe I Kα intensities of the GRXE at $b = -1.^\circ0$ (left panel) and $b = -0.^\circ2$ (right panel). The observed 6.4 keV line intensity in the excess regions (red data points) and the reference regions (black data points) are also plotted.

In both of G323.7−1.0 and G346.6−0.2, the 6.4 keV line intensity in the reference regions are comparable with that of the Fe I Kα intensity of the GRXE. The intensities in the excess regions, on the other hand, are higher than the GRXE Fe I Kα intensities by factors of ~ 10 (G323.7−1.0) and ~ 4 (G346.6−0.2). Although G304.6+0.1 locates outside the range of the GRXE profile, we concluded that at least the enhancements in G323.7−1.0 and G346.6−0.2 do not the fluctuation of the GRXE. There are excess of the 6.4 keV line intensity in addition to the GRXE.

6.2 Equivalent width and energy centroid of the 6.4 keV line

To estimate the equivalent width of the 6.4 keV line enhancement of each SNR, the spectrum of the reference region was subtracted from that of the excess region after correcting the difference

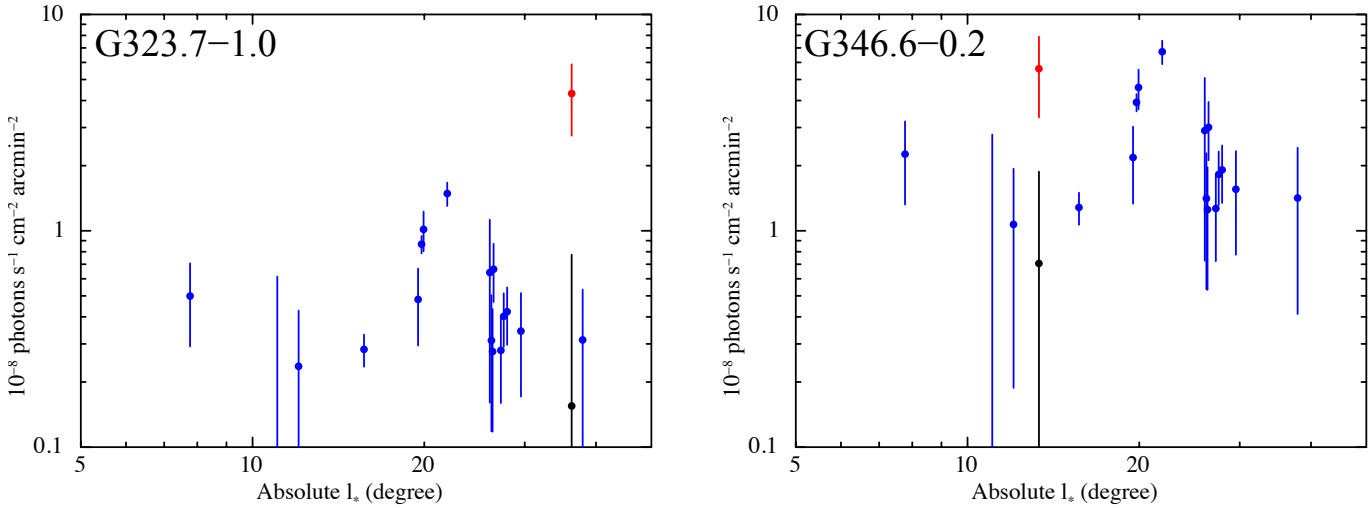

Figure 6.2: (Left panel) : Blue data points show the Fe I Kα intensity profile of the GRXE along the Galactic longitude at $b = -1.^\circ0$. The red and the black data points are the observed intensity of the 6.4 keV line in the excess and reference regions of G323.7−1.0. The error bar of each data point of the GRXE profiles shows the 1σ confidence level, while that of the 6.4 keV line intensities in the excess and reference regions show the 90% confidence level. (Right panel) : The same plot with the left panel, but the intensity profile of the GRXE at $b = -0.^\circ2$ and the observed intensity of G346.6−0.2.

of the area taking into account the vignetting. Figures 6.3 show the spectra of the excess regions of G304.6+0.1, G323.7−1.0 and G346.6−0.2 after the subtraction. The spectra were fitted with a model consisting of a power-law and two Gaussian functions. The energy centroids of the Gaussian functions were fixed to be 6.40 keV and 7.06 keV assuming the Fe I Kα and the Fe I Kβ lines, respectively. The intensity of the Fe I Kβ line was set to 0.125 times that of the Fe I Kα line. When the width of the 6.40 keV line was set to be a free parameter, it was consistent with zero in each SNR. The upper limits were 88 eV (G304.6+0.1), 92 eV (G323.7−1.0), and 104 eV (G346.6−0.2). Thus widths of both of the 6.40 keV and 7.06 keV lines were fixed to be zero. The best-fit parameters are summarized in table 6.1.

All three SNRs exhibit the quite large equivalent widths. The lower limits of the equivalent widths of G304.6+0.1, G323.7−1.0 and G346.6−0.2 are 670 eV, 2300 eV and 5200 eV, respectively. The continuum level and hence the equivalent width are sensitive to the vignetting correction. The lower limits become 440 eV, 1200 eV and 570 eV, respectively, when the uncertainty of the vignetting correction is assumed to be 5% according to *Suzaku technical description*.

Then the energy centroid of the gaussian functions for the 6.40 keV lines were arrowed to vary to investigated the energy centroids. The energy centroids are obtained as 6.38 ± 0.04 keV (G304.6+0.1), 6.40 ± 0.04 keV (G323.7−1.0) and $6.38^{+0.05}_{-0.04}$ keV (G346.6−0.2). These values

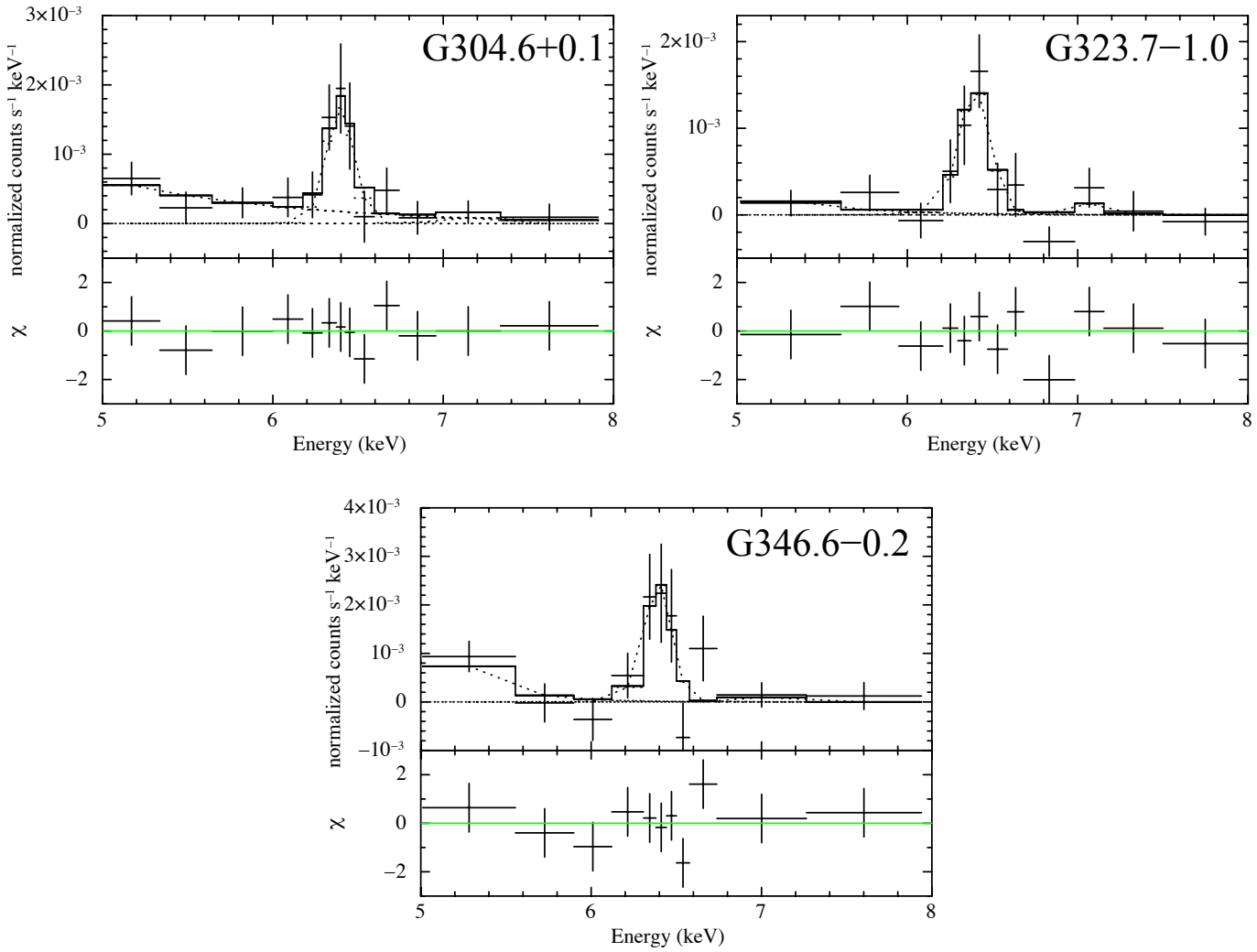

Figure 6.3: Spectra of the excess regions of G304.6+0.1 (top left), G323.7−1.0 (top right) and G346.6−0.2 (bottom), corresponding spectra of the reference regions are subtracted. The solid lines show the best-fit model consisting of a power-law and a Gaussian function.

are consistent with the Fe I Kα. The upper limits of 6.42–6.44 keV indicate that the Fe is less ionized than the ∼O-like or Ne-like states.

6.3 Combined spectrum of G304.6+0.1, G323.7−1.0 and G346.6−0.2

The spectral nature of the 6.4 keV enhancements of G304.6+0.1, G323.7−1.0 and G346.6−0.2 is similar with each other: the large equivalent widths and the low energy centroids hence the low ionization states. To investigate the enhancements in more detail, the spectra of G304.6+0.1,

Table 6.1: Best-fit parameters for the excess regions after the subtraction of the spectra of the background regions.

Parameter	Best-fit value		
	G304.6+0.1	G323.7−1.0	G346.6−0.2
Power-law photon index	$4.8^{+20.0}_{-4.9}$	N/A[2]	> 5.4
Power-law flux[1]	0.21 ± 0.20	< 1.5	$0.17^{+1.97}_{-0.10}$
6.4 keV line equivalent width(keV)	$1.9^{+46.0}_{-1.2}$	> 2.3	$30.0^{+38.9}_{-27.9}$

[1] Observed intensity in the 5.0–8.0 keV band in the unit of 10^{-11} photons cm^{-2} s^{-1} arcmin^{-2}.
[2] Both of the lower- and upper-limits are obtained within the 90% confidence level.

G323.7−1.0 and G346.6−0.2 were added altogether assuming that the 6.4 keV line in the three SNRs are emitted via the same mechanism.

The combined spectrum of the excess regions of G304.6+0.1, G323.7−1.0 and G346.6−0.2 is plotted with black data points in figure 6.4(a). The red data points in figure 6.4(a) shows that of the reference regions. Then the combined spectrum of the reference regions was subtracted from that of the excess regions. Figure 6.4(b) shows the combined spectrum of the excess regions after the subtraction. The subtracted spectrum was fitted with the model consisting of a power-law and two Gaussian functions, which is applied in section 6.2. The energy centroid of the Gaussian function for the 6.4 keV line was set to be a free parameter. The width of the 6.4 keV line was consistent with zero, and we obtained only an upper limit of < 76 eV. Thus the width was fixed to be zero hereafter. The spectral fitting gives the equivalent width of $2.5^{+9.9}_{-1.4}$ keV and the energy centroid of 6.40 ± 0.02 keV. When we take into account the systematic uncertainty of the vignetting correction, the lower-limit of the equivalent width become 760 eV. The upper limit of the energy centroid of 6.42 keV corresponds to the Fe Kα line with a charge number of about XIV (Mg-like state).

Next we tried to fit the combined spectrum of the excess regions assuming emission from ionizing plasma. The combined spectrum was fitted with the NEI model in `XSPEC`. The normalization, electron temperature and ionization timescale were set to be free parameters. The abundance of Fe was also a free parameter, while those of the other elements were fixed to the values of the Sun (Lodders, 2003). Figure 6.5 shows the combined spectrum fitted with the NEI model. Although the model represents the spectrum well, either a high Fe abundance and a high electron temperature are required. Figure 6.6 shows the delta-χ^2 map and the confidence contours for various electron temperatures (horizontal axis) and Fe abundances (vertical axis). If the electron temperature is 1 keV, at least the Fe abundance of 30 solar is needed to represent the observed spectrum at a confidence level of 90%. Even if the electron temperature reaches 5 keV, the Fe abundance higher than 3 solar is required. The ionization timescale is obtained to be $n_{\rm e}t < 3 \times 10^9$ s cm^{-3}, here $n_{\rm e}$ is the electron density in the plasma.

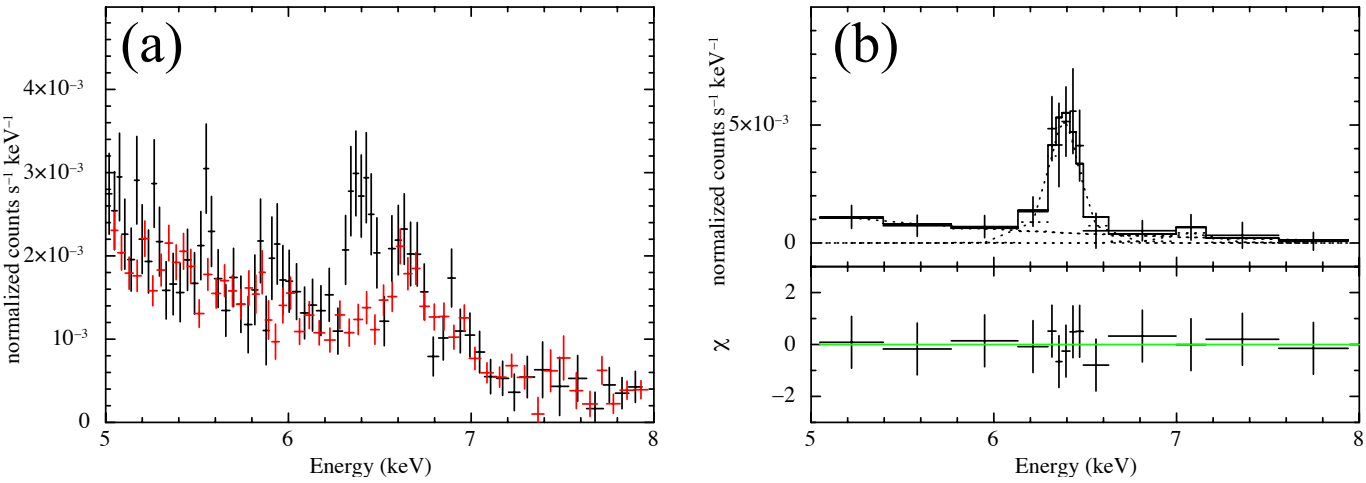

Figure 6.4: (a) : Combined spectrum of the excess regions (black) and the reference regions (red) of G304.6+0.1, G323.7−1.0 and G346.6−0.2. (b) : Top panel shows the combined spectrum of the excess regions, from which that of the reference regions is already subtracted. The best-fit power-law plus Gaussian functions model is plotted with the solid line. The dotted lines indicate the each component of the best-fit model. The residuals between the data and the best-fit model are shown in the bottom panel.

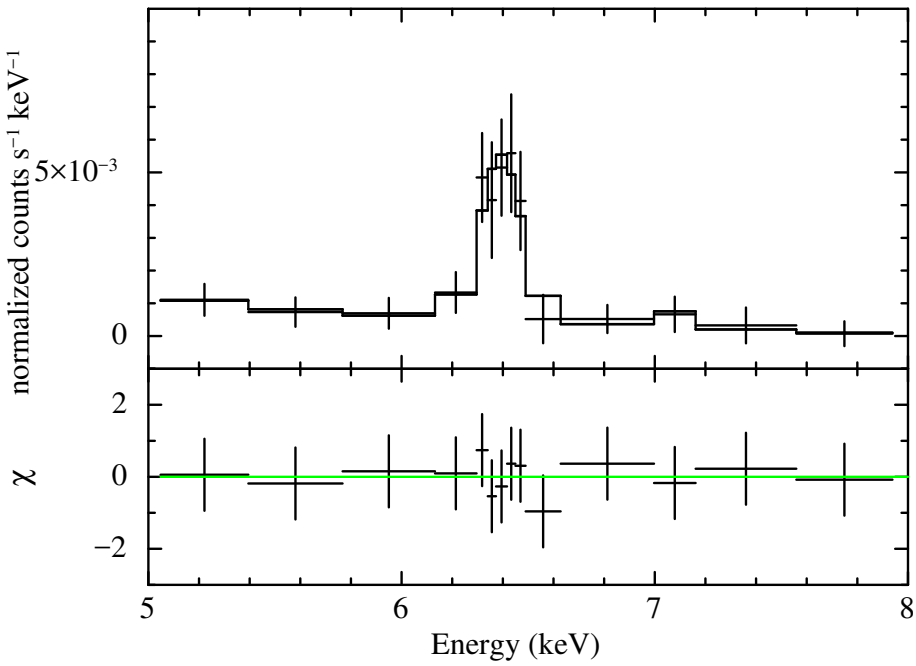

Figure 6.5: Same spectrum with figure 6.4(b), but fitted with the NEI model.

6.4 Spatial distribution of the 6.4 keV line enhancement

First, we made projection profiles of the 6.4 keV line enhancements seen in G304.6+0.1, G323.7−1.0, and G346.6−0.2 to test the expanse. In the case of G304.6+0.1, for example,

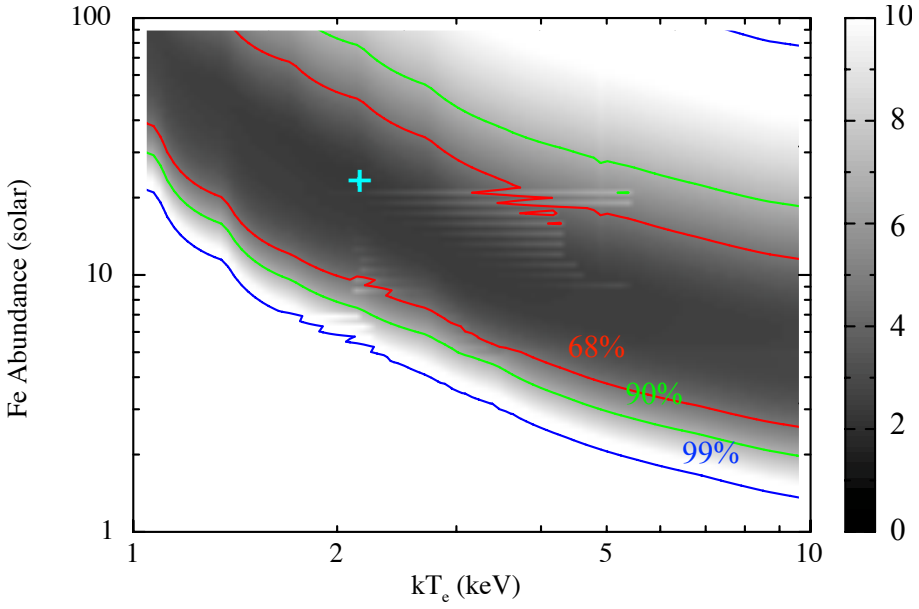

Figure 6.6: Delta-χ^2 map resulting from the fitting by the NEI model. The red, green and blue curves indicate the confidence contours corresponding to the levels of 68%, 90% and 99%, respectively. The cross point shows the best-fit value.

an X-ray count profile in the 6.3–6.5 keV band was made along the green arrow in the left panel of figure 6.7. Before to make the profile, the NXB was subtracted from the 6.3–6.5 keV band image and then the exposure correction was applied. Although the left panel of figure 6.7 was smoothed with a Gaussian function, the profile was made based on a non-smoothed image. The right panel of figure 6.7 shows the projection profile of the 6.4 keV line enhancement of G304.6+0.1. The horizontal dashed line shows an averaged count in the reference region. By the similar way, we also made projection profiles of the enhancements in G323.7−1.0 (figure 6.8) and G346.6−0.2 (figure 6.9).

Although the statistics are low, all of the three enhancements show the expanse with 5′ to 10′. The width of the point spread function of the Suzaku XRT, on the other hand, is $\sim 2'$ (see table 3.1), which is much smaller than the size of each bin in figures 6.7, 6.8, and 6.9. All of the enhancements expanse larger than the spatial resolution of the Suzaku XRT.

Table 6.2 shows the summary of the approximated size of the 6.4 keV line emitting regions in G304.6+0.1, G323.7−1.0, and G346.6−0.2. Each angular size was determined based on the 6.3–6.5 keV X-ray image. The actual size was calculated based on the angular size and the distance from the solar system obtained in the previous researches. The 6.4 keV line emitting regions are estimated to be larger than 10 pc.

Next we compare the spatial distribution of the 6.4 keV line enhancements and the thermal plasma. Figures 6.10 show the 6.3–6.5 keV band images of G304.6+0.1 (left), G323.7−1.0

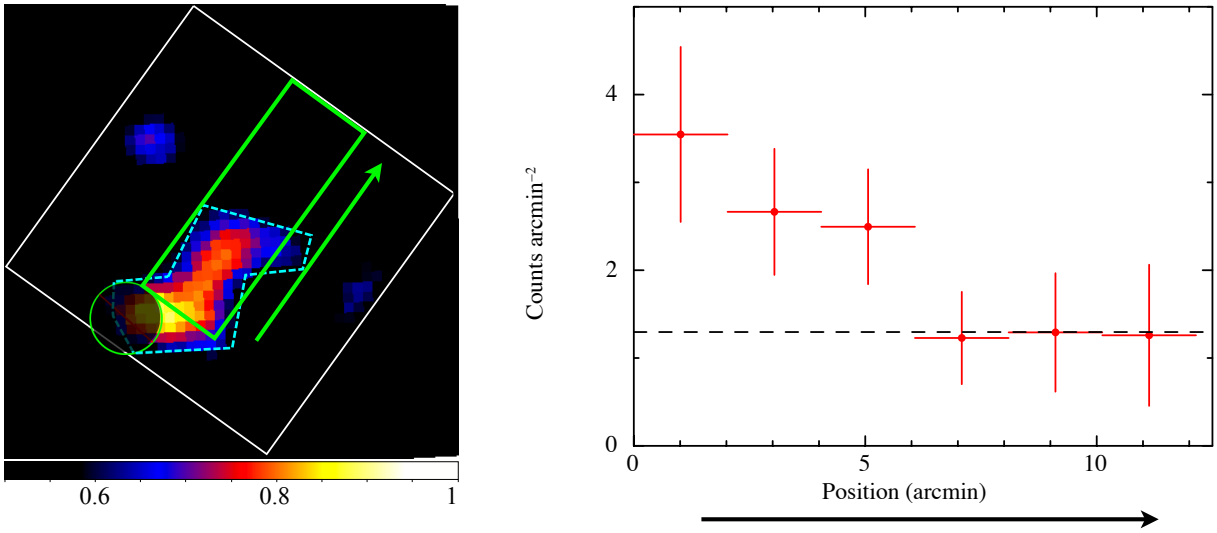

Figure 6.7: Left panel: The green rectangle indicates a region from which the projection profile was extracted. The color image is the same with figure 5.7(c). Right panel: Projection profile of the X-ray count in the 6.3–6.5 keV band along the direction of the green arrow in the left panel. The dashed line indicates the averaged count in the reference region. The error bar of each data point indicates the 1σ Poisson error.

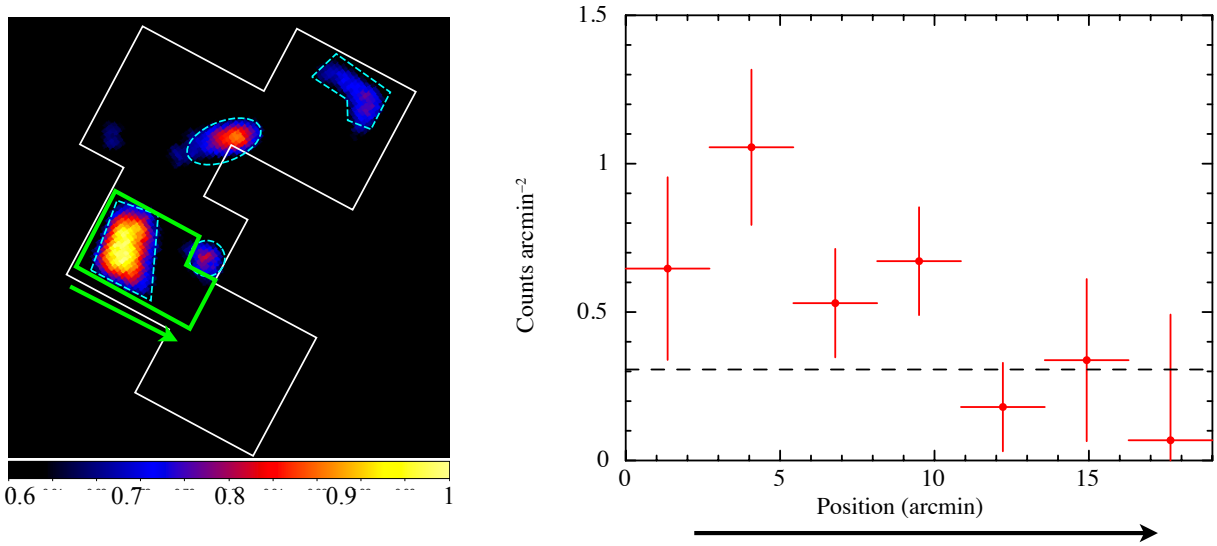

Figure 6.8: The same figure with figure 6.7 but for G323.7−1.0.

(center) and G346.6−0.2 (right) compared with the intensity distribution of the 0.5–3 keV X-rays (contours). Since the X-rays in the 0.5–3 keV band are dominated by emission from the low-temperature thermal plasma, the contours in figure 6.10 correspond to the distribution of the low-temperature thermal plasma. The contours of G323.7−1.0 are noisy since its thermal radiation is faint. The brightness peaks of the 6.4 keV line emission are apart from the radiation

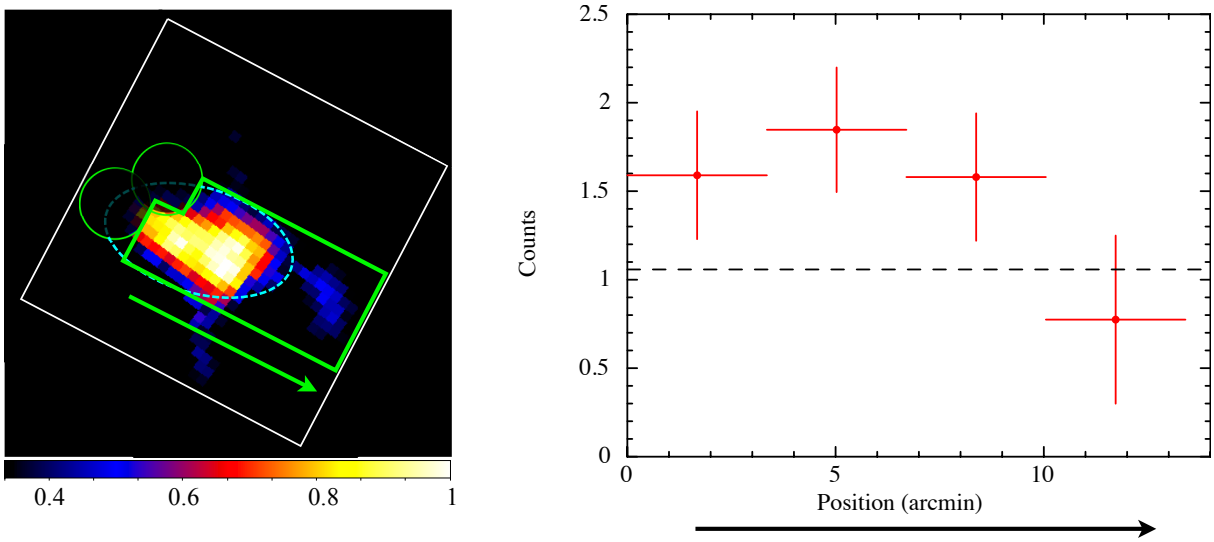

Figure 6.9: The same figure with figure 6.7 but for G346.6−0.2.

Table 6.2: Summary of the size of the 6.4 keV line emitting regions in G304.6+0.1, G323.7−1.0 and G346.6−0.2.

	Angular size[1]	Distance[2]	Actual size[3]
G304.6+0.1	$\sim 5'$	> 9.7 kpc[4]	> 15 pc
G323.7−1.0	$\sim 8'$[4]	5 kpc[5]	10 pc
G346.6−0.2	$\sim 8'$	5.5 kpc or 11 kpc[6]	10 pc or 20 pc

[1] Approximated angular size of the 6.4 keV line emitting region.
[2] Distance to the SNR from the solar system.
[3] Actual size of the 6.4 keV line emitting region calculated based on its angular size and the distance from the solar system.
[4] The size of the largest 6.4 keV clump.
[5] Caswell et al. (1975), [6] Araya (2017), [7] Koralesky et al. (1998)

in the 0.5–3 keV band, indicating that the 6.4 keV line emission does not associate with the low-temperature plasma.

Figures 6.11 show the 6.3–6.5 keV band images of G304.6+0.1 (left) and G346.6−0.2 (right) compared with the 843 MHz radio continuum of Whiteoak & Green (1996). The brightness peak of the 6.3–6.5 keV X-rays of G346.6−0.2 is almost coincident with the bright part of the radio shell in the southeastern rim. Although the 6.3–6.5 keV X-rays and the radio continuum are not strongly associated in G304.6+0.1, the distance from the brightness peak of the 6.3–6.5 keV X-rays to that of the radio continuum ($\sim 2'$) is smaller than that to the thermal X-ray emission's peak ($\sim 6'$). Figure 6.12 shows the contours of the 6.3–6.5 keV intensity overlapped on the 843 MHz radio map. The radio emission of G323.7−1.0 is quite weak and clear correlations cannot be seen. Roughly the 6.4 keV clumps locate near or on the radio shell.

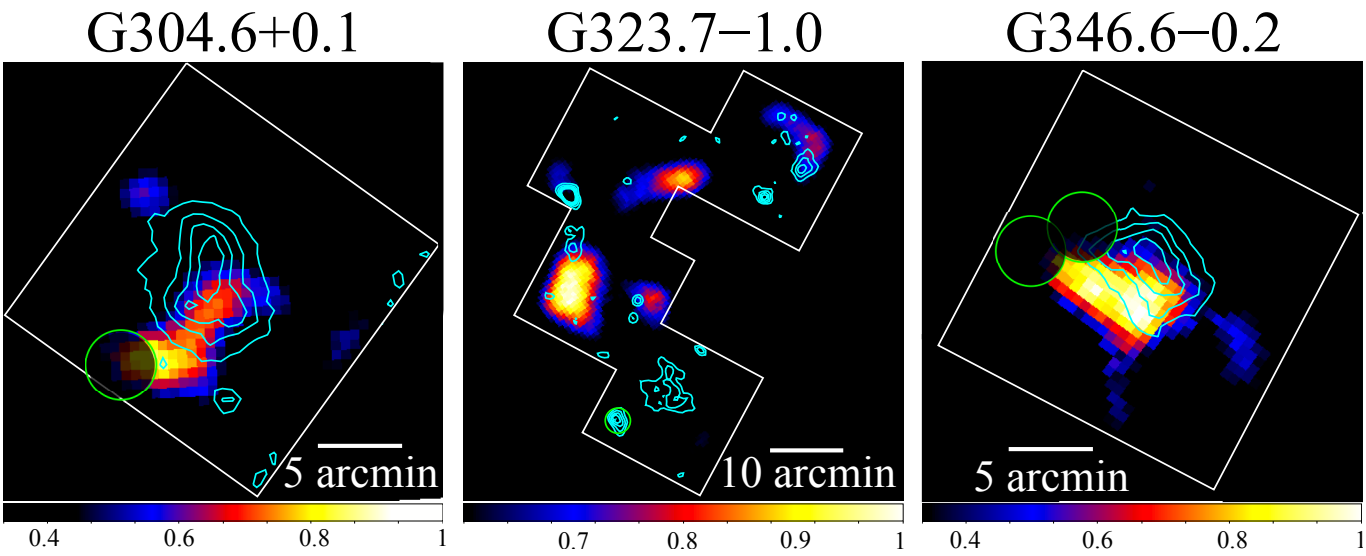

Figure 6.10: 6.3–6.5 keV band images of G304.6+0.1 (left), G323.7−1.0 (center) and G346.6−0.2 (right) compared with the 0.5–3 keV X-ray distribution (contours). The size of the binning and the smoothing for the images are the same with that applied in the systematic analysis (see chapter 5).

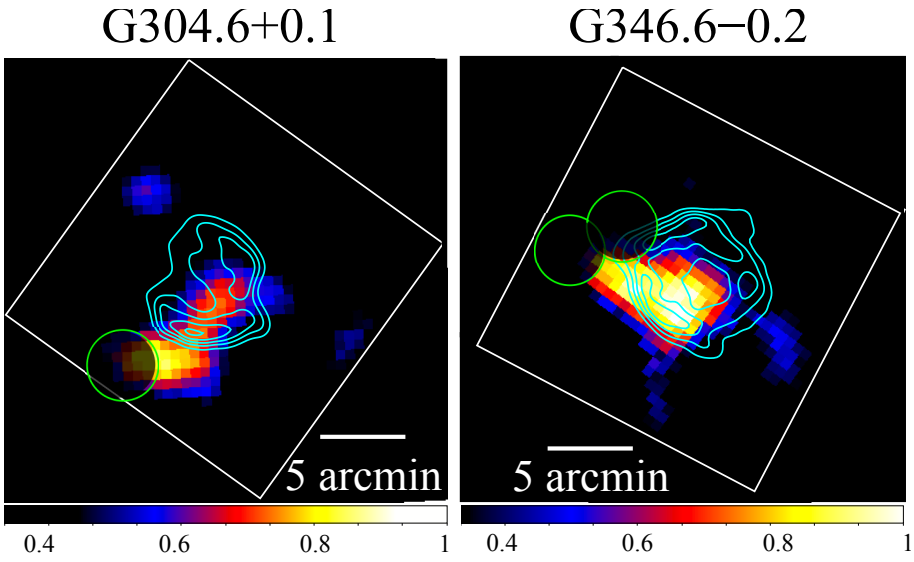

Figure 6.11: 6.3–6.5 keV band images of G304.6+0.1 (left) and G346.6−0.2 (right) compared with the 843 MHz radio distribution (contours). The color images are the same with that in figure 6.10. The contours of the 843 MHz radio intensity were made using the data of Whiteoak & Green (1996).

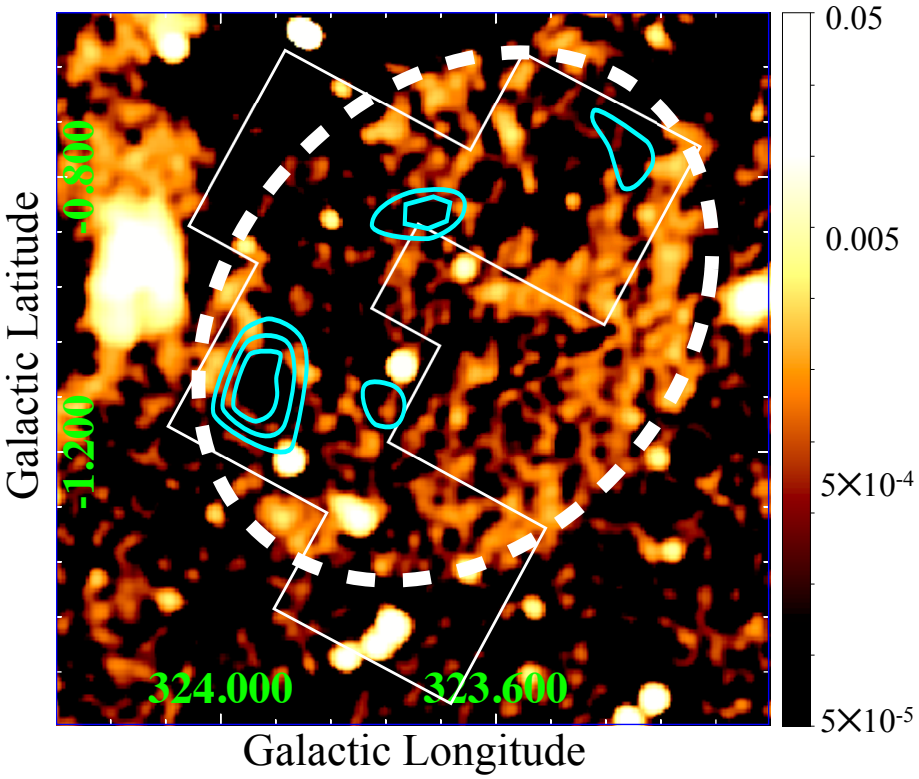

Figure 6.12: Contours of the 6.3–6.5 keV intensity overlapped on the 843 MHz radio map taken from the Skyview homepage. The dashed ellipse indicates the approximated shape of the radio shell.

Chapter 7

Discussion

7.1 Origin of the 6.4 keV emission line

7.1.1 Thermal plasma origin

IP can emit the iron K-shell line at ~ 6.4 keV. Indeed, the spectral model assuming the IP can represent the combined spectrum of G304.6+0.1, G323.7−1.0 and G346.6−0.2 (see section 6.3). The spectral fitting reveals that the high Fe abundance and the high electron temperature are required for the plasma, as well as the low-ionization state.

The electron temperature of the thermal plasma previously known in G304.6+0.1 ($kT_{\rm e} \sim 0.75$ keV) and G346.6−0.2 ($kT_{\rm e} \sim 0.3$ keV) is too low to emit the significant Fe Kα line. In addition, the spatial distribution of the 6.4 keV line is different from that of the soft X-rays in G304.6+0.1 and G346.6−0.2. Although the newly discovered soft source in G323.7−1.0 is possibly thermal plasma, the Fe Kα line emitted from the soft source is estimated to be 7×10^{-11} photons cm^{-2} s^{-1} arcmin^{-2} based on the best-fit parameters (see section 5.5). This value is about 500 times smaller than the observed 6.4 keV line intensity. In addition, the spatial distribution of the soft source is completely different from the 6.4 keV clumps. Thus the origin of the 6.4 keV line is not the thermal plasma seen in the soft X-rays.

Based on the spectral fitting by the IP model, the Fe abundance is required to be more than 3 solar if the electron temperature is assumed to be 5 keV. The electron temperature of the plasma in SNRs is lower than ~ 5 keV in general. The lower the electron temperature becomes, the higher Fe abundance is required to explain the observed spectrum. Such a high abundance could be realized only in Fe-rich ejecta. The ionization timescale obtained by the spectral fitting ($n_{\rm e}t < 3 \times 10^9$ s cm^{-3}) means that the thermal plasma originates from the ejecta is younger than $100(n_{\rm e}/1\ {\rm cm}^{-3})^{-1}$ yr. The ejecta in G304.6+0.1, G323.7−1.0 and G323.7−1.0 are quite unlikely in such a low ionization state due to the old age of the SNRs: the ages were estimated to be $(2.8\text{–}6.4) \times 10^4$ yr for G304.6+0.1 (Combi et al., 2010), $\sim 10^5$ yr for G323.7−1.0

(this work) and (1.4–1.6) $\times 10^4$ yr for G346.6−0.2 (Yamauchi et al., 2013). Indeed, Yamaguchi et al. (2014) reported that only young SNRs exhibit such a low energy centroid of ~ 6.42 keV using the Suzaku archive data of many SNRs.

The thermal plasma origin is also disfavored by the size of the 6.4 keV line emitting regions. The 6.4 keV line emitting regions were estimated to be larger than 10 pc (see table 6.2). If the origin of the 6.4 keV line is the thermal plasma, the plasma larger than 10 pc should be generated by the shock heating. When we assume a shock velocity of 3000 km s^{-1}, it takes about 3000 yr to cross 10 pc. Since G304.6+0.1, G323.7−1.0 and G323.7−1.0 are not young SNRs, the shock velocity would be slower than 3000 km s^{-1} and thus it takes more than 3000 yr to generate the thermal plasma with the size of 10 pc. Based on the fitting of the observed spectrum, on the other hand, the thermal plasma is younger than 100 yr assuming a typical electron density of ~ 1 cm^{-3}. It is impossible to generate the thermal plasma larger than 10 pc within 100 yr by the shock heating.

From the reasons above, the 6.4 keV line does not originate from the thermal plasma. The 6.4 keV line emission has to be explained by non-thermal processes such as K-shell ionization by photons, non-thermal electrons or protons with an energy above the Fe K-edge (7.1 keV). We discuss which particle is the dominant source for the observed 6.4 keV line emission.

7.1.2 Non-thermal processes

Photoionization

The 6.4 keV line can be produced by the photoionization. The equivalent width of the 6.4 keV line can be larger than the observed value, 760 eV, when the spectral photon index of the X-ray irradiating source is smaller than $\Gamma = 1.5$ in the case that the Fe abundance of the X-ray reflecting cloud is equal to that of the Sun (see figure 2.6). The photon index can be larger if the Fe abundance of the cloud is higher. In this prosess, bright X-ray sources are required in the vicinity of the SNR. We searched for luminous X-ray source near G304.6+0.1, G323.7−1.0 and G346.6−0.2, and estimated the luminosity required for the X-ray sources to generate the observed 6.4 keV line intensity.

We found that PSR B1259−63, which is a high-mass X-ray binary hosting a neutron star, is located ~ 1.2 degrees away from G304.6+0.1 (Greiner et al., 1995). The distance from the solar system to PSR B1259−63 is estimated to be 14±4 kpc from the parallax of 0.70±0.28 mas (Gaia Collaboration et al., 2016). The distance to G304.6+0.1, on the other hand, is estimated to be larger than 9.7 kpc by measuring the 21-cm absorption profiles (Caswell et al., 1975). When we assume that both of G304.6+0.1 and PSR B1259−63 locate 14 kpc away from the solar system, the distance between G304.6+0.1 and PSR B1259−63 is 13 kpc $\times$ sin(1.°2) = 290 pc. Since

the angular size of the 6.4 keV emitting region is $\sim 5'$, the actual size is ~ 20 pc. Then the hydrogen number density of the 6.4 keV emitting cloud is estimated to be ~ 340 cm^{-3} based on the empirical relation between the density and size of $n_{\rm H} = 180(D/40{\rm pc})^{-0.9}$ cm^{-3} (Scoville et al., 1987), where D is the size of the cloud. Note that there are no available data of ^{12}CO or HI with enough angular resolution to estimate the density of the cloud. With this assumption and the photon index of PSR B1259−63 ($\Gamma \sim 1.6$; Chernyakova et al., 2009), a luminosity of $\sim 1.3 \times 10^{39}$ erg s^{-1} in the 0.1–100 keV band is required for PSR B1259−63 to generate the observed intensity of the 6.4 keV line. The iron abundance of the cloud is assumed to be that of the Sun (Lodders, 2003). Since the luminosity exceeds the Eddington luminosity of a neutron star ($\sim 2 \times 10^{38}$ erg s^{-1}) by a factor of 6.5, the photoionization is unlikely to be the significant origin of the 6.4 keV line.

Cir X-1, which is an X-ray binary hosting a neutron star, is located $\sim 2^\circ$ away from G323.7−1.0. The distance from the Sun to Cir X-1 is estimated to be 4.1 kpc (Iaria et al., 2005). The minimum distance between G323.7−1.0 is 140 pc, and in this case the size of the 6.4 keV emitting region is ~ 10 pc. Then the hydrogen number density of the cloud is estimated to be ~ 600 cm^{-3} based on an empirical relation between the density and size. With this assumption and the photon index of Cir X-1 ($\Gamma = 2.6$; Iaria et al., 2005), a luminosity of $\sim 2.2 \times 10^{39}$ erg s^{-1} in the 0.1–100 keV band is required for Cir X-1. Since the luminosity exceeds the Eddington luminosity for a neutron star by an order of magnitude, Cir X-1 is not the significant source for the photoionization.

In the vicinity of G346.6−0.2, there are three bright X-ray sources; 1RXS J170849.0−400910, RX J1713.7−3946, and 4U 1708−40. The separations between G346.6−0.2 and these sources are $0.^\circ3$ (1RXS J170849.0−400910), $\sim 0.^\circ5$ (RX J1713.7−3946) and $0.^\circ7$ (4U 1708−40). The distance from the solar system to G346.6−0.2 is estimated to be 5.5 kpc or 11 kpc based on the line-of-sight velocity of the associated OH maser (Koralesky et al., 1998). The size of the 6.4 keV line emitting region of G346.6−0.2 is roughly $8'$. By the similar way applied for G304.6+0.1 and G323.7−1.0, we calculated the required luminosity for 1RXS J170849.0−400910, RX J1713.7−3946, and 4U 1708−40. The parameters used in the calculation and the results are summarized in table 7.1. All of the luminosity exceed that each X-ray source can emit, although that of 1RXS J170849.0−400910 exceed the Eddington luminosity of a neutron star only by a factor of two. The highest flux ever observed from 1RXS J170849.0−400910 is about 5×10^{-11} erg cm^{-2} s^{-1} in the 1–10 keV band (Scholz et al., 2014). An unabsorbed luminosity in the 0.1–100 keV band is estimated to be 5.2×10^{36} erg s^{-1}, assuming the photon index of $\Gamma = 3.1$ and the absorption column density of $N_{\rm H} = 2.434 \times 10^{22}$ cm^{-2} obtained in Scholz et al. (2014), and the distance of 5.5 kpc. This luminosity is about two orders of magnitude lower than that required. Thus these three X-ray sources are unlikely to be the significant source for

Table 7.1: Parameters used to calculate the luminosity required for the X-ray sources in the vicinity of G346.6−0.2.

	1RXS J170849.0−400910	RX J1713.7−3946	4U 1708−40
Object type	Neutron star[5]	SNR[7]	Neutron star[10]
Distance(kpc)[1]	Unknown	1[8]	10–15[11]
Minimum separations(pc)[2]	29	4500	130
Photon index[3]	3.1[6]	2.4[9]	2.42[12]
Required luminosity (erg s^{-1})[4]	4×10^{38}	1×10^{42}	9×10^{38}

[1] Distance from the solar system to the X-ray sources.
[2] Minimum separations between the X-ray sources and G346.6−0.2.
[3] Spectral photon index assumed in the calculation based on the previous researches.
[4] Required luminosity for the X-ray sources in the 0.1–100 keV band to generate the observed 6.4 keV line intensity.
[5] 1RXS J170849.0−400910 is an AXP and hence is a magnetar candidate (Scholz et al., 2014).
[6] Scholz et al. (2014)
[7] RX J1713.7−3946 is a famous SNR exhibiting non-thermal hard X-rays (e.g. Koyama et al., 1997).
[8] e.g. Pfeffermann & Aschenbach (1996); Koyama et al. (1997); Fukui et al. (2003)
[9] The averaged spectral index was observed to be $\Gamma = 2.4$–2.5(Koyama et al., 1997).
[10] 4U 1708−40 is a Low-mass X-ray binary hosting a neutron star.
[11] Estimated using the reddening in the infrared band (Revnivtsev et al., 2013).
[12] Migliari et al. (2003)

the photoionization.

Ionization by cosmic-ray electrons

A scenario that the Fe in the cold and dense cloud is ionized by cosmic-ray electrons might be possible. In this process, strong continuum emission must be generated by the bremsstrahlung. The equivalent width of the Fe Kα line for the bremsstrahlung is 400 eV at most assuming a solar abundance (see figure 2.8). Since the equivalent width of the observed 6.4 keV line is higher than 760 eV based on the combined spectrum of G304.6+0.1, G323.7−1.0 and G346.6−0.2, the Fe abundance has to be higher than 1.9 times of the solar value. The abundance is too high as the ISM and thus an Fe-rich material such as ejecta is required.

The brightest part of the 6.4 keV line emitting region in G304.6+0.1 locates outside the radio shell of the SNR. G346.6−0.2 also shows the sign that some part of the 6.4 keV line enhancement is outside the radio shell. These spatial distributions disfavor the ejecta origin, since the radio shell would be the outermost part of the SNR. In addition, as discussed in section 7.1.1, the ejecta in G304.6+0.1, G323.7−1.0 and G346.6−0.2 are unlikely to be low-ionized enough to explain the observed energy centroid.

Ionization by cosmic-ray protons

The 6.4 keV line can also be produced via ionization by protons. In this process, the equivalent width of the Fe I Kα emission can be higher than 1 keV for gas with a solar abundance (Dogiel et al., 2011) (see figure 2.8). Thus the observed equivalent width (> 760 eV) can naturally be explained with the proton origin. The Fe I Kα intensity is calculated by

$$I_{6.4\mathrm{keV}} = \frac{1}{4\pi} \int \sigma_{6.4\mathrm{keV}} v n_{\mathrm{H}} l Z_{\mathrm{Fe}} \frac{dN}{dE} dE, \tag{7.1}$$

where $\sigma_{6.4\mathrm{keV}}$ is the proton's cross-section for the Fe I Kα emission, v is the velocity of the proton, n_{H} is the hydrogen number density of the clump, l is the thickness of the clump along the line-of-sight, Z_{Fe} is the iron abundance of the clump, and dN/dE is the spectral number distribution of the proton.

Since the angular size of the 6.4 keV emitting region in G304.6+0.1 is $\sim 5'$, the thickness of the cloud along the line-of-sight is assumed to be $l = d\sin(8')$. Here d is the distance from the solar system to the 6.4 keV emitting region. When the spectrum of the cosmic-ray proton is set to be $dN/dE \propto E^{-2.7}$ assuming the Galactic cosmic-rays (Cronin, 1999), a proton energy density of $\sim 200(n_{\mathrm{H}}/100\ \mathrm{cm}^{-3})^{-1}(d/10\ \mathrm{kpc})^{-1}$ eV cm^{-3} (0.1–1000 MeV band) is required to generate the observed 6.4 keV line intensity. The abundance of the iron Z_{Fe} is assumed to be that of the Sun (Lodders, 2003). This energy density is much higher than the canonical value for the Galactic cosmic-ray (~ 1 eV cm^{-3}).

The angular size of the largest 6.4 keV clump of G323.7−1.0 is $\sim 8'$. Then the thickness of the clump along the line-of-sight is assumed to be $l = d\sin(8')$. By a similar calculation above, a proton energy density of $\sim 150(n_{\mathrm{H}}/100\ \mathrm{cm}^{-3})^{-1}(d/10\ \mathrm{kpc})^{-1}$ eV cm^{-3} in the 0.1–1000 MeV band is required to generate the 6.4 keV line intensity observed in G323.7−1.0.

We applied the similar estimation for G346.6−0.2 using its angular size of $8'$. Then, by a similar calculation, a proton energy density of $\sim 210(n_{\mathrm{H}}/100\ \mathrm{cm}^{-3})^{-1}(d/10\ \mathrm{kpc})^{-1}$ eV cm^{-3} in the 0.1–1000 MeV band is required.

Short summary

The origin of the 6.4 keV line observed in G304.6+0.1, G323.7−1.0 and G346.6−0.2 is not the thermal plasma, because of the quite low energy centroid of < 6.418 keV and the large equivalent width of > 760 eV. Then the non-thermal processes should be the origin of the 6.4 keV line. The photoionization scenario is rejected because of the absence of the X-ray irradiating source. The non-thermal electron scenario might be possible, but the anomalous large Fe abundance of 1.9 solar or more is required. The scenario of the ionization by protons with the energy of ~ 10 MeV can naturally explain the observed 6.4 keV lines in G304.6+0.1,

G323.7−1.0 and G346.6−0.2 without any anomalous assumption. Then we concluded that the protons with an energy of $\sim$ 10 MeV are the most plausible source of the non-thermal 6.4 keV line enhancement.

7.2 6.4 keV line enhancement and emission in the other wave length

7.2.1 Gamma-rays

Very high-energy gamma-rays have been detected in the GeV band from G304.6+0.1 (Wu et al., 2011; Gelfand et al., 2013) and in the GeV–TeV band from G323.7−1.0 (Araya, 2017; Puehlhofer et al., 2015). The radiation mechanism of such high-energy gamma-rays is explained by either (1) the inverse-Compton scattering of low-energy photons by high-energy electrons or (2) the decay of neutral pions generated by collisions between high-energy protons and an interstellar matter. The 6.4 keV line, on the other hand, is likely to be generated by the low-energy ($\sim$ 10 MeV) protons (see section 7.1). In this section, we discuss the relation between the high-energy protons in the gamma-ray emitting region and the low-energy protons in the 6.4 keV line emitting region.

Gamma-ray emission from G304.6+0.1 was investigated in Gelfand et al. (2013) using the Fermi-LAT data. Based on the radio, X-ray and gamma-ray spectra, they claimed that the gamma-rays are mainly generated by the decay of the pions produced by the high-energy protons. The cutoff energy of the proton spectrum was estimated to be higher than 500 GeV. The extent of the gamma-ray source, on the other hand, is not clear because of the large point spread function of the Fermi-LAT ($\sim 0.3^\circ$; Gelfand et al., 2013). The energy density of the cosmic-ray protons in the gamma-ray emitting region is unclear and thus the relation between the 6.4 keV line and gamma-ray emissions cannot be discussed in detail.

In G323.7−1.0, the brightness peak of the gamma-ray emission is about $20'$ away from the 6.4 keV clumps (see figures 5.9 and 5.10). If the origin of the gamma-rays is the high-energy protons, Araya (2017) found out that the proton spectrum can be represented by a power-law with a particle index of $s = 1.5$ (particle number density $\propto E^{-s}$) and a cut-off energy of 15 TeV. The total energy of the cosmic-ray protons in the gamma-ray emitting region was estimated to be 1.07×10^{49} erg $(d/1\ \mathrm{kpc})^2 (n_\mathrm{H}/1\ \mathrm{cm}^{-3})^{-1} = 1.07 \times 10^{49}$ erg $(d/10\ \mathrm{kpc})^2 (n_\mathrm{H}/100\ \mathrm{cm}^{-3})^{-1}$, where d and n_H are the source distance from the solar system and the averaged density of the target material, respectively (Araya, 2017). According to the TeV gamma-ray image in Puehlhofer et al. (2015), the size of the bright part of the gamma-ray source is $\sim 20'$ corresponding to the actual size of $60(d/10\ \mathrm{kpc})$ pc. The volume

can be calculated to be $3.3 \times 10^{60}(d/10\ \mathrm{kpc})^3\ \mathrm{cm}^3$ assuming a sphere with the diameter of $60(d/10\ \mathrm{kpc})$ pc. Then the averaged energy density of the cosmic-ray protons is calculated to be $1.9(n_\mathrm{H}/100\ \mathrm{cm}^{-3})^{-1}(d/10\ \mathrm{kpc})^{-1}$ eV cm^{-3} above 280 MeV. The energy density in the 0.1–1000 MeV band becomes $1.8 \times 10^{-2}(n_\mathrm{H}/100\ \mathrm{cm}^{-3})^{-1}(d/10\ \mathrm{kpc})^{-1}$ eV cm^{-3} when we assume the proton spectrum estimated in Araya (2017). The 0.1–1000 MeV proton energy density in the 6.4 keV clumps, $\sim 150(n_\mathrm{H}/100\ \mathrm{cm}^{-3})^{-1}(d/10\ \mathrm{kpc})^{-1}$ eV cm^{-3} (see section 7.1.2), is larger than this value with about four orders of magnitude. In other words, significant gamma-ray emission should be associated with the 6.4 keV clumps if the proton spectrum in the 6.4 keV clumps is the same with that in the gamma-ray source. Observationally, on the other hand, the gamma-rays are not associated with the 6.4 keV clumps (see figure 5.9). Thus the number density of GeV/TeV protons in the 6.4 keV clumps must be less than that in the gamma-ray region. This means either that the spectral index of the cosmic-ray protons in the 6.4 keV clumps is larger, or the cut-off energy is smaller than that in the gamma-ray emitting region.

Higher-energy protons easily escape from the acceleration site, since their mean free path is longer than those of the lower-energy ones (Ohira et al., 2011). The 6.4 keV line emitting region might be the acceleration site, and the escaped high-energy protons would hit a high-density cloud located far from the 6.4 keV region and produces the high-energy gamma-rays. More qualitative discussion on possible correlations between the 6.4 keV line and gamma-ray emissions require detailed studies on the 6.4 keV line, gamma-rays as well as the ^{12}CO or HI with an angular resolution better than a few arcmin. These would be future projects.

7.2.2 ^{12}CO line (molecular clouds)

^{12}CO(J = 2–1) observations for RX J1713.7−3946 were performed with the NANTEN2 4 m telescope (Sano et al., 2013). G346.6−0.2 was caught in a part of the observations and ^{12}CO (J = 2–1) data were obtained. Figure 7.1 shows the intensity map of the ^{12}CO (J = 2–1) in the line of sight velocity range of -84.3 – -65.5 km s^{-1}. The ^{12}CO clumps in this velocity range would be associated with G346.6−0.2, since the line of sight velocity of the OH masers interacting with the SNR is distributed from -79.3 to -73.9 km s^{-1} (Koralesky et al., 1998). Indeed, in this velocity range, small peaks of ^{12}CO intensity would be associated with the OH masers plotted with the yellow crosses in figure 7.1.

We can see a ^{12}CO clump in the northeast of the radio continuum shell. The northern part of the 6.4 keV line enhancement (red contours in figure 7.1) is roughly coincident with the ^{12}CO clump. If the origin of the 6.4 keV line is the low-energy cosmic-ray protons, its intensity is proportional to the multiplication of the target density and the cosmic-ray proton's energy density. Based on the ^{12}CO map, the target density in the northern part of the 6.4 keV line emitting region is higher than that in the southern part. The energy density of the cosmic-ray

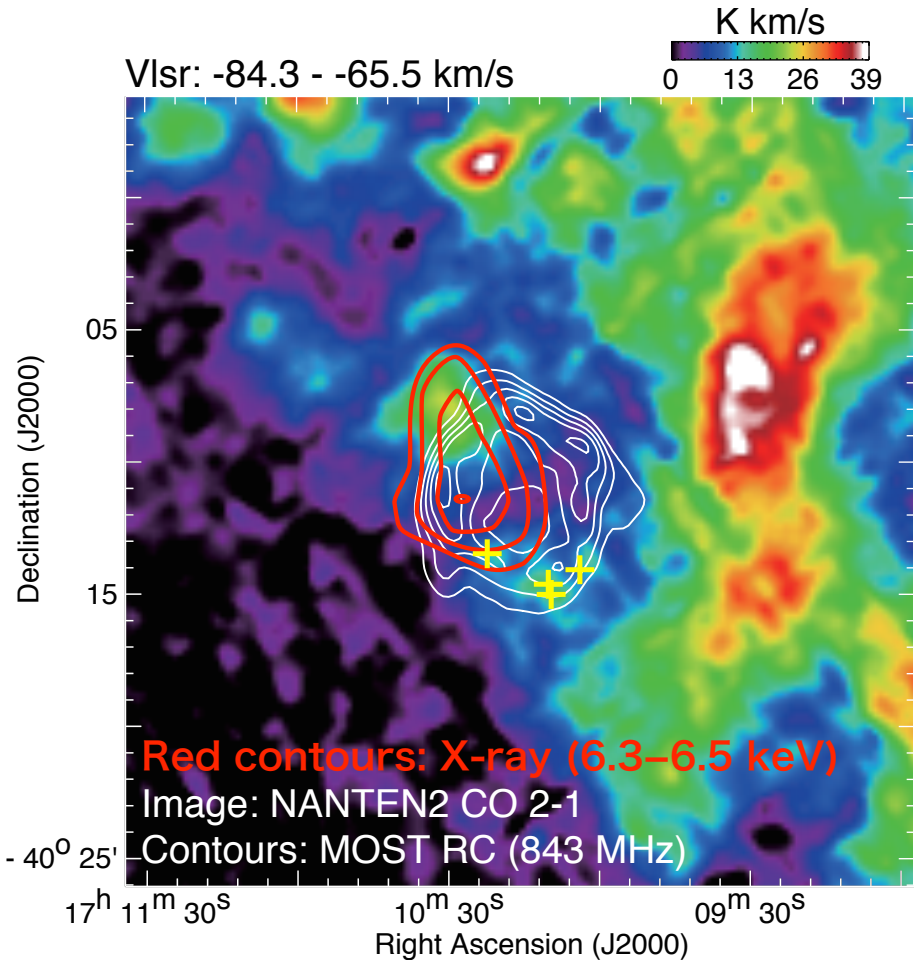

Figure 7.1: Color map shows the intensity of the ^{12}CO ($J = 2$–1) around G346.6−0.2 in the line of site velocity range of -84.3 – -65.5 km s^{-1}. The positions of the four OH masers (Koralesky et al., 1998) are marked with the yellow crosses. The radio continuum intensity at 843 MHz is shown by the white contours. The red contours indicate the 6.3–6.5 keV X-ray intensity.

protons would be higher in the southern part.

Neither for G304.6+0.1 and G323.7−1.0, there are available data of the ^{12}CO or HI with an enough angular resolution. The detailed observations for the molecular clouds around those SNRs can be helpful to understand the spatial distribution of the low-energy cosmic-rays.

7.2.3 Far-infrared (dust)

In the interstellar space, more than 99% of Fe is thought to be depleted onto dust grains (Draine, 1995). If the origin of the 6.4 keV line is Fe atoms in a dense cloud, infrared emission form the dust in the cloud should be seen. Figures 7.2 show the 140 μm far-infrared images of G304.6+0.1, G323.7−1.0 and G346.6−0.2 taken by AKARI. 140 μm is a peak wavelength of

the blackbody emission with a temperature of 20 K, and thus the images show the distribution of the dust not strongly heated.

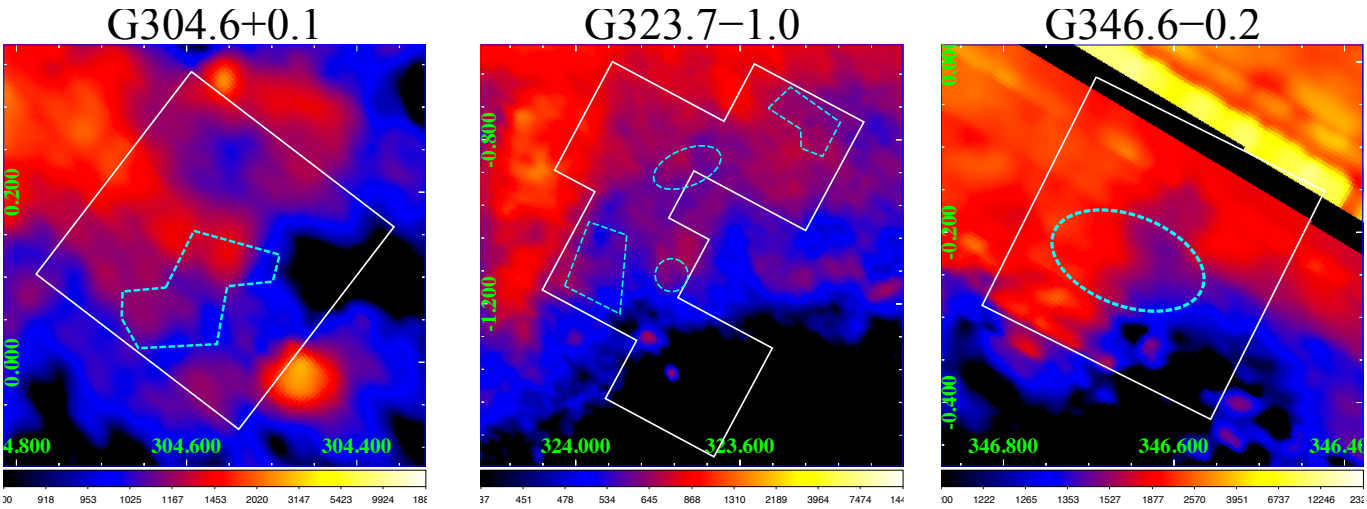

Figure 7.2: AKARI 140μm infrared images of G304.6+0.1, G323.7−1.0 and G346.6−0.2. The Suzaku fields of view and the excess regions are surrounded by the white solid and cyan dashed lines, respectively.

Since these SNRs locate on the Galactic plane, the far-infrared images are suffered from the background and/or foreground emissions. No clear association with the 6.4 keV enhancements are seen. The absence of the association means that the clouds emitting the 6.4 keV line are not so dense, or there are dense clouds but the dust grains in the clouds are destructed. If the dust grains are efficiently destructed, large amount of Fe would be in the gas-phase and in the low-ionization state. Such low-ionized gas-phase Fe has been detected in some SNRs (e.g. IC443; Kokusho et al., 2013) with the Fe II line emission at 1.257 μm and 1.644 μm. The Fe II line observations for G304.6+0.1, G323.7−1.0 and G346.6−0.2 would reveal the nature of the target material emitting the 6.4 keV line.

7.3 Characteristics of the SNRs and the 6.4 keV line

Table 7.2 shows the summary of the SNRs focusing on the 6.4 keV line intensities. In addition to the samples selected in this work, SNRs known to exhibit non-thermal 6.4 keV line emission are also listed: W28, Kes67, Kes69, Kes78, W44 (Nobukawa et al., 2017), and Kes 79 (Sato et al., 2016). The SNR age, presence of gamma-ray emission, the progenitor type, and the confirmation of the interaction between molecular clouds are the same information as summarized in tables 4.1 and 4.2. The radio intensities at 1 GHz were calculated based on the radio flux

and the size of the SNRs listed in Green (2014). When we calculated the areas of the SNRs, the shape of each SNR was approximated to be an ellipse.

Table 7.2: Summary of SNRs with 6.4 keV enhancement

SNR name	6.4 keV intensity[1]	SNR age (yr)	Radio intensity[2]	gamma-ray[3]	SN type[4]	MC interaction[5]
G290.1−0.8	< 1.8	$10,000$–$20,000$[8]	201	GeV[23]	CC[32]	possible[42]
G298.6−0.0	< 2.0	unknown	59	GeV[4]	unclear	–
G304.6+0.1	$3.8^{+1.7}_{-1.8}$	$28,000$–$64,000$[9]	280	GeV[24]	CC[33]	yes[43]
G323.7+1.0	$4.2^{+1.6}_{-1.7}$	$\sim 100,000$	> 0.4[22]	GeV[25], TeV[26]	unclear	–
G330.2+1.0	4.7 ± 2.8	$1,000$–$1,200$[10]	53	–	CC[34]	–
G346.6−0.2	$4.9^{+2.4}_{-2.6}$	$14,000$–$16,000$[11]	159	–	unclear[11,35]	yes[44,45]
G348.5+0.1	$3.4^{+2.2}_{-2.5}$	$\sim 24,000$[12]	408	GeV[24], TeV[27]	CC?[36]	yes[43]
G348.7+0.3	< 3.8	350–$3,150$[13]	115	GeV[28], TeV[29]	unclear	yes[43]
G355.6−0.0	4.4 ± 3.7	$\sim 20,000$[14]	425	–	unclear	–
G359.0−0.9	2.3 ± 1.9	$\sim 9,700$[15]	55	GeV[24]	unclear	–
G359.1−0.5	< 4.3	$\gtrsim 10,000$[16]	31	GeV[24]	CC?[37]	yes[46]
W28 (G006.4−0.1)	0.81 ± 0.52[6]	$\sim 36,000$[17]	171	GeV[24], TeV[30]	CC?[38]	yes[47]
Kes 67 (G018.8+0.3)	3.61 ± 1.35[6]	$\sim 100,000$[18]	225	–	unclear	yes[18]
Kes 69 (G021.8−0.6)	2.78 ± 0.95[6]	$\sim 5,000$[19]	207	–	unclear	yes[19]
Kes 78 (G032.8−0.1)	1.81 ± 0.89[6]	$13,000$–$63,000$[20]	48	GeV[24], TeV[31]	CC?[39]	yes[45]
W44 (G034.7−0.4)	1.26 ± 0.64[6]	$\sim 27,000$[21]	324	GeV[24]	CC[40]	yes[47]
Kes 79 (G033.6+0.1)	3.82 ± 1.40[7]	$\sim 27,000$[7]	64	–	CC[41]	yes[48]

[1] In the unit of 10^{-8} photons s^{-1} cm^{-2} keV^{-1}.
[2] Radio intensity at 1 GHz averaged over the SNR in the unit of mJy arcmin^{-2}, calculated based on (Green, 2014).
[3] "GeV" means that gamma-rays coincident with the SNR have been detected in the GeV band. "TeV" means the same but in the TeV band.
[4] Progenitor type of the SNR; Core-Collapse(CC), type Ia (Ia), or unclear.
[5] If the SNR is confirmed to be interacted with molecular clouds (MCs), "yes". "possible" means that there are signs for the interaction.
[6]Nobukawa et al. (2017). The errors show the 1σ confidence level.
[7]Sato et al. (2016). The intensity shows the averaged value in the "overall" region with the error in the 90% confidence level.
[8]Slane et al. (2002), [9]Combi et al. (2010), [10]Park et al. (2009), [11]Yamauchi et al. (2013), [12]Yamauchi et al. (2014)
[13]Nakamura et al. (2009), [14]Minami et al. (2013), [15]Leahy (1989), [16]Bamba et al. (2000), [17]Rho & Borkowski (2002)
[18]Dubner et al. (2004), [19]Tian & Leahy (2008), [20]Bamba et al. (2016b), [21]Park et al. (2013), [22]Flux at (at 843 MHz) obtained in Green et al. (2014)
[23]Auchettl et al. (2015), [24]Acero et al. (2016), [25]Araya (2017), [26]Puehlhofer et al. (2015), [27]Aharonian et al. (2008c),
[28]Xin et al. (2016), [29]Aharonian et al. (2008b), [30]Aharonian et al. (2008a), [31]Kosack et al. (2011), [32]García et al. (2012)
[32]García et al. (2012), [33]Washino et al. (2016), [34]Park et al. (2006), [35]Sezer et al. (2011a), [36]Yamauchi et al. (2013), [37]Bamba et al. (2000)
[38]Sawada & Koyama (2012), [39]Bamba et al. (2016b), [40]Wolszczan et al. (1991), [41]Giacani et al. (2009), [42]Filipovic et al. (2005)
[43]Frail et al. (1996), [44]Green et al. (1997), [45]Koralesky et al. (1998) [46]Lazendic et al. (2002), [47]Yamauchi et al. (2014)
[48]Kilpatrick et al. (2016)

G304.6+0.1 and G346.6−0.2 are categorized into middle-aged or old SNRs. Although the age of G323.7−1.0 is unclear, it would be an old SNR because of its large and extremely faint radio shell (see section 5.5). Thus it can be said that at least middle-aged – old SNRs can exhibit significant 6.4 keV line enhancement. Many young SNRs were removed from the sample because they usually have hot plasma with the temperature higher than 1 keV. The property of the non-thermal 6.4 keV line including the young SNRs are hard to be examined because of strong iron K-shell emission lines originate from the thermal processes.

The radio flux of G323.7−1.0 has not been measured in the 1 GHz band, but measured by the Molonglo observatory Synthesis Telescope (MOST). Since the MOST is not sensitive to smooth structure on a scale larger than $30'$, only a lower limit in the 843 MHz band was obtained (Green et al., 2014). We estimated the radio intensity at 1 GHz assuming a typical spectrum of the radio emission of SNRs, $S_\nu \propto \nu^{-0.5}$ (Green, 2014). Here S_ν is the energy flux density at the frequency ν. The radio intensity of G323.7−1.0 at 1 GHz was calculated to be > 0.36 mJy amin^{-2}. The relation between the intensities of the radio continuum at 1 GHz and the 6.4 keV line is plotted in figure 7.3. No clear correlation can be seen due to the large error bars for the 6.4 keV line intensities. X-ray data with more high statistics and high energy resolution obtained by future missions such as XARM or Athena make it possible to discuss the relation.

Gamma-ray emission has been detected from many SNRs in the GeV and/or TeV bands independent on the significance levels of the 6.4 keV line detection. G346.6−0.2, on the other hand, exhibits significant 6.4 keV line enhancement without any gamma-ray detection. Thus the intensity of the non-thermal 6.4 keV line is unlikely to be related to the gamma-ray emission.

Although the progenitor types of 8 out of 17 SNRs in table 7.2 are unclear and no SNRs have been confirmed to originate from type Ia SNe, at least CC SNRs can exhibit the non-thermal 6.4 keV line emission. Yamaguchi et al. (2014) reported that the energy centroids of the thermal Fe Kα lines from CC SNRs are significantly higher than 6.4 keV (see section 2.3). In other words, the result supports the idea that the observed 6.4 keV line enhancement does not originate from thermal processes.

Due to the short lifetimes of massive stars, most CC SNe are thought to occur inside dense molecular clouds. Indeed, 11 out of 17 SNRs in table 7.2 have been confirmed to be interacting with molecular clouds. The interactions with molecular clouds have not been confirmed in G323.7−1.0 since no observations have been performed. For G323.7−1.0, observations of ^{12}CO or HI with an angular resolution better than a few arcmin as well as OH maser are required to discuss the relation between the 6.4 keV line and the molecular cloud interaction. These would be future projects.

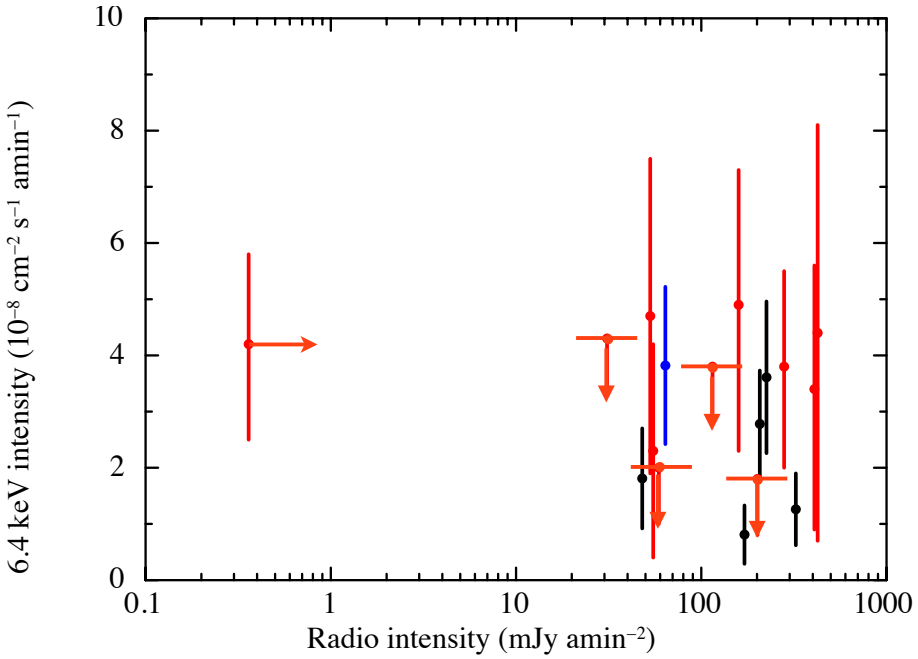

Figure 7.3: Relation of the intensities between the radio and 6.4 keV line in the SNRs. The horizontal axis shows the averaged intensity of the radio continuum at 1 GHz (see table 7.2), while the vertical axis shows the 6.4 keV line intensity of the enhancement. The SNRs analyzed in this work are plotted with red data points. Black and blue data points show the SNRs investigated in Nobukawa et al. (2017) and Sato et al. (2016), respectively. The error bars of the black data points indicate the 1σ confidence level, while that of the other data points are in the 90% confidence level.

7.4 Implications to the GDXE

GDXE shows the Fe I, Fe XXV, and Fe XXVI Kα lines. Revnivtsev & Sazonov (2007) resolved about 20% of the GRXE flux into point sources with the detection limit of $\sim 10^{31}$ erg s^{-1} in the 1–7 keV band at $(l, b) \sim (28.^{\circ}5, -0.^{\circ}0)$. However, Nobukawa et al. (2016) reported that the GRXE spectrum could not be well fitted with any combination of point sources of magnetic CVs, non-magnetic CVs, and active binaries. The Fe I Kα flux of the GRXE was ~ 2 times larger than that estimated from the combined model of the magnetic CVs, non-magnetic CVs, and active binaries. The spectrum of the GRXE is different between the eastern side and the western side of the Galactic plane. The difference is described by a combination of a power-law and a 6.4 keV line (Nobukawa et al., 2015). The equivalent width of the 6.4 keV line is ~ 1.3 keV. If the origin of the excess in the 6.4 keV line of the GRXE is the low-energy cosmic-ray proton, the authors estimated that the averaged proton energy density is 80 eV cm^{-3}.

We suggest that old SNRs can be the source of the 6.4 keV line of the GRXE. In the last

phase of the SNR evolution (disappearance phase), the expansion speed drops and the shock wave no longer lasts. Then the radio continuum emission becomes weaker and weaker. On the Galactic plane, there should be old SNRs which have not been discovered due to the low surface brightness of the radio emission. The radio emission is radiated from the electrons in the energy band of $\sim$ GeV. The 6.4 keV line, on the other hand, is generated by the protons with an energy of $\sim$ 10 MeV, if the origin is the low-energy cosmic-ray proton. There might be protons which can generate the 6.4 keV line even though there is no significant radio continuum emission. In fact, the radio shell of G323.7$-$1.0 is extremely faint (Green et al., 2014), but there is significant 6.4 keV line emission. The accumulation of such old SNRs might be the origin of the excess of the 6.4 keV line in the GRXE.

Chapter 8

Conclusion

Eleven SNRs are systematically searched for the 6.4 keV line emission using Suzaku XIS data. In these SNRs, the temperature of thermal plasma is lower than 1 keV, or X-ray emission from thermal plasma has not been detected. Based on the 5–8 keV spectra, spatially-extended enhancements of the 6.4 keV line are found from G304.6+0.1 with the significance level of 3.6σ, G323.7−1.0 with 4.1σ and G346.6−0.2 with 3.2σ. In addition, there are signs of the 6.4 keV line enhancements with the significance level of 2.6σ in G330.2+1.0 and with 2.8σ in G348.5+0.1. In G304.6+0.1, G323.7−1.0 and G346.6−0.2, the spatial distribution of the 6.4 keV line emission is not correlated with the thermal X-ray radiation. The equivalent width of the 6.4 keV line is generally large; in particular, the equivalent width of G323.7−1.0 is larger than 1200 eV. The combined spectrum of the enhancements in the three SNRs shows the equivalent width larger than 760 eV. The 6.4 keV line emitting gas of G304.6−0.1, G323.7−1.0 and G346.6−0.2 has to be less ionized than the Mg-like state, based on the energy centroid of 6.40 ± 0.02 keV.

Ionizing non-equilibrium thermal plasma can emit the 6.4 keV line. However, the line centroid suggests that $n_{\rm e}t < 3 \times 10^9$ s cm^{-3}, which means that the age of the plasma is smaller than 100 yr assuming the typical density of SNR plasma of 1H cm^{-3}. Such low-ionized ejecta are unlikely in G304.6+0.1, G323.7−1.0 and G346.6−0.2 because of the relatively old age of the SNRs ($\gtrsim 10^4$ yr). In addition, it is impossible to generate the spatially extended plasma within 100 yr by the shock heating. The large equivalent width also disfavors the thermal plasma scenario. Then, the 6.4 keV line emission is explained by non-thermal processes such as K-shell ionization by photons, non-thermal electrons or protons with energy above Fe K-edge (7.1 keV). The photoionization scenario is rejected because of the absence of the X-ray irradiation source. The scenario of the ionization by cosmic-ray electrons is also unlikely due to the large equivalent width. The interaction between the proton with ~ 10 MeV and the adjacent cold gas, on the other hand, can explain the results. The protons are possibly accelerated in the SNRs.

Bibliography

Acero, F., Ackermann, M., Ajello, M., et al. 2016, ApJS, 224, 8

Aharonian, F., Akhperjanian, A. G., Bazer-Bachi, A. R., et al. 2006a, A&A, 449, 223

Aharonian, F., Akhperjanian, A. G., Bazer-Bachi, A. R., et al. 2006b, ApJ, 636, 777

Aharonian, F., Akhperjanian, A. G., Bazer-Bachi, A. R., et al. 2008a, A&A, 481, 401

Aharonian, F., Akhperjanian, A. G., Barres de Almeida, U., et al. 2008b, A&A, 486, 829

Aharonian, F., Akhperjanian, A. G., Barres de Almeida, U., et al. 2008c, A&A, 490, 685

Anders, E., & Grevesse, N. 1989, GeCoA, 53, 197

Araya, M. 2017, ApJ, 843, 12

Arnaud, K. A. 1996, Astronomical Data Analysis Software and Systems V, 101, 17

Auchettl, K., Slane, P., Castro, D., Foster, A. R., & Smith, R. K. 2015, ApJ, 810, 43

Bamba, A., Yokogawa, J., Sakano, M., & Koyama, K. 2000, PASJ, 52, 259

Bamba, A., Yamazaki, R., Kohri, K., et al. 2009, ApJ, 691, 1854

Bamba, A., Sawada, M., Nakano, Y., et al. 2016a, PASJ, 68, S5

Bamba, A., Terada, Y., Hewitt, J., et al. 2016b, ApJ, 818, 63

Bautz, M. W., LaMarr, B. J., Miller, E. D., et al. 2007, Proc. SPIE, 6686, 66860Q

Bell, A. R. 1978, MNRAS, 182, 147

Castro, D., & Slane, P. 2010, ApJ, 717, 372

Caswell, J. L., Murray, J. D., Roger, R. S., Cole, D. J., & Cooke, D. J. 1975, A&A, 45, 239

Caswell, J. L., Haynes, R. F., Milne, D. K., & Wellington, K. J. 1983, MNRAS, 204, 915

Chernyakova, M., Neronov, A., Aharonian, F., Uchiyama, Y., & Takahashi, T. 2009, MNRAS, 397, 2123

Clark, D. H., Caswell, J. L., & Green, A. J. 1975, Australian Journal of Physics Astrophysical Supplement, 37, 1

Clark, D. H., Green, A. J., & Caswell, J. L. 1975, Australian Journal of Physics Astrophysical Supplement, 37, 75

Combi, J. A., Albacete Colombo, J. F., Sánchez-Ayaso, E., et al. 2010, A&A, 523, A76

Cronin, J. W. 1999, Reviews of Modern Physics Supplement, 71, S165

Dogiel, V., Chernyshov, D., Koyama, K., Nobukawa, M., & Cheng, K.-S. 2011, PASJ, 63, 535

Downes, D., Goss, W. M., Schwarz, U. J., & Wouterloot, J. G. A. 1979, A&AS, 35, 1

Draine, B. T. 1995, Ap&SS, 233, 111

Dubner, G., Giacani, E., Reynoso, E., & Parón, S. 2004, A&A, 426, 201

Fermi, E. 1949, Physical Review, 75, 1169

Egger, R., & Sun, X. 1998, IAU Colloq. 166: The Local Bubble and Beyond, 506, 417

Filipovic, M. D., Payne, J. L., & Jones, P. A. 2005, Serbian Astronomical Journal, 170, 47

Frail, D. A., Goss, W. M., Reynoso, E. M., et al. 1996, AJ, 111, 1651

Fukui, Y., Moriguchi, Y., Tamura, K., et al. 2003, PASJ, 55, L61

Fukui, Y., Sano, H., Sato, J., et al. 2012, ApJ, 746, 82

Gaia Collaboration, Brown, A. G. A., Vallenari, A., et al. 2016, A&A, 595, A2

García, F., Combi, J. A., Albacete-Colombo, J. F., et al. 2012, A&A, 546, A91

Gelfand, J. D., Castro, D., Slane, P. O., et al. 2013, ApJ, 777, 148

Giacani, E., Smith, M. J. S., Dubner, G., et al. 2009, A&A, 507, 841

Gök, F., & Sezer, A. 2012, MNRAS, 423, 1215

Gray, A. D., Cram, L. E., Ekers, R. D., & Goss, W. M. 1991, Nature, 353, 237

Gray, A. D. 1994, MNRAS, 270, 835

Gray, A. D. 1994, MNRAS, 270, 847

Green, A. J., Frail, D. A., Goss, W. M., & Otrupcek, R. 1997, AJ, 114, 2058

Green, D. A. 2009, Bulletin of the Astronomical Society of India, 37, 45

Green, A. J., Reeves, S. N., & Murphy, T. 2014, pasa, 31, e042

Green, D. A. 2014, Bulletin of the Astronomical Society of India, 42, 47

Greiner, J., Tavani, M., & Belloni, T. 1995, ApJL, 441, L43

Hoffman, I. M., Goss, W. M., Brogan, C. L., & Claussen, M. J. 2005, ApJ, 627, 803

Ishisaki, Y., Maeda, Y., Fujimoto, R., et al. 2007, PASJ, 59, 113

Iaria, R., Spanò, M., Di Salvo, T., et al. 2005, ApJ, 619, 503

Itoh, H., & Masai, K. 1989, MNRAS, 236, 885

Iwamoto, K., Brachwitz, F., Nomoto, K., et al. 1999, ApJS, 125, 439

Kaastra, J. S., & Mewe, R. 1993, A&AS, 97, 443

Kaneda, H., Makishima, K., Yamauchi, S., et al. 1997, ApJ, 491, 638

Kassim, N. E., Weiler, K. W., & Baum, S. A. 1991, ApJ, 374, 212

Kawasaki, M. T., Ozaki, M., Nagase, F., et al. 2002, ApJ, 572, 897

Kelley, R. L., Mitsuda, K., Allen, C. A., et al. 2007, PASJ, 59, 77

Kesteven, M. J. L. 1968, Australian Journal of Physics, 21, 739

Kesteven, M. J., & Caswell, J. L. 1987, A&A, 183, 118

Kilpatrick, C. D., Bieging, J. H., & Rieke, G. H. 2016, ApJ, 816, 1

Kokusho, T., Nagayama, T., Kaneda, H., et al. 2013, ApJL, 768, L8

Koralesky, B., Frail, D. A., Goss, W. M., Claussen, M. J., & Green, A. J. 1998, AJ, 116, 1323

Kosack, K., Chaves, R. C. G., & Acero, F. 2011, International Cosmic Ray Conference, 7, 76

Koyama, K., Awaki, H., Kunieda, H., Takano, S., & Tawara, Y. 1989, Nature, 339, 603

Koyama, K., Petre, R., Gotthelf, E. V., et al. 1995, Nature, 378, 255

Koyama, K., Kinugasa, K., Matsuzaki, K., et al. 1997, PASJ, 49, L7

Koyama, K., Tsunemi, H., Dotani, T., et al. 2007a, PASJ, 59, 23

Koyama, K., Hyodo, Y., Inui, T., et al. 2007b, PASJ, 59, 245

LaRosa, T. N., Kassim, N. E., Lazio, T. J. W., & Hyman, S. D. 2000, AJ, 119, 207

Lazendic, J. S., Wardle, M., Burton, M. G., et al. 2002, MNRAS, 331, 537

Leahy, D. A. 1989, A&A, 216, 193

Lee, H.-G., Moon, D.-S., Koo, B.-C., et al. 2011, ApJ, 740, 31

Lodders, K. 2003, ApJ, 591, 1220

Masai, K. 1984, Ap&SS, 98, 367

Migliari, S., Di Salvo, T., Belloni, T., et al. 2003, MNRAS, 342, 909

Milne, D. K., Caswell, J. L., Haynes, R. F., et al. 1985, Proceedings of the Astronomical Society of Australia, 6, 78

Milne, D. K., Caswell, J. L., Kesteven, M. J., Haynes, R. F., & Roger, R. S. 1989, Proceedings of the Astronomical Society of Australia, 8, 187

Minami, S., Ota, N., Yamauchi, S., & Koyama, K. 2013, PASJ, 65, 99

Mitsuda, K., Bautz, M., Inoue, H., et al. 2007, PASJ, 59, S1

Muno, M. P., Baganoff, F. K., Bautz, M. W., et al. 2004, ApJ, 613, 326

Nakamura, R., Bamba, A., Ishida, M., et al. 2009, PASJ, 61, S197

Nakashima, S., Nobukawa, M., Uchida, H., et al. 2013, ApJ, 773, 20

Nobukawa, K. K., Nobukawa, M., Uchiyama, H., et al. 2015, ApJL, 807, L10

Nobukawa, M., Uchiyama, H., Nobukawa, K. K., Yamauchi, S., & Koyama, K. 2016, ApJ, 833, 268

Nobukawa, K. K., Nobukawa, M., Koyama, K., et al. 2017, ApJ, submitted

Nomoto, K., Thielemann, F.-K., & Yokoi, K. 1984, ApJ, 286, 644

Ohira, Y., Murase, K., & Yamazaki, R. 2011, MNRAS, 410, 1577

Ohnishi, T., Koyama, K., Tsuru, T. G., et al. 2011, PASJ, 63, 527

Palmeri, P., Mendoza, C., Kallman, T. R., Bautista, M. A., & Meléndez, M. 2003, A&A, 410, 359

Park, S., Mori, K., Kargaltsev, O., et al. 2006, ApJL, 653, L37

Park, S., Kargaltsev, O., Pavlov, G. G., et al. 2009, ApJ, 695, 431

Park, G., Koo, B.-C., Gibson, S. J., et al. 2013, ApJ, 777, 14

Pfeffermann, E., & Aschenbach, B. 1996, Roentgenstrahlung from the Universe, 267

Prigozhin, G. Y., Kissel, S. E., Bautz, M. W., et al. 2000, Proc. SPIE, 4140, 123

Puehlhofer, G., Brun, F., Capasso, M., et al. 2015, 34th International Cosmic Ray Conference (ICRC2015), 34, 886

Rauw, G., De Becker, M., Gosset, E., Pittard, J. M., & Stevens, I. R. 2003, A&A, 407, 925

Reach, W. T., Rho, J., Tappe, A., et al. 2006, AJ, 131, 1479

Reich, W., & Fuerst, E. 1984, A&AS, 57, 165

Reich, W., Sofue, Y., & Fuerst, E. 1987, PASJ, 39, 573

Revnivtsev, M., & Sazonov, S. 2007, A&A, 471, 159

Revnivtsev, M., Sazonov, S., Churazov, E., et al. 2009, Nature, 458, 1142

Revnivtsev, M. G., Kniazev, A., Karasev, D. I., Berdnikov, L., & Barway, S. 2013, Astronomy Letters, 39, 523

Reynoso, E. M., & Mangum, J. G. 2000, ApJ, 545, 874

Reynoso, E. M., Johnston, S., Green, A. J., & Koribalski, B. S. 2006, MNRAS, 369, 416

Rho, J., & Borkowski, K. J. 2002, ApJ, 575, 201

Rybicki, G. B., & Lightman, A. P. 1979, New York, Wiley-Interscience, 1979. 393 p.,

Sano, H., Tanaka, T., Torii, K., et al. 2013, ApJ, 778, 59

Sato, T., Koyama, K., Takahashi, T., Odaka, H., & Nakashima, S. 2014, PASJ, 66, 124

Sato, T., Koyama, K., Lee, S.-H., & Takahashi, T. 2016, PASJ, 68, S8

Sawada, M., & Koyama, K. 2012, PASJ, 64, 81

Scholz, P., Archibald, R. F., Kaspi, V. M., et al. 2014, ApJ, 783, 99

Scoville, N. Z., Yun, M. S., Sanders, D. B., Clemens, D. P., & Waller, W. H. 1987, ApJS, 63, 821

Sedov, L. I. 1959, Similarity and Dimensional Methods in Mechanics, New York: Academic Press, 1959,

Serlemitsos, P. J., Soong, Y., Chan, K.-W., et al. 2007, PASJ, 59, S9

Seward, F. D. 1990, ApJS, 73, 781

Sezer, A., Gök, F., Hudaverdi, M., Kimura, M., & Ercan, E. N. 2011a, MNRAS, 415, 301

Sezer, A., Gök, F., Hudaverdi, M., & Ercan, E. N. 2011b, MNRAS, 417, 1387

Shaver, P. A., & Goss, W. M. 1970, Australian Journal of Physics Astrophysical Supplement, 14, 133

Slane, P., Smith, R. K., Hughes, J. P., & Petre, R. 2002, ApJ, 564, 284

Sugizaki, M., Mitsuda, K., Kaneda, H., et al. 2001, ApJS, 134, 77

Takahashi, T., Abe, K., Endo, M., et al. 2007, PASJ, 59, 35

Tanimori, T., Hayami, Y., Kamei, S., et al. 1998, ApJL, 497, L25

Tatischeff, V., Decourchelle, A., & Maurin, G. 2012, A&A, 546, A88

Tawa, N., Hayashida, K., Nagai, M., et al. 2008, PASJ, 60, S11

Taylor, G. 1950, Proceedings of the Royal Society of London Series A, 201, 159

Tian, W. W., & Leahy, D. A. 2008, MNRAS, 391, L54

Torii, K., Uchida, H., Hasuike, K., et al. 2006, PASJ, 58, L11

Tsujimoto, M., Hyodo, Y., & Koyama, K. 2007, PASJ, 59, 229

Uchida, K. I., Morris, M., Bally, J., Pound, M., & Yusef-Zadeh, F. 1992, ApJ, 398, 128

Uchiyama, Y., Maeda, Y., Ebara, M., et al. 2008, PASJ, 60, S35

Uchiyama, H., Ozawa, M., Matsumoto, H., et al. 2009, PASJ, 61, S9

Uchiyama, H., Nobukawa, M., Tsuru, T. G., & Koyama, K. 2013, PASJ, 65, 19

Vink, J. 2012, A&AR, 20, 49

Washino, R., Uchida, H., Nobukawa, M., et al. 2016, PASJ, 68, S4

Whiteoak, J. B. Z., & Green, A. J. 1996, A&AS, 118, 329

Wolszczan, A., Cordes, J. M., & Dewey, R. J. 1991, ApJL, 372, L99

Worrall, D. M., Marshall, F. E., Boldt, E. A., & Swank, J. H. 1982, ApJ, 255, 111

Wu, J. H. K., Wu, E. M. H., Hui, C. Y., et al. 2011, ApJL, 740, L12

Xin, Y.-L., Liang, Y.-F., Li, X., et al. 2016, ApJ, 817, 64

Yamaguchi, H., Ozawa, M., Koyama, K., et al. 2009, ApJL, 705, L6

Yamaguchi, H., Badenes, C., Petre, R., et al. 2014, ApJL, 785, L27

Yamauchi, S., Kawada, M., Koyama, K., Kunieda, H., & Tawara, Y. 1990, ApJ, 365, 532

Yamauchi, S., Ueno, M., Koyama, K., & Bamba, A. 2008, PASJ, 60, 1143

Yamauchi, S., Nobukawa, M., Koyama, K., & Yonemori, M. 2013, PASJ, 65, 6

Yamauchi, S., Minami, S., Ota, N., & Koyama, K. 2014, PASJ, 66, 2

Yamauchi, S., Nobukawa, K. K., Nobukawa, M., Uchiyama, H., & Koyama, K. 2016, PASJ, 68, 59

Yusef-Zadeh, F., & Bally, J. 1987, Nature, 330, 455

Acknowledgement

First of all, I would like to express my most sincere gratitude and appreciation to Prof.Hironori Matsumoto for his guidance, support, advice, encouragement, and any other things. He supported my studies on all sides, such as the basic of astrophysics, analysis, discussion, and so on. I am grateful to emeritus Prof. Hidehiro Kaneda, Prof. Yuzuru Tawara, Dr. Ikuyuki Mitsuishi, Dr. Kazunori bish Ishibashi, and Dr. Keisuke Tamura for giving me various useful advice and comments in the analysis and the discussion. Dr. Kiyoshi Hayashida and Dr. Hiroshi Nakajima dave me many useful comments and they supported my activity at Osaka University. I express my gratitude to Dr. Masayoshi Nobukawa, Dr. Kumiko K. Nobukawa, Dr. Hideki Uchiyama, Prof. Shigeo Yamauchi, and Prof. Katsuji Koyama. They offered me an opportunity to study the SNRs and provided a lot of useful comments. This thesis would not be possible without their support and discussions with them. I am also grateful to Dr. Hideyuki Mori. He instructed me the basic skill of the analysis, English, and many matters.

I would like to give my thanks to Mr. Yasunori Babazaki, Mr. Shota Inoue, and all students. Owing to them, I spent fulfilling and enjoyable life in the university. Finally, I wish to thank my family and friends. Without their encouragement and understanding, it would have been impossible for me to finish my work.